COUPLING NITROGEN VACANCY CENTERS IN DIAMOND TO A NANOMECHANICAL OSCILLATOR

by

THEIN HTAY OO

A DISSERTATION

Presented to the Department of Physics
and the Graduate School of the University of Oregon
in partial fulfillment of the requirements
for the degree of
Doctor of Philosophy

September 2017

DISSERTATION APPROVAL PAGE

Student: Thein Htay Oo

Title: Coupling Nitrogen Vacancy Centers in Diamond to A Nanomechanical Oscillator

This dissertation has been accepted and approved in partial fulfillment of the requirements for the Doctor of Philosophy degree in the Department of Physics by:

Benjamin McMorran	Chair
Hailin Wang	Advisor
Paul Csonka	Core Member
Cathy Wong	Institutional Representative

and

Sara D. Hodges	Interim Vice Provost and Dean of the Graduate School

Original approval signatures are on file with the University of Oregon Graduate School.

Degree awarded September 2017

DISSERTATION ABSTRACT

Thein Htay Oo

Doctor of Philosophy

Department of Physics

September 2017

Title: Coupling Nitrogen Vacancy Centers in Diamond to A Nanomechanical Oscillator

Exotic aspects of quantum mechanics, such as quantum entanglement, can be exploited to solve computational problems that are impractical to solve with conventional computers. With the realization of robust solid-state qubits, such as Nitrogen Vacancy (NV) centers in diamond, an outstanding challenge is to develop experimental approaches that can control the interactions between individual qubits. This dissertation develops a diamond-based experimental system that exploits acoustic waves or mechanical vibrations to mediate interactions between spin qubits. This spin-mechanical system features three essential elements: robust qubits, high quality-factor diamond nanomechanical resonator, and strong spin-mechanical coupling, thus enabling a new and promising platform for pursuing solid-state quantum computer.

For the spin-mechanical system, NV centers are created near the surface of a bulk diamond through nitrogen ion implantation followed by stepwise high temperature annealing. We successfully suppress environmental fluctuations and achieve NV centers with stable and spectrally narrow (< 50 MHz) fluorescence at low temperature, which is crucial for the spin-mechanical system.

Diamond nanomechanical resonators with a fundamental frequency near 1 GHz have been successfully fabricated with a diamond-on-insulator approach. The resonators are suspended from a silicon substrate and are supported with long and thin tethers, decoupling the mechanical modes from the surrounding environment. Diamond nanofabrication is still in its infancy. Numerous fabrication problems occurring during etching, mask transfer, and wafer bonding have been painstakingly resolved.

Strong spin-mechanical coupling is demonstrated via the strain coupling of the NV excited-states. The spin-mechanical coupling takes place through a Λ-type three-level system, where two ground-spin-states couple to an excited-state through a phonon-assisted as well as a direct dipole optical transition. Both coherent population trapping and optically-driven spin transitions have been realized. The coherent population trapping demonstrates the coupling between an acoustic wave and an electron spin coherence through a dark state, thus avoiding the short lifetime of the excited state. The optically-driven spin transitions can enable the quantum control of both spin and mechanical degrees of freedom.

This dissertation includes previously published co-authored material.

CURRICULUM VITAE

NAME OF AUTHOR: Thein Htay Oo

GRADUATE AND UNDERGRADUATE SCHOOLS ATTENDED:
University of Oregon, Eugene, Oregon
Western Illinois University, Macomb, Illinois
Yangon Technological University, Yangon, Myanmar

DEGREES AWARDED:
Doctor of Philosophy, Physics, 2017, University of Oregon
Master of Science in Physics, 2009, Western Illinois University
Bachelor of Engineering in Electronics, 2003, Yangon Technological University

AREAS OF SPECIAL INTEREST:
Quantum Optics
Semiconductor Fabrication
Quantum Information Processing

PROFESSIONAL EXPERIENCE:

Graduate Research Fellow, University of Oregon, 2011-2017

Graduate Teaching Fellow, Western Illinois University, 2009 - 2010

GRANTS, AWARDS AND HONORS:

Third Prize Winner of Poster Sections at Material Science Institute/Oregon Center for Optics symposium (2013)

Outstanding Graduate Physics Award at Western Illinois University (2008 009)

Outstanding Mid-term Graduate Physics Award at Western Illinois University (2007 008)

Tsuchiya International Student Science Scholarship Award (2007 008)

PUBLICATIONS:

Golter, D. A.,Oo, T., Amezcua, M., Stewart, K. A. Wang, H. Coupling a Surface Acoustic Wave to an Electron Spin in Diamond via a Dark State. Phys. Rev. X 6, 41060 (2016).

Golter, D. A., Oo, T., Amezcua, M., Stewart, K. A. Wang, H. Optomechanical Quantum Control of a Nitrogen-Vacancy Center in Diamond. Phys. Rev. Lett. 116, 143602 (2016)

Jiang, X., Wang, M., Kuzyk, M., Oo, T., Long, G. Wang, H. Chip-based silica microspheres for cavity optomechanics. Optics Express 23, 27260 (2015).

Oo, T., Dong, C., Fiore, V. Wang, H. Evanescently coupled optomechanical system with SiN nanomechanical oscillator and deformed silica microsphere. Appl. Phys. Lett. 103, 031116 (2013).

ACKNOWLEDGEMENTS

First and foremost, I would like to thank my advisor, Hailin Wang who encourages and guides me through out my years as a graduate student.

I also would like to thank my faculty members on my committee, Benjamin McMorran, Paul Csonka, Shannon Boettcher and Cathy Wong for their support and encouragement through out my doctoral research.

I would like to express my gratitude to Benjamín Aleman for guiding me to set up the reactive ion etching system (RIE). Without this complex state-of-the-art system, some of my research projects will never taken place. I appreciate Kurt A. Langworthy and Robert Fischer for their support and advices on semiconductor fabrication processes. I would like to thank Kris Johnson and John Boosinger for their expertise and insight on cryogenic systems, thermal annealing systems and reactive ion etching systems.

I would like to also express gratitude to Tom Reynolds for allowing me to use Nanotech Fabrication Facility at University of California, Santa Barbara (UCSB).

I would like to thank my mother and father for their unconditional love and support through out my journey.

I also express my thanks to my colleagues, Ignas Lekavicius, Mark Kuzyk, Mayra Amezcua, Abby Pauls, Spencer Alexander, Chunhua Dong, Jintao Zhang, Xuefeng Jiang, Andrew Golter, Tom Baldwin and Victor Fiore .

I would like to thank my wife and daughter who understand, support and encourage me to follow my passion.

I thank all the administrative staff who help and support through out my years as a graduate student here.

TABLE OF CONTENTS

LIST OF FIGURES

Figure Page

Figure Page

CHAPTER I

INTRODUCTION

1.1. Quantum Information Processing

A quantum mechanical system can feature unusual phenomena such as quantum superposition and quantum entanglement. This exotic aspect of quantum mechanics can be exploited to solve computational problems that are impractical or impossible to solve with conventional, classical computers [1–3]. The quest for developing quantum computers has attracted extensive worldwide efforts with wide-ranging technical approaches. The elementary units for quantum information processing are quantum bits or qubits, which are essentially two-level quantum systems. The most promising qubit systems for implementing quantum computers have thus far been superconducting circuits[4, 5] and trapped ions [6–8], which was rewarded with Nobel Prize in 2012. Intense research efforts have also focused on other qubit systems, especially solid-state spin qubits that can preserve quantum coherence for a long time and can potentially enable scalable quantum computers. An outstanding challenge in these efforts is to develop and demonstrate experimental approaches that can precisely control the interactions between individual spin qubits.

1.2. Nitrogen Vacancy Centers as Qubits

Negatively-charged nitrogen Vacancy (NV) centers in diamond have recently emerged as a leading candidate for solid-state spin qubits. NV centers have many properties that resemble those of trapped-ion atomic systems. The decoherence time of an electron spin in NV centers can be of order of a few milliseconds, which is several orders of magnitude longer than that of superconducting qubits[9, 10]. Spins in NV centers can be easily manipulated with microwave waves. Spin states can be prepared and measured (or read out) with high fidelity through convenient optical processes. In addition, nuclear spins related to NV centers can feature decoherence time greater than seconds and can thus serve as excellent quantum memories.

1.3. Surface Acoustic Waves (SAW)

Electromagnetic waves have traditionally been the primary experimental tool for controlling a quantum system and for transmitting and distributing quantum information. There has also been strong recent interest in using acoustic or mechanical waves, in particular surface acoustic waves (SAWs), for quantum control and on-chip quantum communication of artificial atoms.

SAWs are elastic waves which propagate near the surface of a medium. The deformation in the medium originated by propagation of SAW waves decays exponentially away from the surface. Therefore, most of the energy is confined within one wavelength depth of the propagating SAW wave.

SAW filters are widely used in mobile communication industry. In recent years, SAW has garnered substantial interests in quantum science research. Phonons generated by SAW waves were successfully coupled to an artificial atom[11]. Universal on-chip quantum transducers based on SAW waves are theoretically proposed. SAW induced quantum oscillation is investigated in a two-dimensional electron system[12]. SAW resonators with internal quality factor approaching 0.5 million at 0.5 GHz was recently demonstrated and they are promising candidates for integrating with supercounducting quantum circuits[13]. SAW waves are successfully coupled to a coupled quantum dot-nanocavity system in the weak coupling regime of cavity-quantumelectrodynamcis[14].

1.4. Spin-mechanical Systems

A major focus of the research efforts in this dissertation is to explore the use of mechanical vibrations including SAWs for quantum control of NV centers, with the eventual goal of using mechanical waves to mediate coherent interactions between distant NV centers on a chip. Coherent coupling between electron spins and nanomechanical resonators has been pursued with a variety of approaches. An earlier study placed a cantilever with magnetic tip to the close proximity of an electron spin in diamond[15]. The spin qubit is coupled to the motion of the magnetized nanomechanical oscillator through magnetic field gradients. Experimental realization of coupling a mechanical oscillator to an electron spin of a NV center in diamond through mechanical strain is also successfully demonstrated by several research groups[16–19]. One approach used a single-crystal cantilever with embedded NV center spins. The spin-phonon coupling is realized by a lattice strain caused by mechanical oscillation of the cantilever[18]. Another approach used electrically driven gigahertz-frequency mechanical (stress) waves instead of a cantilever. The mechanical (stress) waves are generated by fabricating High-Overtone Bulk Acoustic Resonator (HBAR) on a diamond sample[20].

1.5. Overview of Dissertation

Coupling of an electron spin in NV centers in diamond to mechanical vibrations has not been widely explored even though NV centers are quite promising for quantum information and communication systems. First of all, the fabrication of diamond mechanical oscillators are relatively hard compared to silicon nitride or silicon due to the physical properties of diamond. NV centers with stable fluorescence are also difficult to be embedded in diamond resonators because of their sensitivity to some etching processes. In this thesis, I will try to address three major issues which are hindering the integration of NV spin systems to a mechanical resonator. First, I will discuss the near-surface implantation of NV centers in diamond. Then, I will elaborate on the fabrication of SAW devices and diamond mechanical resonators. Finally, I will demonstrate how we couple SAW to the excited state of an electron spin in the NV center.

1.5.1. Implantation of NV Centers

After a brief discussion of NV properties in Chapter II and the experimental setups in Chapter III, I will discuss the creation of nitrogen vacancy centers in diamond. These techniques discussed in Chapter IV will be easily transferable to other color centers such as silicon vacancy centers or germanium vacancy centers. I will discuss the surface preparation of diamond which are crucial for charge stability of NV centers and any future resonator fabrication. We will use the ion implantation method in which we bombard the diamond sample with energetic $^{15}N^+$ ions. The energy of the ions and the type of the material (in our case it is diamond.) controls how far the ions will penetrate under the surface of the sample. In that way, we can control the location of NV centers below the surface. Extensive post-annealing and surface termination result in NV centers with stable fluorescence. Having NV centers with charge stability is one of the crucial requirements of any future study of quantum behaviors of diamond nano- and micro-mechanical systems.

1.5.2. Fabrication of Diamond Mechanical Resonators

In chapter V, I will discuss the modeling and fabrication of mechanical resonators. In general, diamond is hard to fabricate due to its well-known chemical inertness. Therefore, we started the modeling and fabrication on silicon nitride. Silicon nitride is inexpensive and has relatively well documented techniques about its fabrication processes such as dry and wet etching. We will also discuss the beam theory which explain the resonant eigen frequency of these oscillators. We are able to tailor the desired resonant frequencies by applying Euler-Bernoulli beam theory. The calculation from Euler-Bernoulli beam theory is in a good agreement with the experiment.

For diamond resonator fabrication, we have explored two approaches. One uses focused ions beam milling and another uses on-chip fabrication. We will discuss how to polish a diamond oscillator using a focused ions beam to minimize the surface damage, which is important for the quality of the resonator. For on-chip diamond resonator fabrication, we will focus on wafer bonding process and how to select the proper mask for etching. The selectivity of the mask is critical when etching diamond due to the chemical inertness of diamond.

We wil also introduce several ways to characterize the beam we fabricated. We will demonstrate peizo-driven temporal ring-down measurements and spectral domain measurements using a simple but powerful optical interferometric measurement setup.

1.5.3. Excited State Electron-phonon Coupling

In chapter VI, I will discuss the excited state electron-phonon coupling in NV centers in diamond using SAWs induced by interdigital transducer (IDT). We will demonstrate how to incorporate phonon-mediated resolved side band coupling into a two-level system in NV centers. We will study phonon-mediated excited state Rabi oscillation. This chapter was previously published in Physical Review Letters[16] coauthored with Andrew Golter, Mayra Amezcua, Kevin Steward and Hailin Wang.

In chapter VII, I will explore phonon-mediated coupling in a Λ-type three-level system in NV centers. We will study both phonon-assisted coherent population trapping (CPT) and optically driven sideband spin transitions. This chapter was previously published in Physical Review X[21] coauthored with Andrew Golter, Mayra Amezcua, Ignas Lekavicius, Kevin Steward and Hailin Wang. .

These experiments demonstrate how to take advantage of the strong excited-state electron-phonon interaction to mediate and control the coupling between a spin and mechanical degrees of freedom, while avoiding decoherence usually associated with the excited state. These approaches can be extended to other emerging spin systems with spin defect centers such as silicon or germanium vacancy center in diamond, defect centers in silicon carbide, quantum-dots as well as superconducting systems.

CHAPTER II

NITROGEN VACANCY CENTER IN DIAMOND

2.1. Introduction

Diamond is well known for its unique and exceptional properties, including hardness, thermal conductivity, optical transparency, and chemical and biochemical inertness. Some of its interesting characteristics emerge from its lattice properties. Nitrogen-vacancy (**NV**) color centers[22], which are formed in a diamond by one substitutional nitrogen atom and an adjacent carbon vacancy, are among the most intensely studied lattice defects in recent years. NV center in diamond behaves like a solid state artifical atom[23] and has been widely investigated in magnetomery[23, 24], thermometry[25], mechanical sensing, electric field sensing,biosensing[26] and nanoscale nuclear magnetic spin resonance spectroscopy (NMR). NV center is also a promising candidate for scalable and feasible implementation of quantum computation and quantum information processing (**QIP**)[27].

2.2. Nitrogen-Vacancy Center in Diamond

2.2.1. Diamond Structure

Diamond is widely acknowledged as an allotrope of carbon constructed by sp^3 hybridized covalent bonds in the form of a tetrahedral geometry. It consists of two face-centered cubic (fcc) lattice structures (see Fig. 2.1). These covalent bonds make diamond very rigid. Even though diamond is one of the best thermal conductor, it is also a great electronic insulator with a wide energy band gap of 5.45eV which gives rise to its optical transparency in the visible regime.

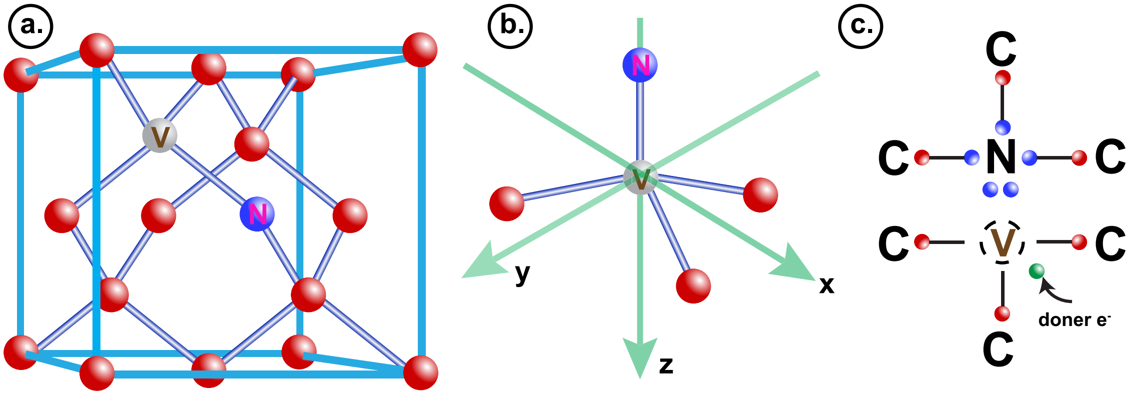

FIGURE 2.1. Carbons atoms are marked in red, a nitrogen(N) atom in violet, and a vacancy (V) is marked in gray and a donor electron from the environment which is most likely coming from another substitutional nitrogen atom (a) A nitrogen vacancy center in diamond lattice. (b) Symmetry operations for C_{3v} group include rotational invariance by 2πn/3 around the NV axis. (c) dot structure drawing diagram of NV defect with surrounding electrons.

2.2.2. Classification of Diamond

Diamond samples with NV centers are commercially available from Element Six (E6) Technologies, Apollo Diamond, and Sumitomo Electric and can exhibit unique characteristics such as concentration of impurities and doping as well as specific nitrogen and carbon isotopes. In general, both natural and artificial diamond are classified into two groups based on the concentration of nitrogen content: type “I” for high and type “II” for low concentration. Type “I” is further divided into type “Ia” and “Ib”, so does type “II”. Nitrogen atoms are commonly regarded as contaminants to diamonds and their concentration is usually expressed in parts-per-million (ppm, 10^{-6}) and parts-per-billion (ppb, 10^{-9}). Both type “Ia” and “Ib” typically contain 100 to 3000 ppm nitrogen atoms. The only difference between type “Ia” and “Ib” is type “Ia” consists of aggregated nitrogen atoms, whereas type “Ib” has single substitutional atoms. In contract, type “II” generally contains less than 5 ppm nitrogen atoms. Nitrogen atoms are the major impurity in type “IIa” which is useful for electrical insulation. Boron atoms are the major impurity in type “IIb” and these type “IIb” diamonds are used as p-type semiconductor. Almost all ($> 98\%$) of natural diamonds belong to type “I" while most artificial diamonds manufactured by chemical vapor deposition method (so called "CVD diamonds") are type “II". Single crystal CVD diamonds from E6 have even divided into three sub-groups: standard optical grade, electronic detector grade with (< 50 ppb) in nitrogen atoms and (<0.5 ppb) in boron atoms and quantum grade with (> 99.95 % ^{12}C) isotopic purity and (< 1 ppb) in nitrogen atoms. Most of the diamond samples we use in the laboratory come from E6 as electronic-detector grade single crystal CVD diamonds (type “IIa”). The crystal structure of the CVD single crystal diamonds used in this thesis is (100) oriented along the surface, with (110) edges, and (111) as a cleavage plane.

2.2.3. Electronic Properties of NV center in Diamond

Both neutral (NV^0) and negative (NV^-) centers can be examined in diamond. In both cases, they are composed of the covalent bonds of three carbon atoms and one nitrogen atom surrounding the vacancy. The neutral NV center (NV^0) possesses 5 electrons and an electron spin of 1/2 whereas the negative NV center has 6 electrons and an electron spin of 1 (see in Fig. 2.1). The negatively charged NV (NV^-) center has undergone decades of intense scientific research and conventionally referred to as NV center with the absence of the "$-$" sign. This naming convention is also applied through out my dissertation since my research focuses exclusively on the negatively charged NV center.

The ground state of the NV center is a spin triplet state with $^3A_2$ symmetry. There are three magnetic sublevels: m_s=0 ($|0\rangle$) and m_s=$\pm$ 1 ($|\pm1\rangle$). These sublevels experience a zero-field splitting due to a spin-spin interaction that raises the energy of $|\pm1\rangle$ with respect to $|0\rangle$ by $\mathcal{D} \approx 2.87$ GHz. Degeneracy between $|\pm1\rangle$ can be lifted by applying an external magnetic field along the NV center axis which causes a Zeeman shift given by $\Delta = m_s \gamma B$, where gyromagnetic ratio $\gamma = g\ \mu_B/h = 2.8$ MHz/G. The nearest excited state is located at 1.945 eV above the ground state[28–34].

2.2.4. Optical Properties of NV Center in Diamond

At room temperature, the cycling optical transition between the ground ($^3A_2$) and excited (^3E) states exhibits a characteristic zero-phonon line (ZPL) at 637nm with a broad phonon sideband which ranges from 637nm up to 800nm with a maximum at approximately 680nm. Only 4% of the photons are emitted into zero-phonon line[35] and the rest decays into the phonon sideband. A single photon can be released at every 12 ns during the relaxation into the ground states. At cryogenic temperature,

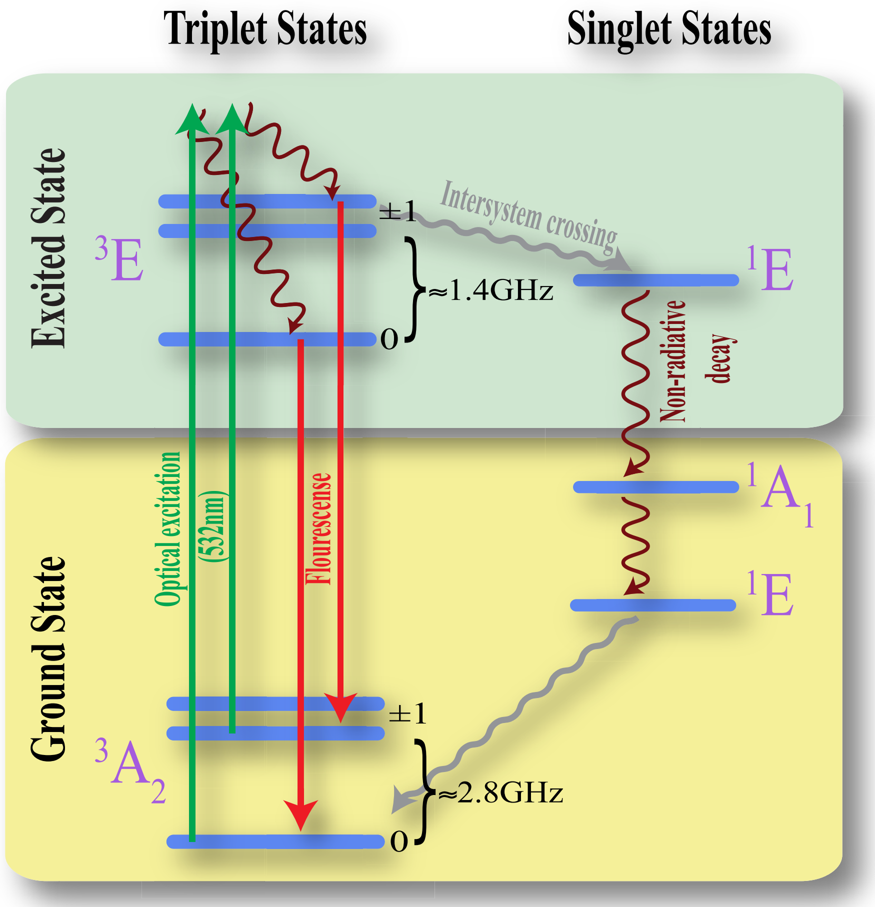

FIGURE 2.2. Energy level structure at room temperature. The zero field splitting between m_s =0 and $m_s = \pm1$ sublevels of the ground triplet states is ≈ 2.87GHz while the similar splitting of the excited states is ≈ 1.43GHz. The green arrows represent the non-resonant (532nm) optical excitation into the phonon sidebands. Fluorescence emission is shown in red, the intersystem crossing is shown in gray and non-radiative decay is indicated by brown arrows.

the bandwidth of optical transitions between the ground and excited triplet states is narrower than the sublevels and moreover, these transitions, in general, obey the spin-selection rule. However, there is a non-radiative decay path from the excited states to metastable singlet states with an effective lifetime of ≈ 200 ns. Even though the inhomogeneous optical linewidth of the ensembles of NV centers is approximately several GHz, the single NV center's linewidth can be in the MHz range which is actually limited by the excited state lifetime.

CHAPTER III

EXPERIMENTAL TECHNIQUE & SETUP

3.1. Introduction

All of my research has been conducted on a single NV center at cryogenic temperature (7.78 K). I will discuss the home-built low working distance confocal setup, how the optical excitation has been performed and how the spin states are prepared, how the surface acoustic waves are generated and being monitored.

3.2. Cryogenic Setup

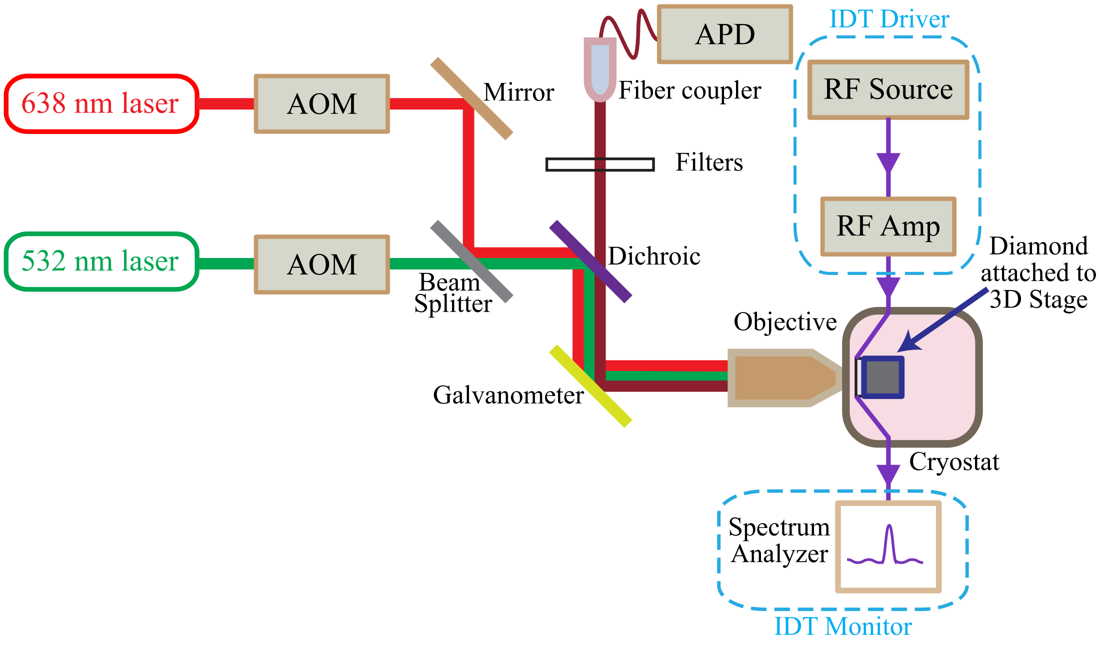

FIGURE 3.1. Low temperature and low working distance confocal microscope setup.

I inherited a confocal setup from my colleague, Andrew Golter and he discussed in details about the setup in his thesis[36]. Therefore, I will focus only on the major upgrades I made to his setup. First, the diamond sample is mounted on the sub-nm resolution 3D positioning stages (ANP 51 series) from Attocube Systems Inc. In most NV center experiments, it is quite critical to get high fluorescence collection efficiency. Various various methods such as pillar structures, and solid immersion lenses[37] (SILs) have been performed to achieve higher collection efficiency.

One of the simple approaches is to use a high numerical aperture microscope objective (see Fig. 3.1). At the same time, an objective with a high magnification is also needed to spatially resolve a single NV center from its environment. All microscope objectives, that satisfy these two requirements, come at a price which is their low working distance. There are two ways to solve these problems: one is to place the microscope objective inside the cryogenic chamber and another is to install an ultra thin cryogenic window so that the low working distance objective can reach the sample. Frequently cooling-heating cycles could damage the objectives in the long run; thus, the latter method is chosen to pursue for the cryogenic setup. After searching through hundreds of microscope objectives, we carefully chose Nikon CFI Plan LWD IMSI 100X microscope objective with an 0.85 numerical aperture, working distance 0.95mm, and cover glass thickness from 0.6-1.3mm. To be compatible with this objective, a 1mm low working distance window with anti-reflective coating from Montana Instruments Corporation is installed as a side window in our cryostat [38].

It is essential to place the diamond sample as close as possible to the cryostat window due to the low working distance objective. This means the sample mount must be about 32.44mm long and more than half of its length will be over hanging because of the size of the attocube stages. To avoid undesirable torque from the

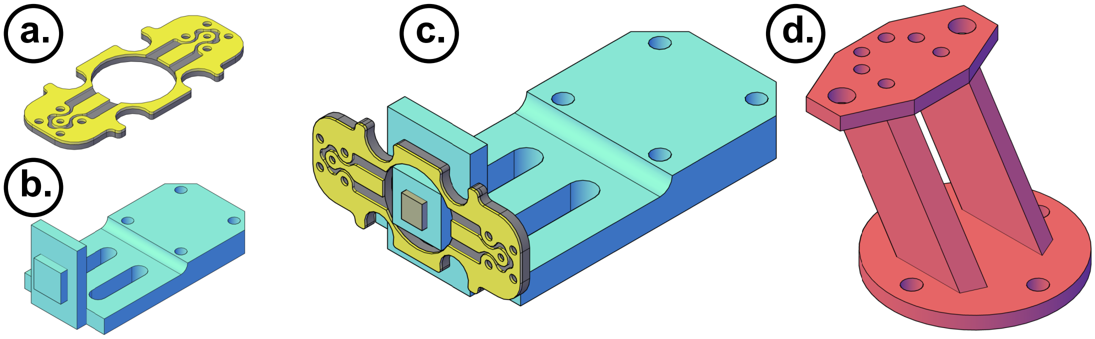

FIGURE 3.2. Custom-built Sample Mount, Spacer and PCB for Cryogenic System. (a) Printed Circuit Board (PCB) is designed to be able to mount right next to the diamond sample and have two available channels for signals coming in and out with the command ground. (b) Sample mount which will be installed on the top of the attocube stage. (c) A diamond sample, PCB and sample mount are all put together. (d) A 54°-angled spacer. Both the sample mount and spacer are made of oxygen-free high-conductivity (OFHC) copper and are gold-plated to prevent oxidation.

sample mount to the attocube stage and to reduce the vibration while moving the stages, the sample mount was meticulously designed to shift the center of mass at the same time as the rigidity of the copper sample mount and the weight limit that the attocube can tolerate are maintained (see Fig. 3.2b).

The low working distance window from Montana Instruments cryogenic system is only recommended for the top window. To install it in the side window, we have to use the long and heavy sample mount which requires ANP 101 series attocube stages to withstand its weight. We plan to install two sets of 3D attocube stages (total of six stages) inside the cryostat in the future; therefore, there is only enough footprint to fit two sets of ANP 51 series attocube stages. To solve this problem, the 54°-angled spacer is made out of a single piece of oxygen-free high-conductivity (OFHC) copper to acquire the best thermal conduction through out the spacer by circumventing thermal contact resistance (see Fig. 3.2d). This 54°-angled spacer will bring the attocube stages closer to the side window so that the short-length sample mount can be used as shown in Fig. 3.3d.

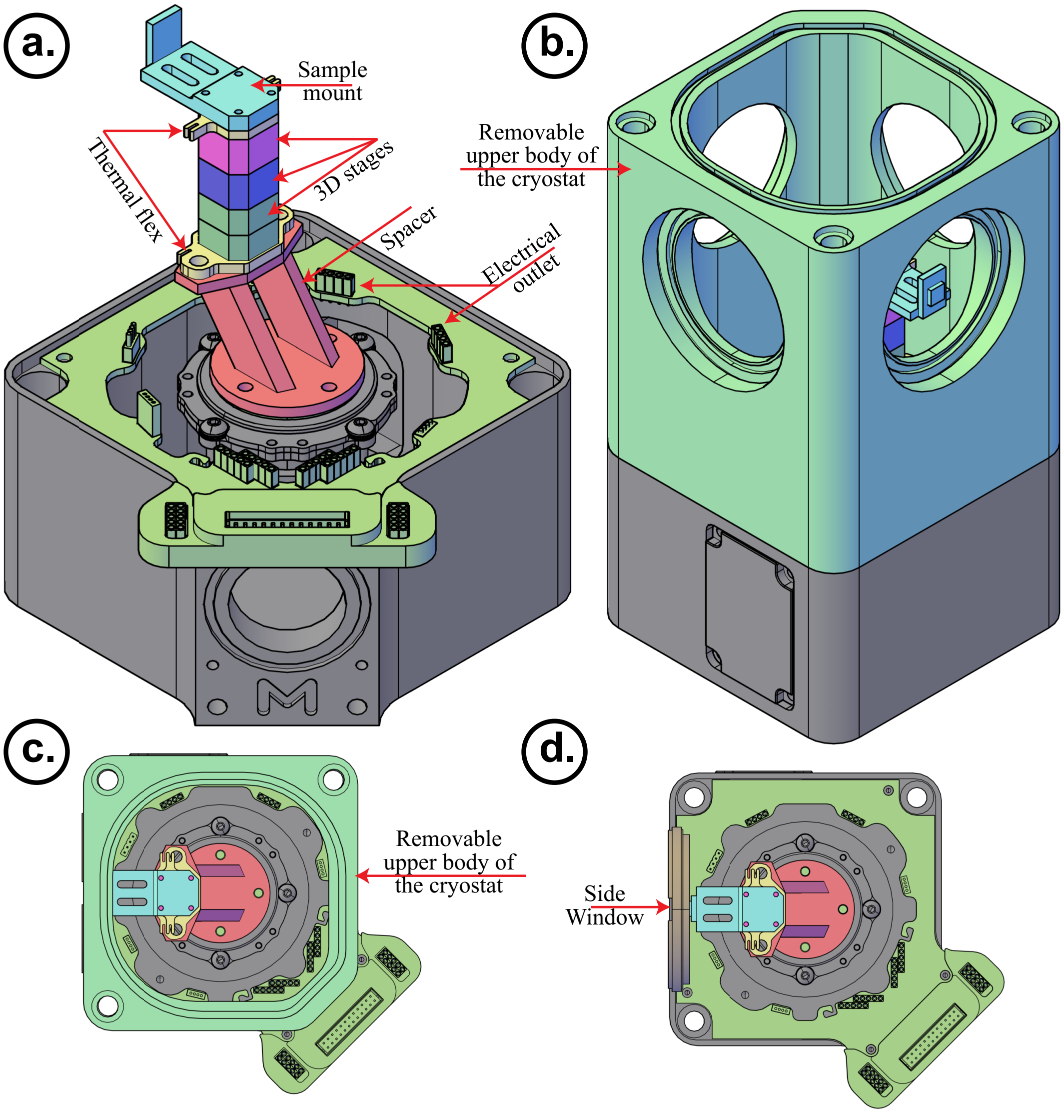

FIGURE 3.3. Cryogenic setup with Sub-nm resolution 3D translational stages. (a) The inside layout of the cryostat where the spacer, the sample mount, three attocube stages and thermal flex which bypass attocube stages so that most of the heat can be transferred from the sample mount to the main cold finger through the spacer. (b) With the installation of the removable upper body of the cryostat. (c) Top view with the removable upper body of the cryostat showing that the attocube stages are successfully installed closer to the side window, and (d) Top view to show how close the sample is to the side window of the cryostat. Drawing of the cryogenic chamber assembly is courtesy of Montana Instruments Corporation.

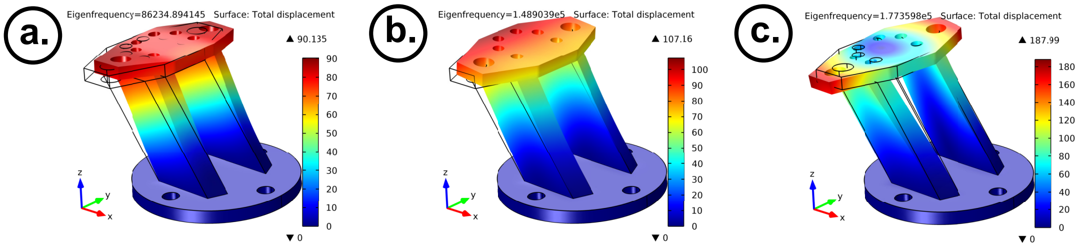

FIGURE 3.4. Comsol modeling of the spacer by adjusting the mechanical structure. (a) 86kHz, (b) 149kHz and (c) 177kHz are the three lowest mechanical frequencies of the spacer.

All the attocube stages used in this system are open-looped nanopositioners and are driven by an Attocube Systems ANC300 controller unit with ANM300 modules. DC voltage within the range of 0-150V can be applied to drive these stages in the fine positioning mode and a sawtooth wave with amplitude of 0-50V and frequency within the range of 0-50kHz can be in the coarse positioning mode. For our experiments, 22-25V and 220-280Hz are usually applied in the coarse positioning mode. When the spacer was modeled, the multiple orders of the fundamental frequency of the spacer are calculated by using COMSOL modeling software (see in Fig. 3.4) and we ensure they are not overlapping with the driving frequency of the attocube stages to avoid resonant vibration in the spacer. By adjusting the position and structure of the two vertical supports that connect the top and bottom plate, the fundamental frequency of the spacer (86kHz) is significantly shifted out of the driving frequency range which is 0-50kHz. This will not be an issue if the spacer is a solid piece but it will definitely increase thermal mass and the cryostat will take a longer time to cool down to 7.7K.This current setup with the three attocube stages, the custom mount and spacer take at least 20 minutes less time to cool down than the previous setup with the Montana Instruments' spacer and sample mount even though the latter does not has attocube stages inside the cryostat.

3.3. Home-built FPGA-based Fast Photon Counting Instrument

Field Programmable Gate Arrays (FPGAs) are universal in systems that require high speed data or signal processing. An FPGA is made of a giant array of interconnected logic gates and they can be configured in multiple ways according to the requirements of the individual research. Therefore, an FPGA development board can be constructed as a function generator, lock-in amplifier, spectrum analyzer, pulse generator, ultra fast digital counter and so forth. These logic gates are reconfigurable. Thus, a development board can be a function generator at one moment and a few minutes later it can be an oscilloscope.

An FPGA-based photon counting card is used on some of the experiments such as Rabi oscillation. With the use of this inexpensive home-built photon counting card, every photon released from the system can be time-tagged with the resolution of 2.8 ns. This instrument is built based on this article[39]. In our modified version, we have each individual trigger input for each counting input and have also written a python module to work with this card. The CG635 from Stanford Research Systems is set up as an external clock generator via the CMOS signal mode. With the use of memory mapping in python, 100 MB of binary data can be interpreted as a meaningful plot within a few seconds.

3.4. SAW Generating and Monitoring Setup

Interdigital transducers (IDT) are fabricated mainly in a pair: one to generate surface acoustic wave from the electrical signal and another to reconstruct the electrical signal from the mechanical one. I will refer to the former IDT as Input IDT and the latter as Output IDT in the rest of this thesis. As shown in Fig. 3.1, the Agilent Technologies 8648C signal generator is tuned to be the frequency of the

SAW and the signal coming from the signal generator is amplified by a Mini-Circuits ZHL-10W-2G+ high power amplifier. The HP 6267B DC power supply is used as a power supply for the Mini-Circuits amplifier. Even though the typical current and voltage required for the amplifier are 4A and 24V, the amplifier needs at least 6A to turn on due to the induced electromotive force.

The output from the power amplifier is connected to the PCB which is shown in Fig. 3.2c. An annealed 1%Silicon-99%Aluminum (1%SiAl) wire with 32 microns in diameter, 1-4% in elongation and 19-21g in tensile strength is used to connect between the PCB and Input IDT via wire bonding. One of the major reasons to use 1%SiAl wires instead of gold or copper wires is the former wires have a 95% success rate in wire bonding and it can easily be bonded to gold, copper, aluminum and even bare silicon surface. The signal coming from Output IDT is observed continuously with Agilent Technologies E4401B spectrum analyzer (see Fig. 3.1).

3.5. PL and PLE Measurement

PL (photo-luminescent) measurement is continuous wave (CW) measurement that can be performed at both room and cryogenic temperatures. In this measurement, the optical field at 532nm (green) with a constant power is applied to the NV center to excite the electrons from the ground state and measure the number of photons coming out of the system as spontaneous emission when excited electrons returns to the ground state. By steering the 532nm (green) laser field with a 2D rotating mirror galvanometer, we can scan the surface of the diamond sample to profile the density of the NV-center of the diamond sample.

PLE (photo-luminescent excitation) is pulsed wave measurement which can only be performed at cryogenic because it is a resonant excitation and at room temperature,

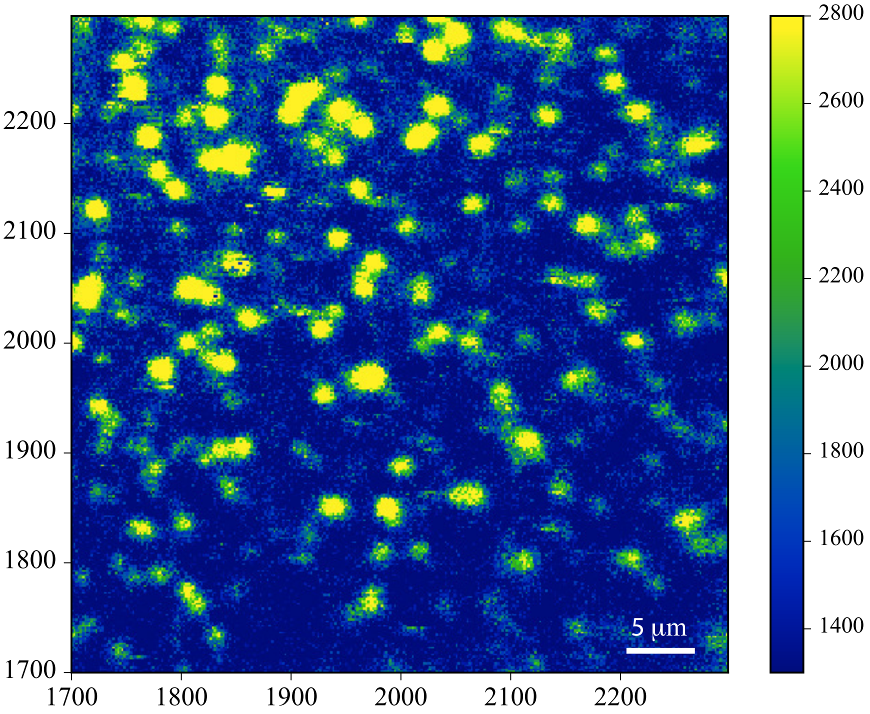

FIGURE 3.5. Scanned confocal microscope image showing implanted individual NV centers

the phonon side band is too broad to do a measurement. Even though the PL experiment is crucial for indentifying the individual NV-center and it is the very first measurement to be performed in most of NV center experiment, most of NV-center measurements on this are done by PLE measurement as it is the only way to access individual energy levels.

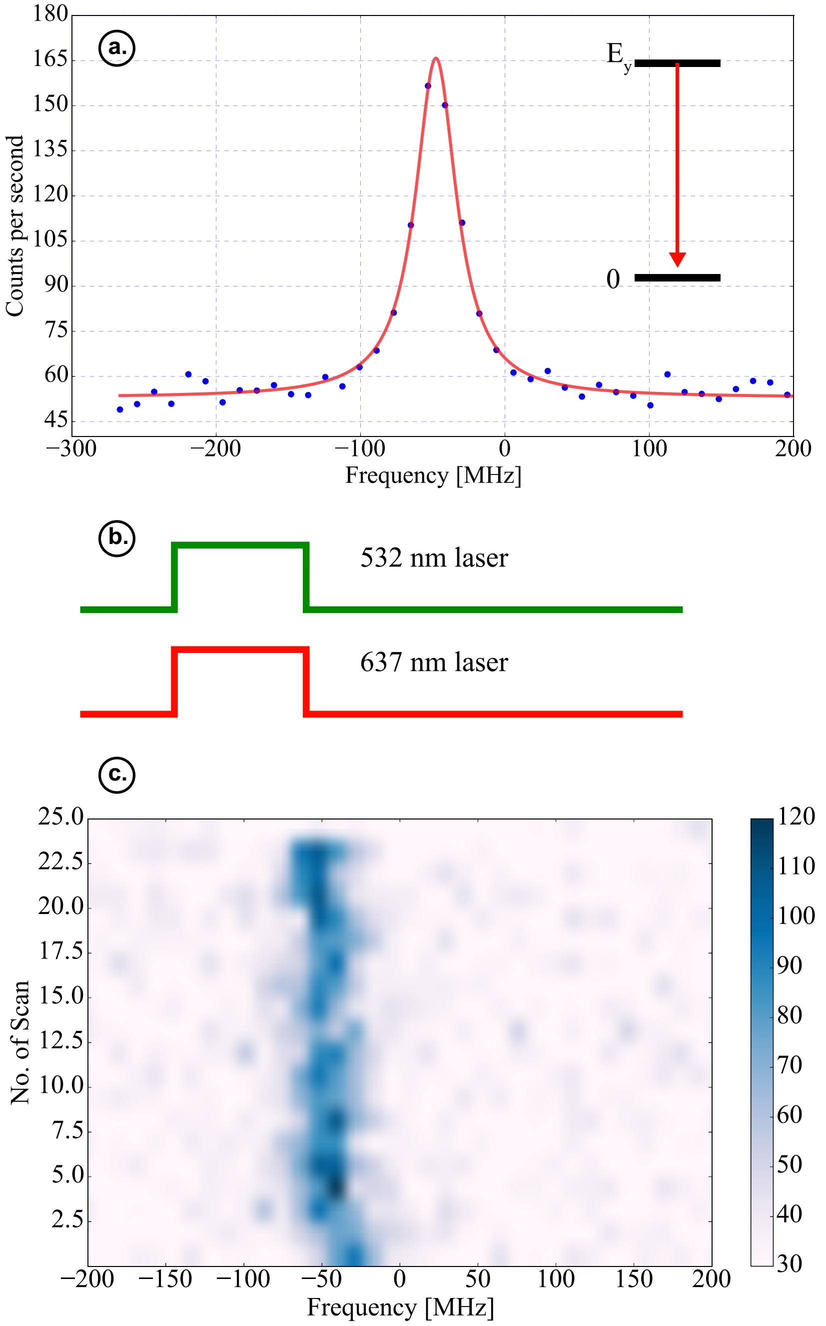

FIGURE 3.6. (a) The averaged spectrum of 25 PLE scans and (c) multiple successive scans with respect to the detuning of the resonant E_y transition frequency, and (b) pulse sequence for PLE scans, in which a green laser is used to repump to reinitialize the system and a red laser is for measurement.

CHAPTER IV

FABRICATION OF NV CENTER IN DIAMOND

4.1. Introduction

As mentioned, the electronic spins in the nitrogen-vacancy (NV) center have been demonstrated to be nanoscale probes in the wide range of applications in magnetometry[40, 41], magnetic imaging[41–43], electric-field sensing[44], and thermometry[45, 46] . However, limitations still exist in applications such as nuclear spin imaging and external spin entanglement[47, 48] due to the weak magnetic dipole interaction in which the coupling strength decreases with distance (r) as $1/r^3$. A simple way to solve this issue is to create a NV center closer to the surface of the diamond so that a single external electron and a proximal nuclear spin can be detected with higher sensitivity through the use of any receiver such as a ferromagnetic or atomic force microscopy[49] (AFM) tip. Ion implantation[50–56] and the delta-doping[57] method are proven to achieve near surface NV centers in diamond.

4.2. Ion Implantation

Ion implantation is a process in which the energetic ions are injected into the targeted substrate which changes the electrical and physical properties of the substrate. In this process, the source gases, in our case is nitrogen gas, are initially ionized in an electrical discharge in the vacuum chamber. These extracted ions are ordered in accordance with their atomic mass in a magnetic field, i.e., by magnetic mass spectrometry. Then, these ions are boosted up to the desired energy and

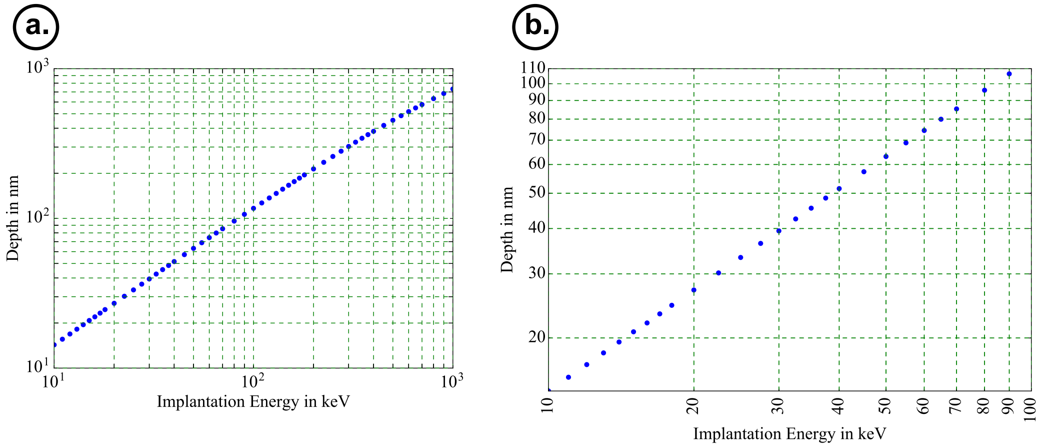

FIGURE 4.1. Average depth of the implanted $^{15}N^{+}$ to the diamond sample as a function of ion energy (simulated with SRIM) represented in (a) the full energy range and (b) the zoom-in to focus the energy range used in this thesis.

released to the targeted substrate, which in our case is the diamond sample. Ion implantation is well-documented industrial process that allows precise control of the dose and depth profile. Depending on the energy dose, the depth of NV center can be easily calculated with SRIM[58] (The **S**topping and **R**ange of **I**ons in **M**atter) software. (See Fig. 4.1) It also has excellent lateral dose uniformity with less than 1% variation across 12″ wafer. And it is also less sensitive to surface cleaning processes. Implanted ions generally causes damage to the crystal lattice along the path into the substrate by displacing atoms from their lattice sites. Therefore, an elevated temperature annealing process is usually followed up to restore crystallographic order in the lattice.

4.3. NV Center Creation via Ion Implantation

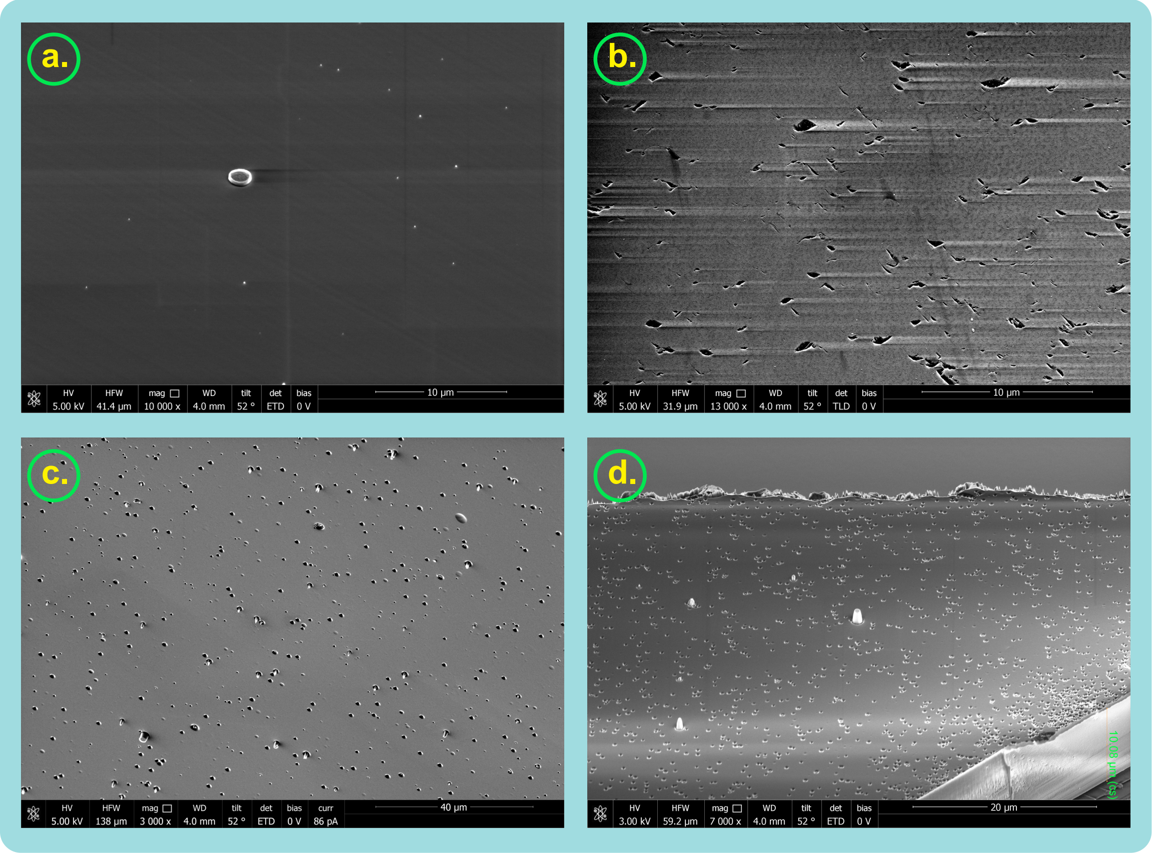

FIGURE 4.2. Scanning Electron Microscope (SEM) images of parts-per-billion and parts-per-million diamond sample: (a) a sciafe-polished surface of the ppb-sample and (b) a chipping and pitting surface of the ppm-sample. (c) The smooth surface shown in (a) becomes rough and pitted after Oxygen plasma etch with the graphite wafer clamp. (d) The same issue can be seen on the surface of the 10μm thin diamond membrane. It is concluded that the graphite wafer clamp is the reason for this roughness. A few nanometers of carbon are deposited on the diamond sample as an anti-charging layer before the SEM images are taken.

4.3.1. Surface Preparation

Ion implantation process is one of the most common techniques for creating color centers in diamond. For this process, we follow the recipe mentioned in this paper.[50] We start with a single crystal diamond from Element Six (E6) which is presumably polished along what is known as the “easy axis” (essentially along the in-plane [100] crystallographic direction). Polishing along the easy axis can minimize the surface damage resulting from the mechanical nature of the process and this polishing process can give the surface as smooth as >1nm in surface roughness. Polishing off the easy axis will make the surface chip and pit, but these cannot be detected easily. The significance of easy axis polishing will be explained in details below when we discuss the surface preparation with induced coupled plasma reactive ion (ICP-RIE) etching.

First, to remove damages due to mechanical polishing, we must etch several microns of diamond from the surface by applying ICP-RIE etching. We start with a 1:1:1 ratio of concentrated sulfuric, nitric and perchloric acid (so called tri-acid) to clean the diamond for about two hours at 380 °C. Perchloric acid can be dangerous and we only need to use 10mL of it thank to the home-built distillation setup.

After this, we perform the standard piranha which is a 3:1 mixture of concentrated sulfuric acid with hydrogen peroxide for 10 mins and then, rinse in several cups of deionized (DI) water. Next we sonicate the diamond sample in acetone, then methanol, then isopropanol (IPA) and eventually rinse with DI water. Usually the diamond sample placed in an aluminum sample holder is dried out inside the oven at 200 °C. A nitrogen blow-dry is not a suitable method for such a small sample.

The final step is to remove the top surface of the diamond sample because it is generally damaged and highly strained from the mechanical polishing process. When thermal annealing is eventually performed after ion implantation, these damage can cause undesirable vacancies with broad linewidth and low fluorescence intensity. We use ICP-RIE dry etching with Oxford Plasma Pro80 Plus to remove several microns of the top surface of the diamond. To achieve a high quality smooth surface ($<$ 1nm RMS surface roughness), the diamond must to be initially sciafe-polished (the so called the easy-axis mechanical polish). Parts-per-million (PPM) diamond samples from Element Six (E6) are not sciafe-polished. Therefore, pitting and chipping on the surface of these samples appear via the optical microscope. After the ICP-RIE etching with Oxygen plasma on these samples, pitting and chipping get worse and even the profilometer's tip cannot travel along the surface on these samples due to the roughness. A diamond sample with dimensions 4mmx4mmx500μm in is attached to a 2$''$ sapphire wafer with 430nm in thickness by bonding with PMMA or crystal bond. Both can dissolve in acetone to reattach from the carrier wafer. Here, the sapphire wafer is used as a carrier wafer instead of the silicon/silica wafer because sapphire is etched much less than silicon/silica during ICP-RIE etching; thus, so there are fewer unwanted compounds in the plasma cloud. Even though crystal bond is recommended for better thermal conductivity than PMMA, we don't find any significant advantage on surface smoothness after the etching. For Oxford Plasma Pro80 Plus, the carrier wafer's thickness must be between 400nm and 500nm to work well with helium backside cooling.

Oxford Plasma Pro80 Plus comes with a $\sim 8.6''$ graphite plate for wafer clamping. We could not achieve a high quality smooth surface with Oxygen plasma etching because Oxygen plasma also etches the graphite plate at the same time and the graphite plate itself is not 100% pure graphite which cause depositing undesirable particles as masks on the surface. Therefore, we designed and machined an alumina (Al_2O_3) ceramic plate as a wafer clamp, which immediately solves the issue.

Before we start any diamond etching, we perform a long and thorough chamber clean because we conduct both Plasma-enhanced chemical vapor deposition (PECVD) and ICP-RIE inside the same chamber. We run a four-hour cleaning recipe with the following parameters: ICP:500 W, RF:20 W, O_2:30-50 sccm and chamber pressure: 93 mTorr for 20 mins, 80 mTorr for 20 mins, 70 mTorr for 20 mins, 60 mTorr for 20 mins, 50 mTorr for 20 mins, 40 mTorr for 20 mins, 30 mTorr for 20 mins, 20 mTorr for 20 mins, 10 mTorr for 20 mins, 5 mTorr for 20 mins, and then, finally 20 mTorr for

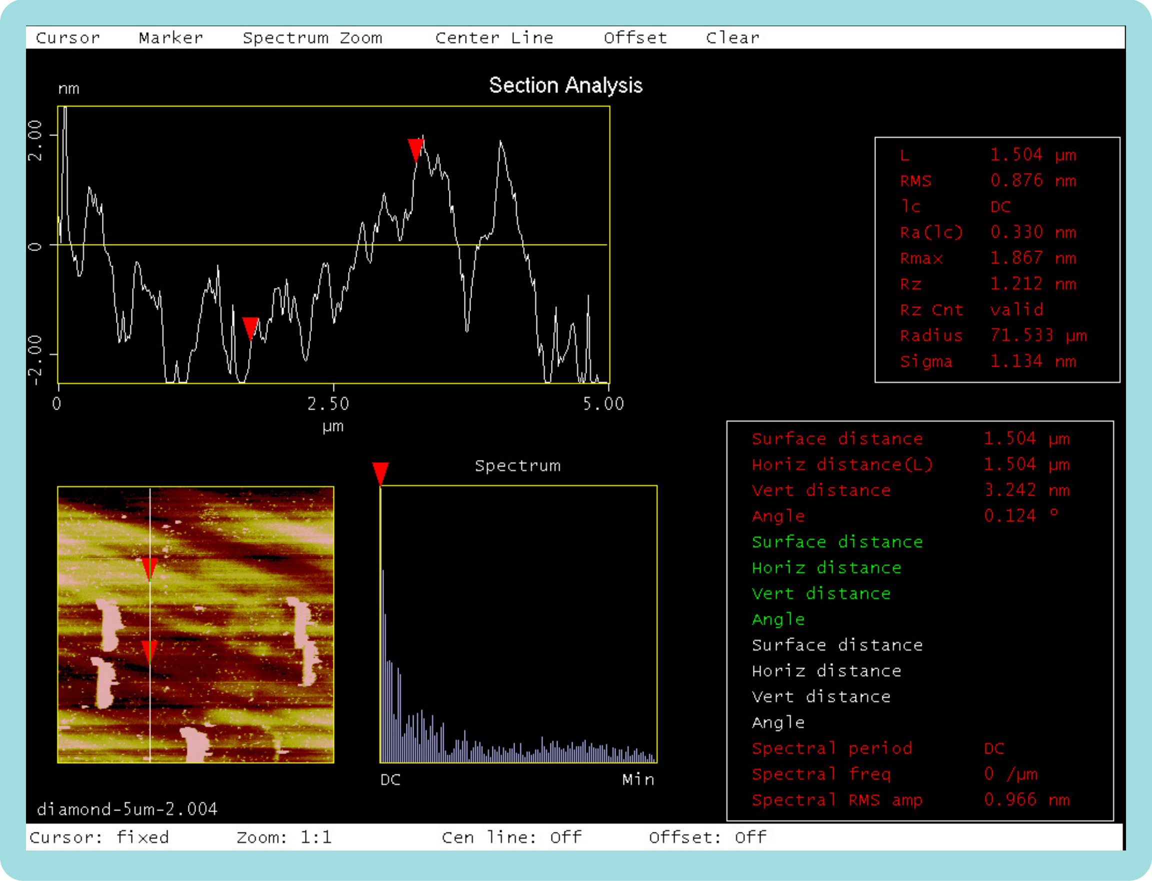

```
L           1.504 µm
RMS         0.876 nm
lc          DC
Ra(lc)      0.330 nm
Rmax        1.867 nm
Rz          1.212 nm
Rz Cnt      valid
Radius      71.533 µm
Sigma       1.134 nm
```

```
Surface distance      1.504 µm
Horiz distance(L)     1.504 µm
Vert distance         3.242 nm
Angle                 0.124 °
Surface distance
Horiz distance
Vert distance
Angle
Surface distance
Horiz distance
Vert distance
Angle
Spectral period       DC
Spectral freq         0 /µm
Spectral RMS amp      0.966 nm
```

```
diamond-5um-2.004
Cursor: fixed       Zoom: 1:1        Cen line: Off      Offset: Off
```

FIGURE 4.3. The surface roughness is measured by an AFM scan and the roughness is less than 1nm RMS. There are some dust particles on the surface because the measurement is taken at open air.

40 mins. Instead of running the whole recipe once, I broke it down into two sequences and during these sequence, I added a step to cool down the wafer to ∼17°C. This cleaning process is a long process and so, ICP plasma gradually heats up the diamond sample and it is good to have a cooling step in the recipe. In the cooling step, we ensure the diamond sample return to ∼17°C before we perform another sequence.

For plasma etching/cleaning, we begin a 49 minute etch with the following parameters: ICP:280 W, RF:210 W, Ar flow rate:10 sccm, Cl_2 flow rate:16 sccm, and chamber pressure:5 mTorr, followed by a second a 60 minute etch with the following parameters: ICP:420 W, RF:60 W, O_2:30 sccm and chamber pressure:10 mTorr. The first process is broken down into two 24-minute-sequences with the extra cooling step. The second recipe is also divided into four 15-minute-sequences with extra cooling steps. A >1nm RMS surface roughness is measured through an AFM scan (shown in Fig. 4.3)after the ICP-RIE surface treatment is performed. The etching rate for the Ar/Cl recipe is about 40nm per minute while the O_2 recipe is about 100nm per minute.

4.3.2. Ion Implantation with $^{15}N^+$ on diamond

$^{14}N^+$ vacancy center with spin=1 is ubiquitous in diamond even though the concentration could be varied among samples. To distinguish a naturally occuring NV center due to $^{14}N^+$, we decided to implant $^{15}N^+$ ions with spin=1/2. We use $^{15}N^+$ at 60 keV and 85 keV with varying doses to generate the near surface NV centers in diamond. According to the SRIM simulation, the stopping depth of 60 keV and 85 keV would be 75 nm and 100 nm respectively (See Fig. 4.1b). While the energy of the ions defines how far the ions will penetrate into the diamond, the dose which is in a unit of ions/cm^2 determines the density of $^{15}N^+$ and, ultimately the density of the NV centers. We implant in a variety of doses ranging from 10^9 /cm^2 and 10^{10} /cm^2.

In general, any ion implantation[59] process is followed by high temperature annealing as mentioned before. In recent years, research has be done on annealing the diamond at different temperatures, ranging from 428 °C to 1200 °C. According to this recipe, we anneal the implanted diamond at 400 °C for four hours, 800 °C at four hours, and 1200 °C at two hours, with a one hour ramp-up time to each temperature transition. The reason for the long ramp up time is to maintain high vacuum (Pressure 10^{-6} Torr) through out the entire annealing process. The reasons for annealing at these certain temperatures are as follows: at 400 °C, the self-interstitial defect is

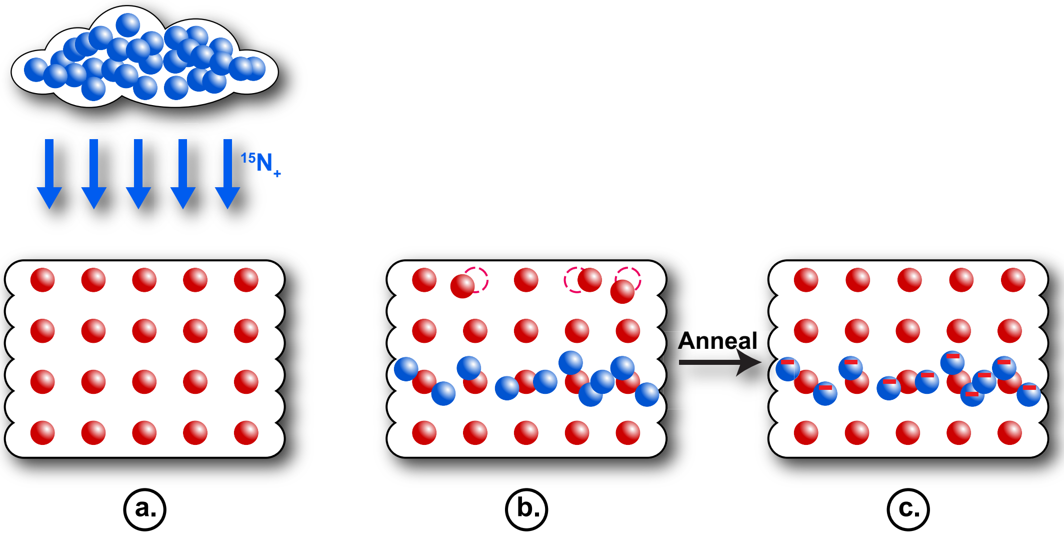

FIGURE 4.4. Ion Implantation with $^{15}N^{+}$ on Diamond. (a) $^{15}N^{+}$ ions are injected into the diamond. (b) The ions stop at a certain distance depending on their kinetic energy. And implanted ions make damage to the crystal lattice by displacing atoms from their lattice sites. (c) High temperature annealing is required to restore crystallographic order in lattice sites.

mobile and anneals out with vacancies so that they annihilate each other; at 800 , the vacancies are allowed to mobilize and unite with substitutional nitrogen atom (mostly 15) as shown in Fig. 4.4c; at 1200 , the T_2 coherent time is substantially increased while the fraction of NVs converting from NV^{-} to NV^{0} is largely reduced. ~2 hour tri-acid cleaning is used to remove the graphitized layer generated by annealing at 800 and above.

4.3.3. X-ray Photoelectron Spectroscopy

In every step of the creation of NV centers via ion implantation, the diamond surface is thoroughly monitored by using X-ray photoelectron spectroscopy (XPS) with a high performance Thermo Scientific ESCALAB 250 system. XPS is fundamentally established on the principle of photoelectric effect. XPS analyzes photo-ionization and energy-dispersion of the emitted photoelectrons ejected from

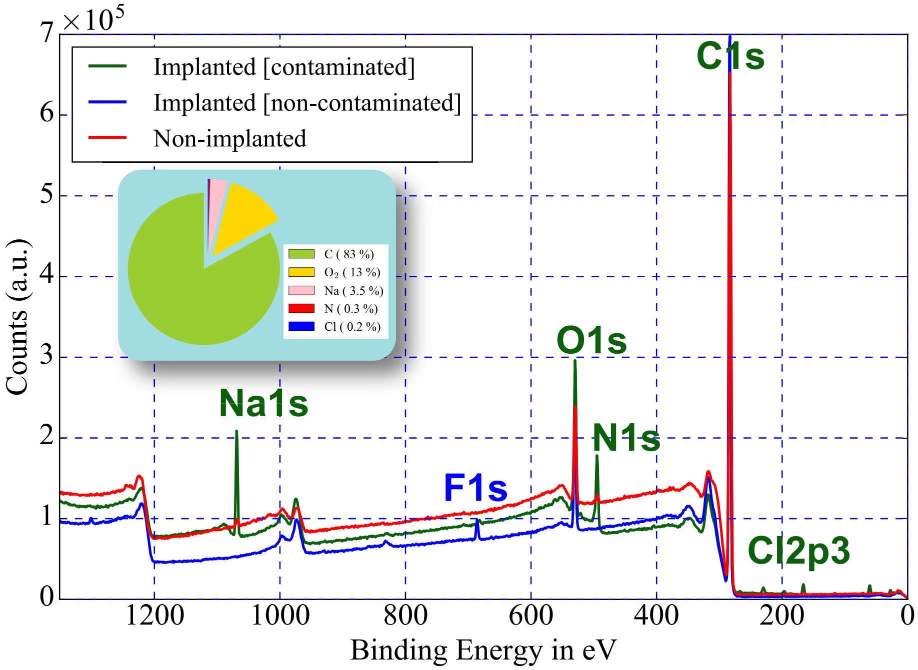

FIGURE 4.5. Comparison of XPS survey scans between the implanted sample with $^{15}N^+$ ions and non-implanted one. This specific sample unfortunately is contaminated with sodium which comes from the implantation chamber, whereas chlorine comes from the ICP-RIE chamber.

the surface via irradiation by X-rays. For instance, we can qualitatively distinguish graphite (sp^2 energy binding) from diamond (sp^3 energy binding) even though they both are made of carbon. We use XPS to ensure the surface is clean, properly oxygen-terminated after Oxygen plasma etch, and free of contaminants such as sodium and chlorine. The possible contamination due to sodium comes from ion implantation process where the process chamber and vacuum parts are usually cleaned with small beads. These beads contains a high percentage of sodium.

Unfortunately, we found some contaminated sample and showed an XPS scan on one of the contaminated samples in Fig. As the figure shows, oxygen termination did not completely remove chlorine and at the same time, we get sodium contaminants.

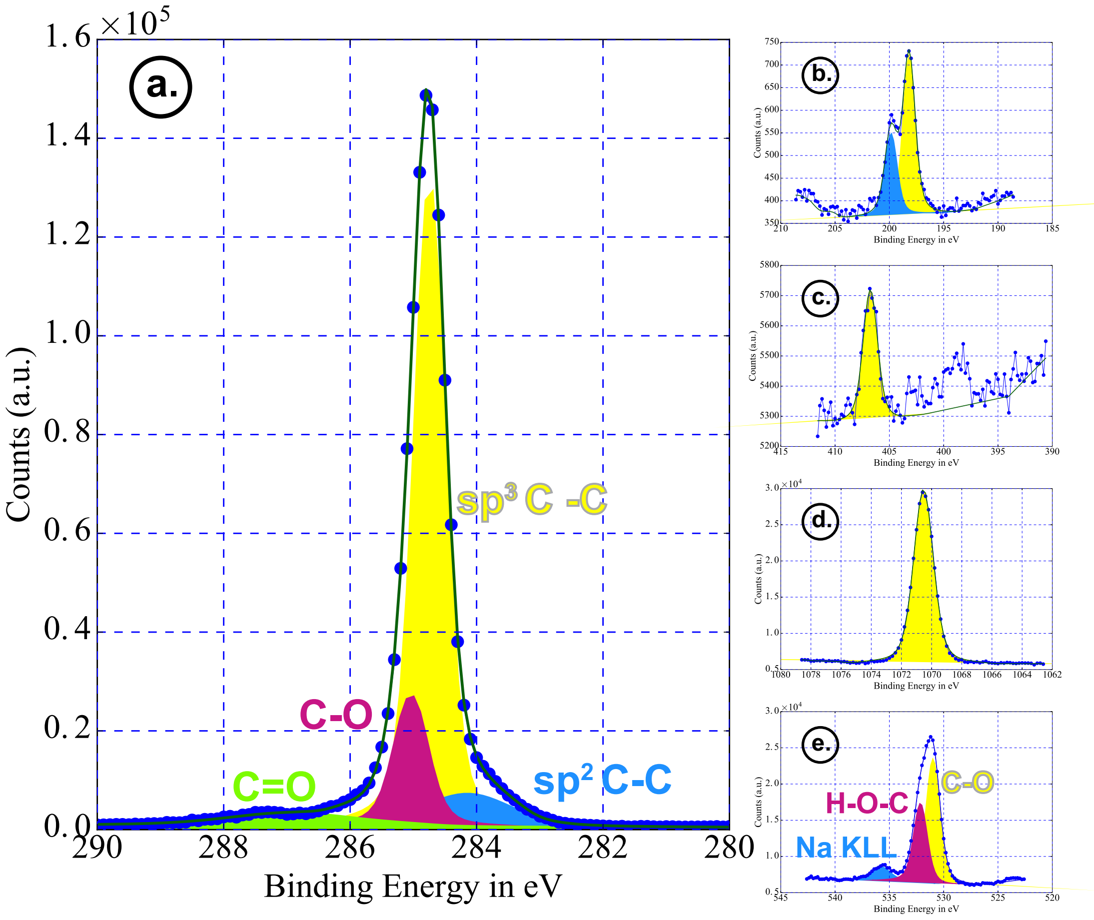

FIGURE 4.6. With fine XPS regional scans, we can identify the types of the bonding and quantify the amount of contaminants contained.Regional scans for (a) carbon, (b) chlorine, (c) nitrogen, (d) sodium and (e) oxygen.

To eliminate chlorine residues, we perform longer (75 minute) oxygen plasma etch. To eliminate sodium contaminants, we requested Innovion Corp.,where we send all our samples for implantation, to scan the source plasma to verify no sodium prior to the implantation. Using XPS analysis, we can not only narrow down the origins of the contaminants and quantify the percentage of contaminants contained (See Fig. 4.6). In the contaminated sample, the percentage of sodium contaminants were relatively quite higher than those for nitrogen as shown in Fig. 4.5. After the final annealing process, we have difficulties in finding good NV centers with a reasonable spectral diffusion (<500 MHz PLE linewidth). We can also conclude from XPS data that the oxygen surface termination process is working well. In the non-contaminated sample, there is also a fluorine peak which is due to the ICP-RIE chamber cleaning recipe which includes 50sccm of O_2 and 50sccm of SF_6. At this point, we are focusing only on oxygen surface termination; therefore, we no longer use the O_2:SF_6 recipe for the chamber cleaning. Instead, we run a thorough O_2 chamber cleaning recipe mentioned in Subsection 4.3.1.

CHAPTER V

NANOMECHANICAL RESONATORS

5.1. Introduction

Nanomechanical resonators[60–62] possess a wide range of applications in both fundamental and applied sciences. Due to their tiny mass (10^{-15}kg), they are the ideal candidates for studying quantum mechanics in a macroscopic mechanical system such as quantum ground state cooling[63, 64] and quantum state transfer[65, 66]. On the other hand, because of their ultra-high sensitivity in detection ($10^{-18}\frac{m}{\sqrt{Hz}}$), they are also leading candidates for use in the field of commercial application sensors such as accelerometers[67] and gyroscopes[68]. Moreover, these resonators can serve as a quantum transducer[69], by which electron spins can couple to the mechanical degrees of freedom by a magnetic field gradient or electrostatics interaction. Some solid states qubits such as superconducting qubits which do not interact coherently with light will be greatly beneficial because this coupling scheme does not rely on the optical properties of qubits. This could serve as a basic building block for many quantum communication applications.

Both silicon nitride (SiN) and diamond resonators not only attain extremely low masses[62] ($\sim 10^{-15}kg$) but also mechanical resonant frequencies ranging from a few megahertz up to gigahertz. These resonators are at least a thousand times lighter than whispering gallery mode (WGM) resonators. Moreover, both resonators are known for achieving ultra high mechanical quality factors[70, 71]. Unlike WGM or diamond resonators, SiN resonators are open to chip-scale nanofabrication making them extremely promising candidates for commercial sensing applications.

On the other hand, diamond resonators possess many material advantages over SiN or other resonators, including high Young's Modulus, high thermal conductivity and low intrinsic dissipation[72]. Moreover, their immunity to strong chemicals makes it possible to use them over an extended period of time by repeatedly cleaning them with strong acids when they become degraded by moisture and dust from their environment.

5.2. Transverse Vibration of Mechanical Resonators

First, eigenfrequencies of mechanical modes of nano mechanical resonators are studied using Euler-Bernoulli beam theory which is based on two major assumptions: plane sections of the resonator beams remain plane and perpendicular to the natural axis before and after the deflection as a result of mechanical motion, and the material is linearly elastic according to Hooke's law[73]. These assumptions are empirically reasonable for our case, in which the length of a resonator is at least thirty times longer than either its width or thickness.

Starting with geometrical deflection of any point on a resonator, we can reach to the moment curvature relation shown in Eq.(5.1). where the geometrical properties of the beam are related to its material properties in terms of modulus of elasticity.

$$M \;=\; E\,I\,\frac{\partial^2 w}{\partial x^2} \tag{5.1}$$

Here, $w(x,t)$ is the deflection of the oscillator from its natural axis which is perpendicular to the length of the oscillator. I is area (second) moment of inertia with the unit of dimension as length to fourth power. M is the bending moment or torque in the transverse direction of the oscillator and E is the Young's Modulus of elasticity of the material. Moreover, we can write the equilibrium condition for force and bending moment due to mechanical deflection as shown in Eq.(5.2).

$$\sum F \;=\; 0 \qquad\qquad \sum M \;=\; 0 \tag{5.2}$$

Combing Eq.(5.1) and Eq.(5.2), we can get the fourth order differential equation of motion for the oscillator beam Eq.(5.3a), and using separation of variables, the solution is calculated as Eq.(5.3b).

$$\frac{\partial^4 w}{\partial x^4} \;=\; -\frac{1}{a^2}\,\frac{\partial^2 w}{\partial t^2} \qquad \text{where } a = \sqrt{\frac{E\,I}{\rho\,A}}, \tag{5.3a}$$

ρ = density of material, and A = cross sectional area of the beam.

$$\Psi \;=\; C_1\, sin\, kx \;+\; C_2\, cos\, kx + C_3\, sinh\, kx \;+\; C_4\, cosh\, kx \tag{5.3b}$$

Using the following boundary conditions,

For doubly clamped beam

$$\Psi|_{x=0} \;=\; 0 \;\; (\text{ No Deflection })$$

$$\Psi|_{x=l} \;=\; 0$$

$$\left.\frac{d\Psi}{dx}\right|_{x=0} \;=\; 0 \;\; (\text{ No Slope })$$

$$\left.\frac{d\Psi}{dx}\right|_{x=l} \;=\; 0$$

For cantilevers

$$\Psi|_{x=0} \;=\; 0 \;\; (\text{ No Deflection })$$

$$\left.\frac{d\Psi}{dx}\right|_{x=0} \;=\; 0 \;\; (\text{ No Slope })$$

$$\left.\frac{d^2\Psi}{dx^2}\right|_{x=l} \;=\; 0 \;\; (\text{ No Bending Moment })$$

$$\left.\frac{d^3\Psi}{dx^3}\right|_{x=l} \;=\; 0 \;\; (\text{ No Shearing Force })$$

the eigenfrequencies (ω) of the nano oscillator are

$$\omega \;=\; \frac{n^2}{l^2}\sqrt{\frac{E\,I}{\rho\,A}} \tag{5.4}$$

where $n = 4.73, 7.853, ...$ for doubly clamped beams, and $n = 1.87, 4.694, ...$ for cantilevers depending on the order of mechanical modes.

For 3D finite element method (FEM) modeling, COMSOL software is extensively used. Simulation of in-plane and out-of-plane transverse modes of both cantilevers and beams are shown in Fig.5.1 and Fig.5.2. The eigenfrequencies of transverse mechanical modes of diamond resonators with density (ρ) 3500 kg/m^3, and a Young's Modulus of 100 GPa are calculated using FEM models as shown in Fig.5.3. They are inversely proportional to the length (l) square of mechanical resonators as we discussed earlier using Euler-Bernoulli beam theory. The first order (red) and third order (blue) mechanical modes in Fig.5.3 represent the out-of-plane transverse motion while the second order (green) represent in-plane transverse motion. FEM modeling would be quite instrumental for studying more complex structures in order to tailor the desired mechanical frequencies and mode distribution for optomechanical systems.

The experimental measurement of the first order transverse mechanical modes of these two diamond resonators presented in Fig.5.3 is shown in Fig.5.12 and is in a good agreement with both Euler Bernoulli theory and FEM simulation.

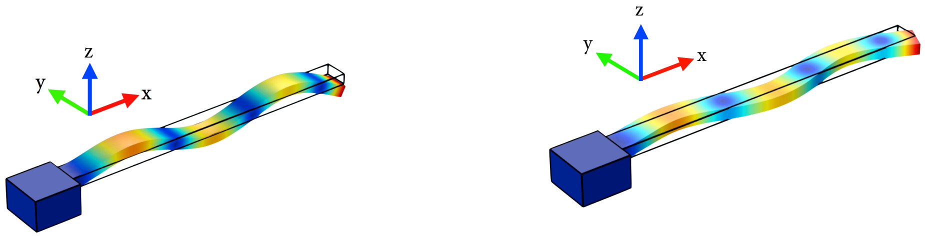

(a) (b)

FIGURE 5.1. (a) In-plane and (b) out-of-plane transverse modes of cantilevers

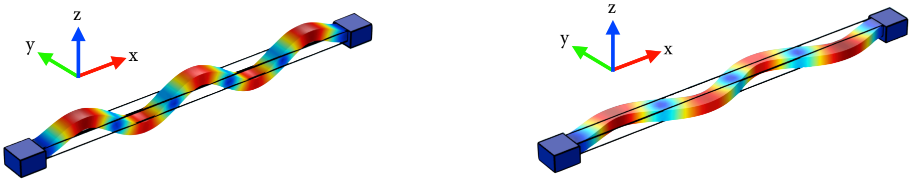

(a) (b)

FIGURE 5.2. (a) In-plane and (b) out-of-plane transverse modes of beams

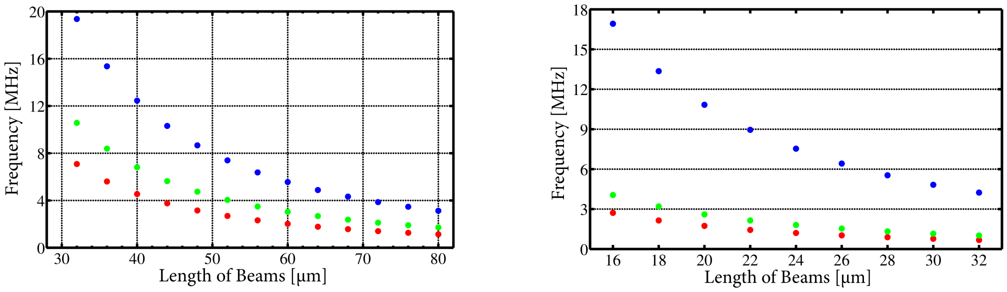

(a) (b)

FIGURE 5.3. Finite element method simulation of first three transverse mechanical modes of (a) a doubly clamped diamond oscillator with rectangular cross-sectional dimensions (2 μm x 1.3 μm), and (b) cantilevers with dimensions (1.53 μm x 0.7 μm)

5.3. Fabrication of SiN and Diamond resonators

5.3.1. Fabrication of SiN resonators

First, the silicon wafer of thickness 500um is prepared with two layers: 3um thickness of silicon oxide and 100-200nm of silicon nitride. Silicon dioxide is thermally grown on top of the silicon wafer to serve as a sacrificial layer. On top of the silicon dioxide layer,a high stress silicon nitride layer is deposited via low pressure chemical vapor deposition (**LPCVD**). Then, a 400nm PMMA(polymethyl methacrylate) layer is spin-coated on top of the silicon nitride layer to be a mask for later etching. Electron beam lithography is used to write the nano oscillator patterns followed by reactive ion etching with CHF_3 (Fluoroform) for 15 min. Hydrofluoric wet etching is applied to under-cut and release the silicon nitride beam from the silicon wafer by removing silicon dioxide. In the final step, the wafer is cleaned with piranha solution, which is a mixture of sulfuric acid (H_2SO_4) and hydrogen peroxide (H_2O_2), to remove most organic matter preventing unnecessary mechanical dissipation. The detailed steps[62] are shown in Fig.5.4.

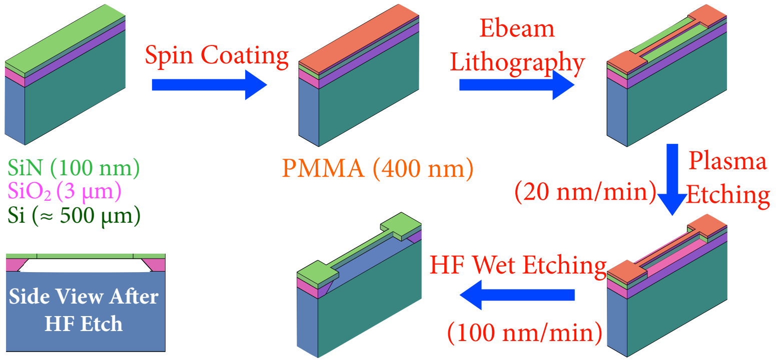

FIGURE 5.4. A step-by-step fabrication process of SiN resonators PMMA(polymethyl methacrylate) layer is spin-coated on top of the silicon nitride layer. Electron beam lithography is used to write the nano oscillator patterns followed by reactive ion etching with CHF3 (Fluoroform) for 15 min to remove silicon nitride while PMMA layer is used as a mask. Hydrofluoric wet etching is applied to under-cut and release the silicon nitride beam from the silicon wafer by removing silicon dioxide.

(a) (b)

FIGURE 5.5. Optical images of (a) a (45μm x 3μm x 100nm) silicon nitride beam and (b) arrays of beams fabricated by using the process shown in Fig. 5.4.

5.3.2. Fabrication of Diamond Resonators Using FIB

Thin diamond film bonded with silicon wafer is not commercially available like in the case of SiN fabrication. Therefore , the fabrication process for diamond resonators is completely different from SiN resonators. So far, 3-dimensional focused ion beam (**FIB**) milling[74] is the only way given our limited accessibility and usually takes about 15-20 hours to make a single diamond oscillator. First, a 4x4x2mm bulk diamond sample is mounted in a 45° mount on a five-axis stage which is capable of in-situ (compu-centric) rotation in the FIB chamber. Most of the diamond beams are usually made out of the edge of a bulk diamond so that both the top surface and the side wall of the diamond oscillator can be easily accessed throughout the fabrication process instead of taking out the sample and physically rotating it. A gallium ion beam of 30kV with programmable current density (1pA-20nA/cm^2) is rastered across the bulk diamond sample at the pixel dwell time 1μs and 50% pixel overlap. To avoid damage due to the ion beam, three different levels of current density are applied for raw cutting, fine cutting and final polishing. Two long trenchs of 40μm long, 5μm deep, and 4-5 μm wide are milled into the top surface of the diamond crystal with current density at 690pA/cm^2. After that, the bulk diamond is rotated so that the side wall is now facing the Gallium ion beam and another trench of 40μm long, 8μm deep, and 2-3 μm wide is milled with lower current density(350pA/cm^2) to release the diamond beam out of the bulk diamond (Fig.5.6). For the final polishing step, 100pA/cm^2 surface-cleaning step is applied to all four surfaces of the diamond beam.

It is essential to point out that both the top surface of the beam and the top surface of the bulk diamond, which is underneath of the beam, should be smooth and parallel to each other so that the interference signal is strong enough to be revealed in a spectrum analyzer. Even though FIB milling is a lengthy (12-18 hours) and delicate process, this can literally mill any three dimensional design while traditional semiconductor fabrication methods cannot access beyond two dimensions.

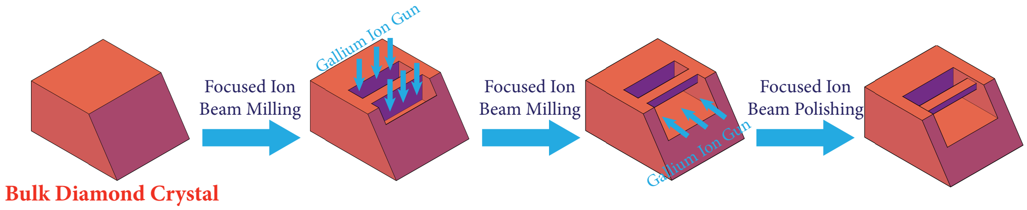

FIGURE 5.6. Focused Ion Beam milling of diamond resonators. A commercially available high purity diamond from Element Six is mounted at 45° on a five-axis stage which is capable of in-situ (compu-centric) rotation to make 3D milling possible.

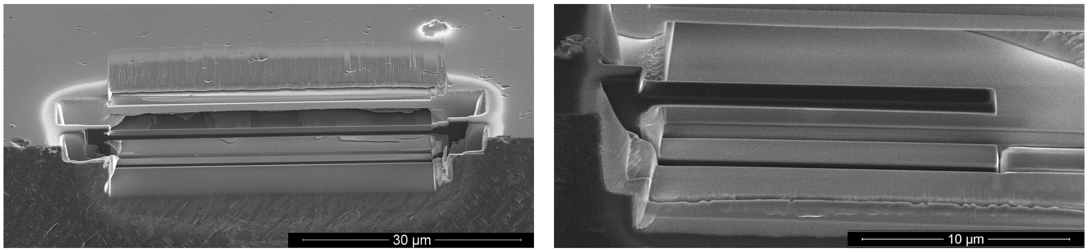

(a) (b)

FIGURE 5.7. SEM images of (a) a (40μm x 2μm x 1.3μm) diamond beam and (b) (16μm x 1.53μm x 0.7μm) diamond cantilever which are tilted at 45° . These two resonators are fabricated by milling with FIB. Several different milling configurations are used to acquire a perfect smooth surface and to avoid redeposition from milling.

5.3.3. Fabrication of On-chip Diamond Resonators

For this process, we started with the electronic grade bulk diamond from Element Six (E6). The bulk diamond generally has a dimension of 4mm × 4mm and thickness is about 500 μm. First, we send the bulk diamond to Applied Diamond/Delaware Diamond Knives where it is sliced and mechanically polished into 50 μm thin membranes. A single bulk diamond with the thickness of 500μm can be sliced into three 4mm × 4mm × 50μ membranes.

To achieve a high quality mechanical oscillator, the surface preparation is very critical. Therefore, before we fabricate diamond mechanical resonators, we follow a series of surface preparation steps to clean the surface and remove a few microns of strained diamond resulting from the mechanical polishing. These steps are important for any future incorporation of NV-centers with stable fluorescence. I clean the thin diamond membranes in a boiling mixture of sulphuric,nitric and perchloric acid in an equal ratio for 30 minutes to 1 hour. This process removes the residue left on the diamond surface by the mechanical polishing. Then, I apply ICP dry-etch with Ar/Cl2 plasma for 45 minutes to reduce the surface roughness down to less than 1nm RMS. Next, I terminate the diamond surface with oxygen by etching with oxygen plasma for 3-5 minutes. Then, I can start the actual fabrication of a diamond mechanical resonator.

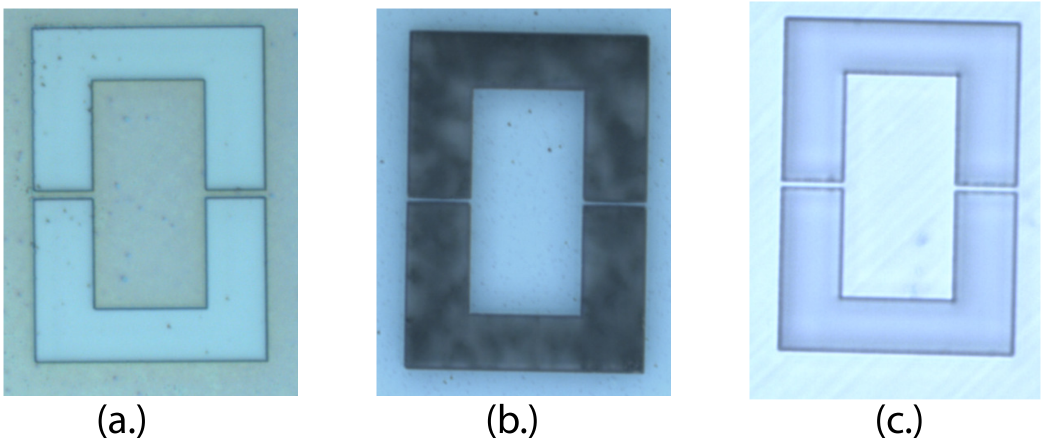

FIGURE 5.8. (a) Transferring a mask by using Ebeam-lithography, (b) Oxygen plasma etching process while protecting a thin diamond with a silicon nitride mask, and (c) an on-chip diamond oscillator.

For the on-chip diamond oscillator fabrication, thin diamond membranes must be mounted on a wafer. I use hydrogen silsesquioxane (HSQ) assisted wafer bonding. HSQ is a flowable oxide. It comes in liquid form and transforms to a solid glass when it is heated to the proper temperature. For the carrier wafer, I use a wafer with the thickness of 1μm-thermal-oxide layer. First, the thermal oxide wafer is cleaned in a piranha solution for 10 minutes followed by a dehydration bake for 10 minutes. After cooling down the wafer, Fox-15 (HSQ) is spin-coated on it for 10 seconds at 2000 rpm. As soon as the spin-coating process is done, a diamond membrane is placed on top of the freshly HSQ-coated surface. At this point, the diamond membrane is usually attached by van der Waals forces. They are not strongly bonded yet. To be fully bonded, we have to place them on the 6 inch diameter wafer, load them into the wafer bonder and anneal at 450 °C with 50 mTorr for about 3 hours. It is also important to wipe out HSQ liquid overspilled to the other side of the carrier wafer before placing inside the wafer bonder because it becomes dry and partially adhesive to the 6 inch diameter wafer.

The on-chip diamond membrane is approximately 50μm in thickness. Therefore, it is necessary to thin it down to less than 2μm. For this process, we will use ICP dry-etch with Ar/Cl2 plasma with the etching rate of 4.75 μm per minute. To avoid redeposition and masking due to Ar/Cl2 plasma etch on silicon wafer, we use a 75μm think quartz mask which is laser-cut to a slightly smaller dimensions of our on-chip diamond membrane. Silicon wafer is fully protected by the quartz mask during the etching process. This etching process takes about 10 hours. After that, a quick (2-5) minutes oxygen plasma etch to remove a chlorine residue which could cause fluorescence instability in NV centers.

To transfer the desired patterns onto a thin diamond membranes, we develop two-layer mask transfer. The main motivation behind this approach is due to the fact that many varieties of masks such as gold or aluminum may not survive the 2μm-etch of diamond.Therefore, we deposit a 275nm-thick silicon nitride layer using Plasma-enhanced chemical vapor deposition (PECVD) with SiH_4/N2 plasma. Then, 500nm of Poly(methyl methacrylate) (PMMA) layer is spin-coated on top of the silicon nitride layer. We use Ebeam-lithography to transfer the patterns followed by reactive ion etching (RIE) using CHF_3/O_2 plasma. The selectivity between PMMA and silicon nitride is approximately 2:1. The etch rate of silicon nitride is approximately 125nm per minute. We use O_2 plasma to etch the thin diamond layer. The selectivity between silicon nitride and diamond is approximately 30:1. In terms of etching selectivity to diamond, silicon nitride is even better than gold metal mask where it is 10:1 instead of 30:1.

Next, we remove the silicon nitride layer by wet etching using phosphoric acid at 160 °C for 4 minutes. It is also important to point out that the on-chip diamond wafer is dipped into 5:1 buffered HF for a few seconds to strip oxide residue resulting from oxygen plasma etching before using phosphoric acid. Phosphoric acid is intentionally chosen due to the good selectivity between silicon nitride and silicon dioxide with 30:1. Finally, we use 5:1 buffered HF to under-etch silicon dioxide layer and release the diamond resonators.

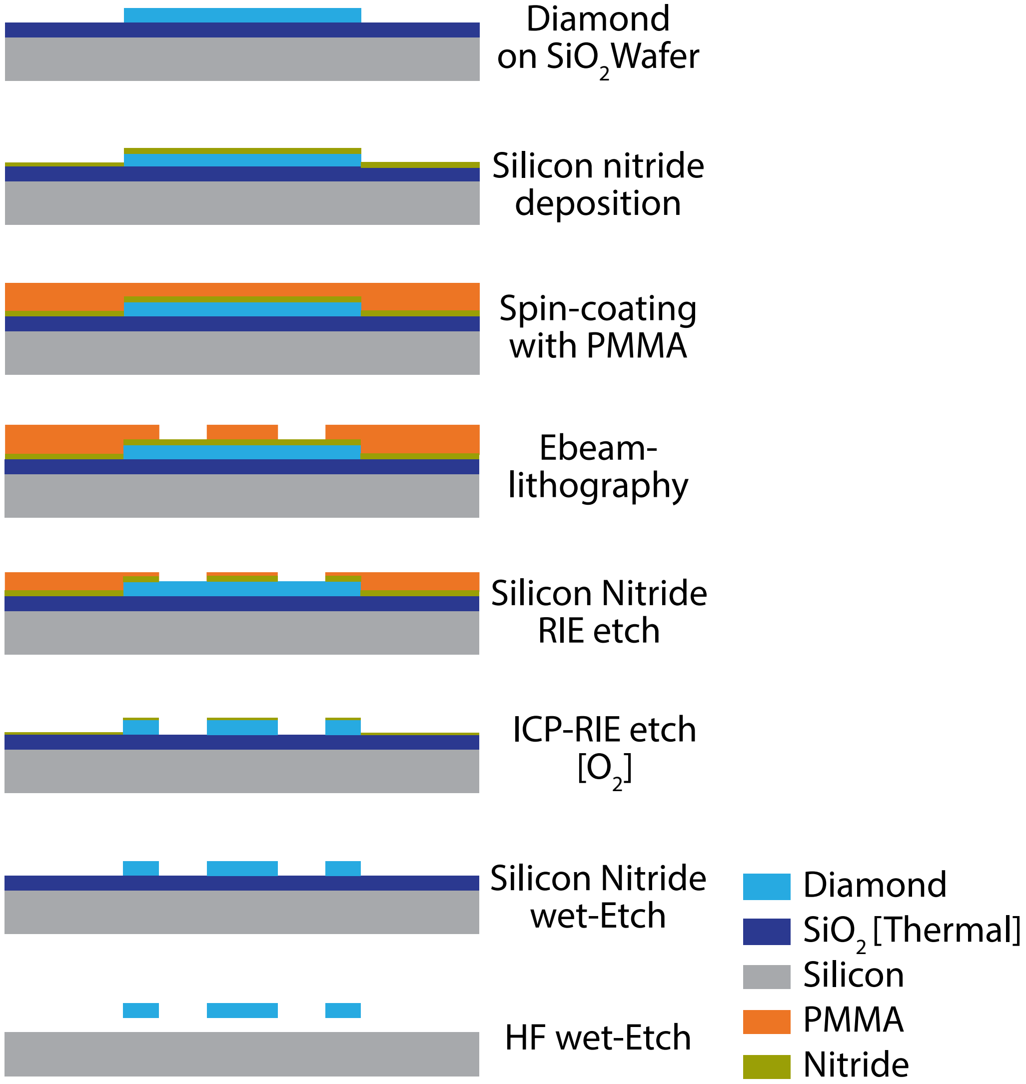

FIGURE 5.9. Fabrication steps for on-chip diamond resonators.

5.4. Experimental Setup

Nanobeam Brownian motion is characterized by optical interferometric phase detection[75, 76]. A focused laser is applied to the nano beam at normal incidence. In the detection scheme, the interference between one light wave (E_S) coming from the partial reflection due to the incident laser on the nano beam and another (E_L)

coming from the substrate — provides ample displacement sensitivity to out-of-plane and in-plane motion of a resonator as described in Eq.(5.5). and Fig.5.11.

$$I \propto |E|^2 = \left|E_L\, e^{i\omega t} + E_S\, e^{i(\delta\phi(t)+\omega t)}\right|^2 = E_L^2 + E_S^2 + 2\, E_L\, E_S\, cos(\delta\phi(t)) \tag{5.5}$$

As shown in Fig.5.10, a 5mW HeNe laser is focused down to a 1-2μm spot with the 20X objective(N.A.=0.42) and sent through the vacuum chamber view port. Light reflected from the sample is taken to a photodiode and the output of the photodiode is attached to a spectrum analyzer where spectrum density of phase fluctuation of a nanobeam is studied. All the measurements are conducted at 10^{-5} torr to avoid mechanical dissipation due to air molecule and room temperature.

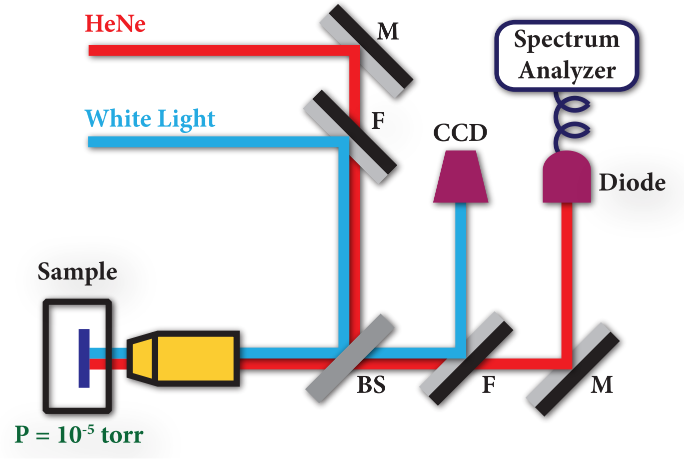

FIGURE 5.10. Optical Interferometric Setup

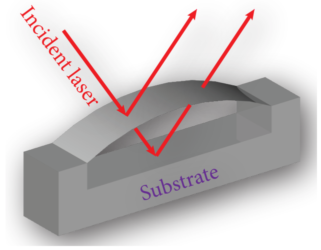

FIGURE 5.11. Interference between two light waves

5.5. Measurement Sensitivity

First, we want to know the amplitude fluctuation of our mechanical resonators, and then compare this Brownian noise signal to the shot noise coming from HeNe laser which is used as a probe in our interferometric measurement. We can model our system as a simple damped harmonic oscillator in a thermal bath with temperature T. Therefore, easily calculate its amplitude using equipartition theorem (shown in Eq.(5.6)) which states that in thermal equilibrium condition, energy is equally distributed among all accessible degrees of freedom of a system.

$$\langle E \rangle = \langle E_{KE} \rangle + \langle E_{PE} \rangle = \frac{1}{2} k_B T + \frac{1}{2} k_B T \tag{5.6a}$$

$$\langle x^2 \rangle = \frac{k_B\, T}{m\, \omega_0^2} \tag{5.6b}$$

$$\sqrt{\langle x^2 \rangle} \approx 10^{-12}\, m \tag{5.6c}$$

Now the question is what are the essential parameters to be able to detect such a tiny fluctuation under a spectrum analyzer and unfortunately, there is measurement imprecision noise (shot-noise) from HeNe laser. As a simple damped harmonic oscillator with a mechanical damping (γ) and mechanical resonant frequency (ω_0), the equation of motion could simply be written as Eq.(5.7), and Eq.(5.8) for its Fourier counterpart. $f(t)$ is the driving force from the thermal bath with temperature T.

$$\ddot{x}(t) + \gamma \dot{x}(t) + \omega_0^2 x(t) = \frac{f(t)}{m} \tag{5.7}$$

$$\tilde{x}(\omega) = \frac{\tilde{f}(\omega)}{m} \frac{1}{\omega_0^2 - \omega^2 + i\gamma\omega} \tag{5.8}$$

The spectral density of thermal amplitude fluctuation can be calculated as $S_{xx}(\omega) = \langle \tilde{x}(\omega)\, \tilde{x}^*(\omega) \rangle$. For thermal bath, $f(t)$ is constant in frequency,

$$S_{xx}(\omega) = \frac{\tilde{f}^2}{m^2} \frac{1}{(\omega_0^2 - \omega^2)^2 + \omega^2\, \gamma^2} \tag{5.9}$$

The driving force $f(t)$ due to a thermal bath can be investigated using Eq.(5.6b), and the Wiener-Khinchin theorem which states that the power spectral density of a wide-sense stationary random process is the Fourier transform of its auto-correlation function. Therefore, the spectral density of amplitude fluctuation can be described as,

$$\begin{aligned} S_{xx}(\omega) &= \int_{-\infty}^{\infty} \langle x(t)\, x^*(t-\tau) \rangle \; e^{-i\omega\tau} \, d\tau \\ \langle x^2 \rangle &= \frac{1}{2\pi} \int_{-\infty}^{\infty} S_{xx}(\omega) d\omega \;=\; \frac{f^{\,2}}{2m^2} \, \frac{1}{\omega_0^2\, \gamma} \end{aligned} \tag{5.10}$$

Substituting Eq.5.6b from Equipartition theorem,

$$f^{\,2} \;=\; 2m\, \gamma\, k_B T \tag{5.11}$$

The driving force due to the thermal Brownian bath is proportional to the bath temperature (T) and the damping rate of the mechanical oscillator as expected. Eventually, substituting this in Eq.5.9 ,

$$S_{xx}(\omega) \;=\; \frac{2k_B T}{m} \, \frac{\gamma}{(\omega_0^2 - \omega^2)^2 \;+\; \omega^2\, \gamma^2} \tag{5.12}$$

This expression is also known as fluctuation dissipation theorem (**FDT**). For a near resonant oscillation , i.e. $\omega_0 \approx \omega$, this can be even further simplified as ,

$$S_{xx}(\omega) \;\approx\; \frac{k_B T}{m\omega_0^2} \, \frac{1}{\gamma} \tag{5.13}$$

From this equation, spectral density of a diamond beam with the dimensions of (40μm x 1.53 μm x 0.7 μm) at room temperature would be estimated to be 3 x 10^{-26} m^2/Hz.

From the optical interferometric measurement, the spectral density of phase fluctuation ($S_{\phi\phi}(\omega)$) is analyzed, not the spectral density of position fluctuation ($S_{xx}(\omega)$). However, spectral density of phase fluctuation of a mechanical oscillator can be derived from the relation between the changes in phase ($\Delta\phi$) and changes in position (Δx) due to the mechanical oscillation.

$$\begin{aligned} \Delta\phi &= \frac{2\pi}{\lambda}\,(2\,\Delta x) \\ S_{\phi\phi}(\omega) &= 4k^2 S_{xx}(\omega) \end{aligned} \tag{5.14}$$

Substituting Eq.(5.13),

$$S_{\phi\phi}(\omega) \approx 4\left(\frac{\omega_L^2}{c^2}\right)\left(\frac{2k_BT}{m}\,\frac{1}{\omega_0^2\gamma}\right) \tag{5.15}$$

To compare the signal-to-noise ratio between thermal Brownian signal and HeNe laser's shot-noise, the spectral density of phase fluctuation of HeNe laser's shot-noise can be calculated based on the number-phase uncertainty principle for coherent states. Based on the power (P=2 mW) of the HeNe laser, the spectral density[77] of its shot-noise is

$$S_{\theta\theta}^{\mathrm{L}} = \frac{1}{4\frac{P}{\hbar\omega_L}} \tag{5.16}$$

Finally, the signal-to-noise ratio of Brownian noise over laser shot-noise can be described as Eq.(5.17).

$$\frac{S_{\phi\phi}(\omega)}{S_{\theta\theta}^{\mathrm{L}}} \approx 16\left(\frac{\omega_L}{\hbar c^2}\right)\left(\frac{2k_BT}{m}\,\frac{1}{\omega_0^2}\right)\frac{P}{\gamma} \tag{5.17}$$

Now the signal-to-noise ratio depends mainly on the power of the HeNe laser and the damping rate of the mechanical oscillator. For one-to-one signal-to-noise ratio, the power of the HeNe laser is required to be as low as 130pW.

The experimental measurement of Brownian motion of a (40μ x 1.53 μm x 0.7 μm) cantilever and a (16μm x 1.53μm x 0.7μm) diamond cantilever is shown in Fig.5.12. The first order out-of plane transverse mechanical mode is approximately 2.66 MHz and the mechanical Q-factor is approximately 20,000 with the linewidth of 130 Hz for the diamond cantilever and 4.7 MHz, Q $\approx$ 10,000, and 230 Hz for the doubly clamped beam. The resonance of the mechanical mode is in agreement with Euler Bernoulli theory. At this point, we can not detect the other mechanical modes other than the first order mode in most of our diamond resonators even though we can see higher order modes in SiN resonators. Using measurement sensitivity analysis discussed in the beginning of this section, the signal-to-noise ratio of SiN and diamond resonators with similar mechanical linewidth, would be mainly dependent on the power of the laser as described in Eq.(5.17). One of the main reasons is the relatively weaker local oscillator signal due to the transparent substrate(bulk diamond) which partially reduces the amount of light coming from it. The larger thickness of the diamond oscillator which is $\sim$10 times thicker than SiN beams, could also make it worse. Therefore, in the future we can replace the HeNe laser (2 mW) with a more powerful laser to study the higher mechanical modes of diamond resonators.

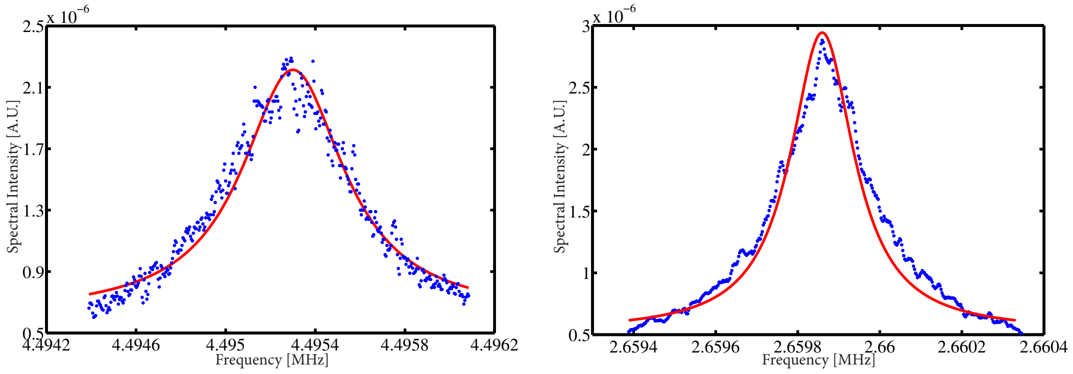

(a) (b)

FIGURE 5.12. First order transverse mechanical modes of (a) a (40μm x 2 μm x 1.3 μm) doubly clamped diamond oscillator with Q $\approx 11,000$, and (b)a (16μm x 1.53 μm x 0.7 μm) cantilever with Q $\approx 20,000$.

5.6. Mechanical Ring-down Measurement

Mechanical ring-down measurement is a two-step process. First, a mechanical oscillator is driven at its resonant frequency by a transducer. In general, a piezoelectric transducer is attached right next to the mechanical oscillator. Then, the transducer is turned off so that the mechanical oscillator vibrates freely. The amplitude of the vibration is exponentially decayed due the mechanical damping loss.

For temporal ring-down measurement, we can rewrite the damped harmonic oscillator equation shown in (5.7) as:

$$\ddot{x}(t) \; + \; \gamma\dot{x}(t) \; + \; \omega_0^2 x(t) \; = \; 0 \tag{5.18}$$

With the initial condition $x(t = 0) = x_0$ (steady state amplitude) and assumption as $\gamma << \omega_0$, the time-dependent decayed amplitude can be expressed as:

$$x(t) \; = \; x_0 \, e^{-\gamma t/2} \, cos(\omega_0 t + \phi_0) \tag{5.19}$$

Room temperature mechanical ring-down measurement of SiN oscillator with dimensions of (46μm x 3 μm x 150 nm) has been shown in Fig. 5.13. The mechanical quality factor of $Q \approx 16,000$ and the resonant frequency of 5.06 MHz are observed from a single data acquisition. Compared to the measurement of the resonant spectrum at frequency domain shown in Fig. 5.12. which requires multiple scans to average out the signal, ring-down measurement is at least 10x faster and less sensitive to the gradual drift of the position of the sample.

Similar measurement is done on a diamond cantilever with dimensions of (16μm x 1.53 μm x 0.7 μm) as shown in Fig. 5.14. The quality factor of $Q \approx 20,000$ and the resonant frequency of 2.6 MHz are observed. The signal is noisier than its counterpart of SiN oscillator due to the transparency of diamond.

5.7. Driven Oscillation Measurement

In this measurement, a mechanical oscillator is driven to its steady state and the spectral fluctuation of the driven amplitude is measured with a spectrum analyzer in frequency domain. The amplitude of the driven oscillation is rewritten from Eq. (5.8). as:

$$x_0^2 = \frac{f_{ext}^2}{m^2} \frac{1}{(\omega_0^2 - \omega^2)^2 + \gamma^2\omega^2} \tag{5.20}$$

In Fig. 5.15., both thermal and piezoelectric-transducer driven motion of a diamond cantilever is measured simultaneously. As expected, piezoelectric-transducer driven motion is significantly stronger than thermal driven motion. The quality factor and the resonant frequency of a resonator can be concluded from these scans. However, compared to ring-down measurement, each scan can only represent a single point and several scans are required to get the complete picture of the oscillator. The

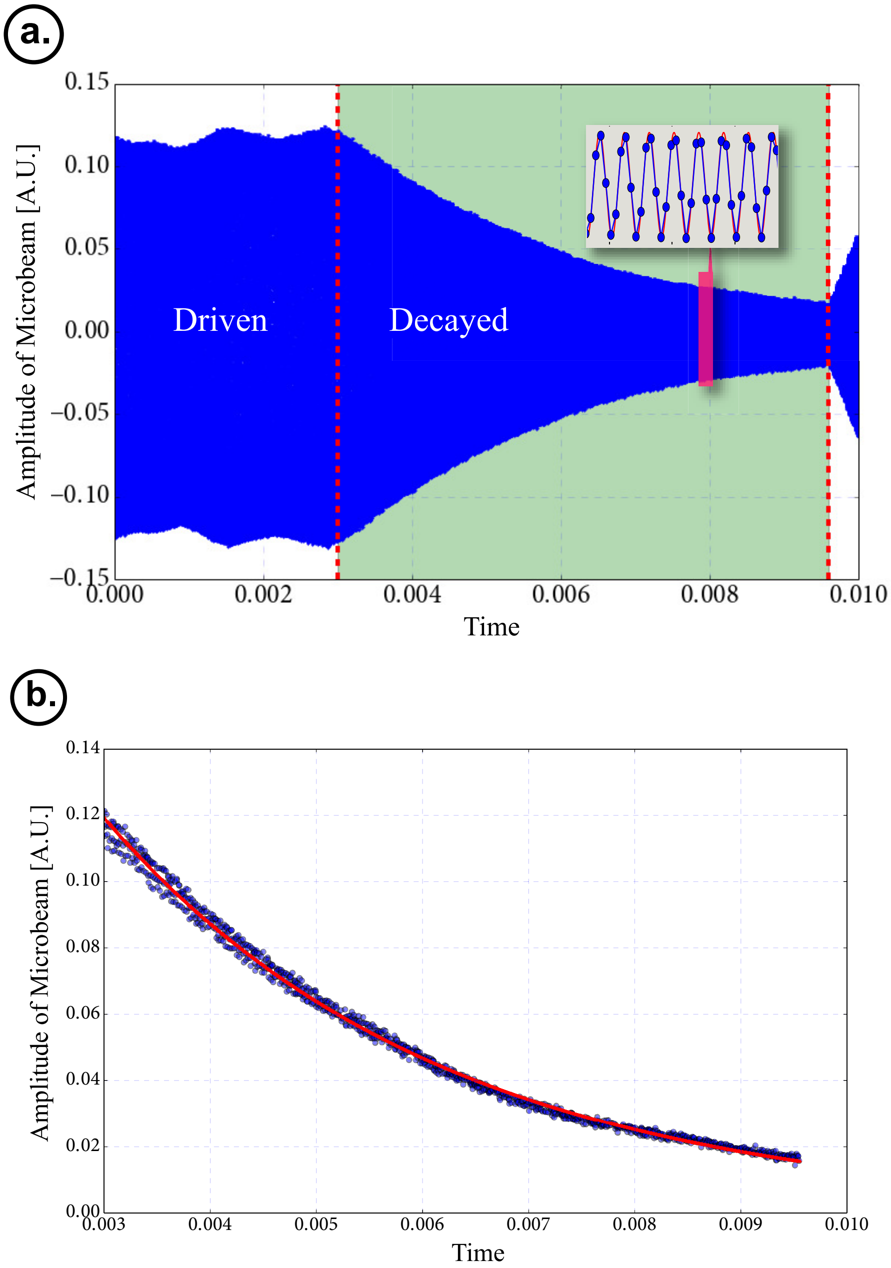

FIGURE 5.13. Mechanical ring-down measurement of a silicon nitride nanomechanical oscillator: (a) the SiN oscillator was driven from t=0 to t=3ms using a piezoelectric transducer and at t=3ms, the external driving force was turned off and the oscillator was allowed to oscillate freely. (b) the quality factor of SiN oscillator is extracted from the exponentially decayed amplitude.

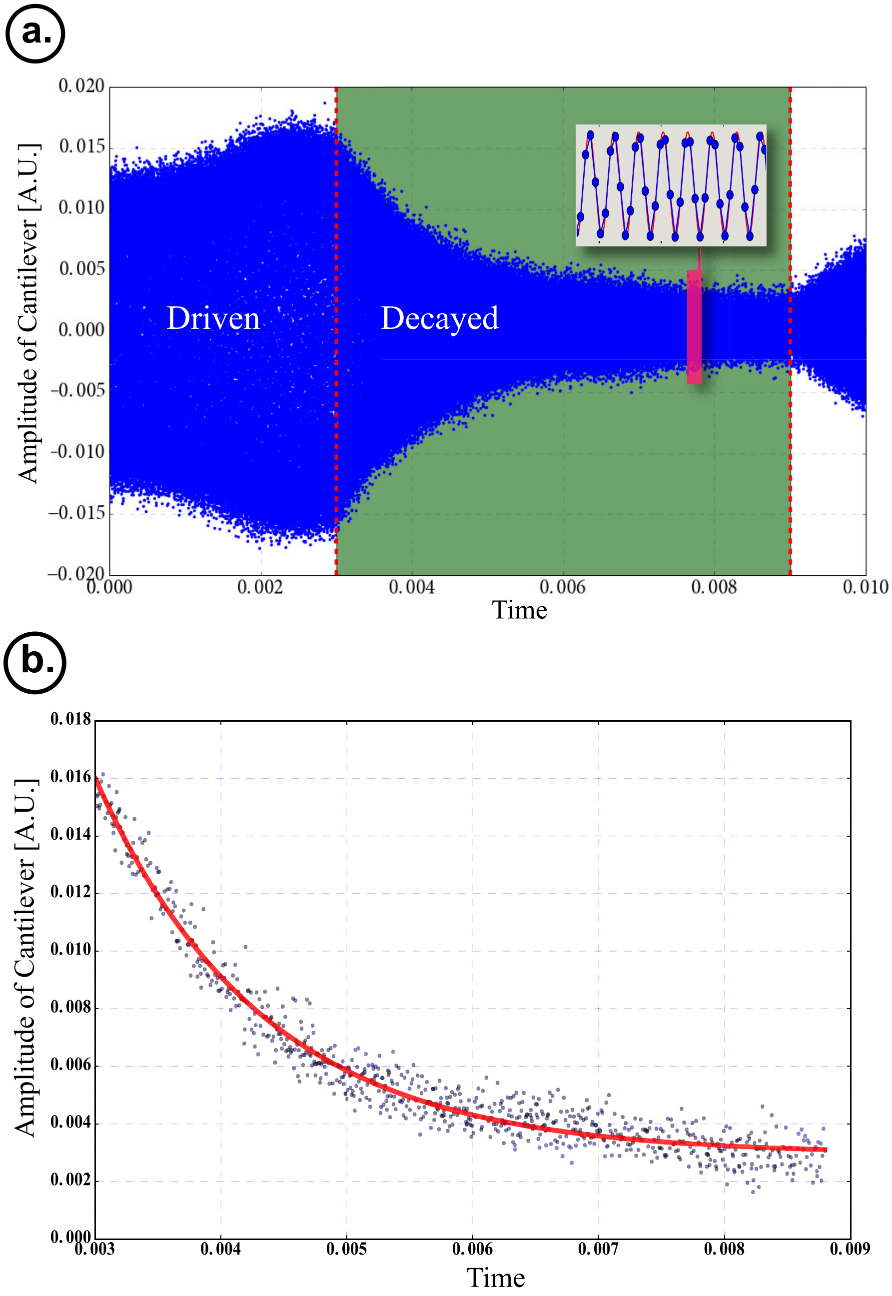

FIGURE 5.14. Mechanical ring-down measurement of a diamond cantilever: (a) the diamond oscillator was driven from t=0 to t=3ms using a piezoelectric transducer and at t=3ms, the external driving force was turned off and the oscillator was allowed to oscillate freely. (b) the quality factor of a diamond cantilever is extracted from the exponentially decayed amplitude.

same experiment with the same sample is done at cryogenic temperature (T= 7K) as shown in Fig. 5.16. Thermal driven motion is not being able to be detected in cryogenic temperature compared to its room temperature counterpart (Fig. 5.15.). Due to the lack of thermal damping at cryogenic temperature, the quality factor ($Q_{T=7K} = 55,000$) is 2.5 time higher than at room temperature measurement.

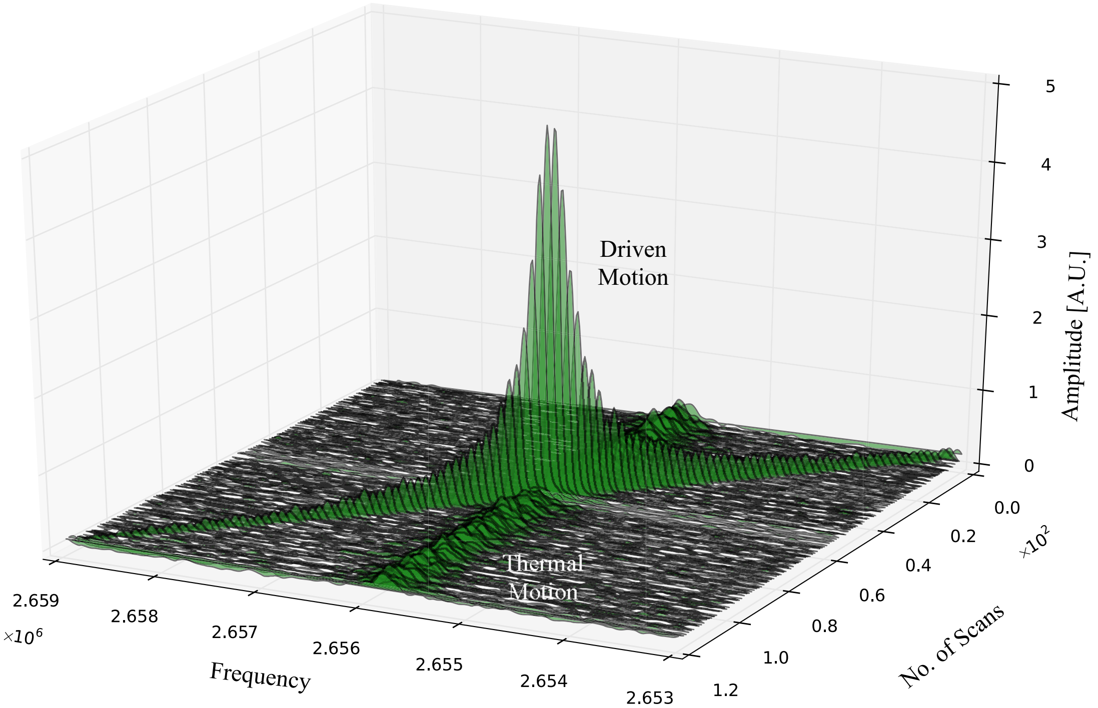

FIGURE 5.15. Spectrum of both thermal and piezoelectric-transducer driven motion of a diamond cantilever at room temperature.

In summary, I studied in theoretical terms the eigenfrequencies of the transverse mechanical modes of SiN and diamond resonators via the Euler-Bernoulli beam theory and I also experimentally proved how theoretical models is as valid as possible. Both the time and frequency domain measurement of nano-mechanical resonators at room and cryogenic temperatures have been demonstrated experimentally. Moreover, both thermal motion and mechanically driven motion have been characterized thoroughly.

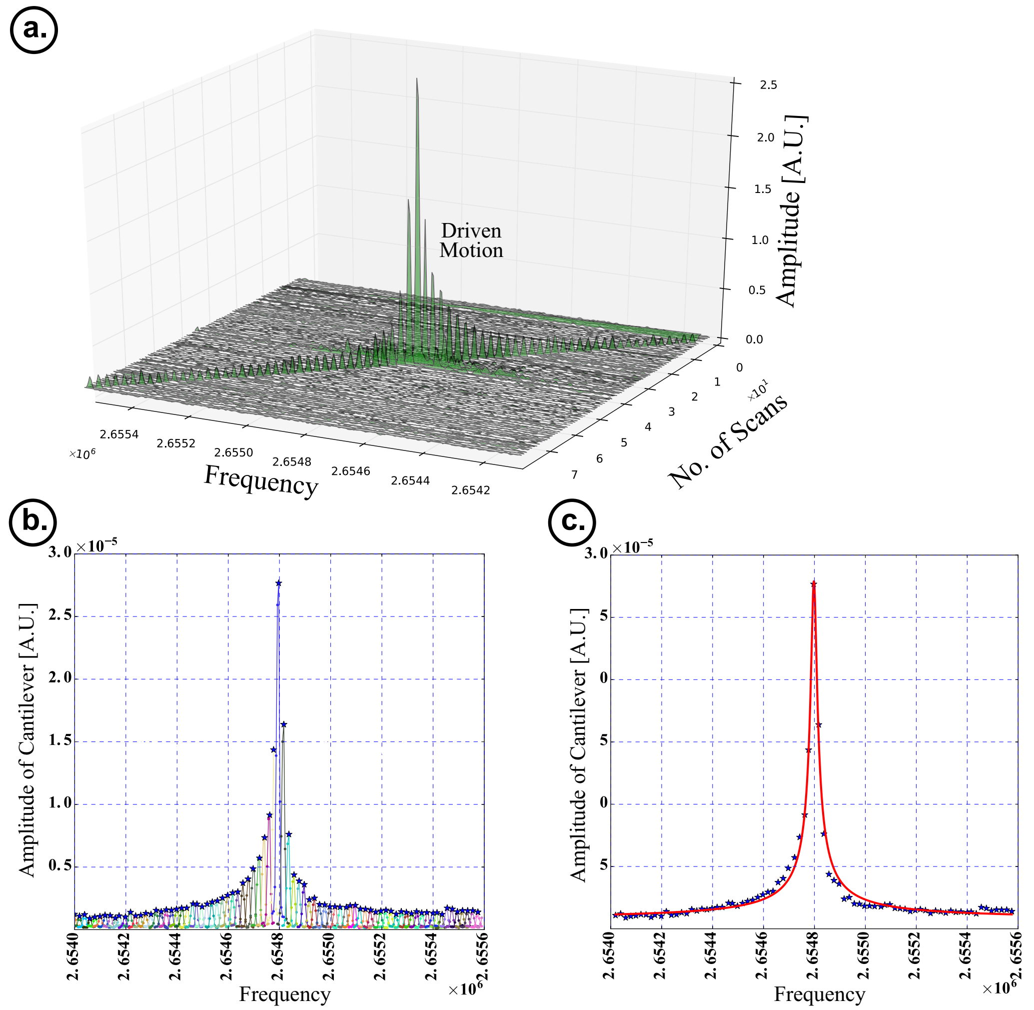

FIGURE 5.16. (a,b) Spectrum of piezoelectric-transducer driven motion of a diamond cantilever at cryogenic temperature. (c) Its amplitude is fitted as the square root of a lorentzian shown in Eq. (5.20).

I also approximated the measurement sensitivity of my mechanical system and conducted the experimental measurement successfully.

CHAPTER VI

SURFACE ACOUSTIC WAVE & NV CENTERS

This chapter was previously published in Physical Review Letters[78]. My primary contribution is the fabrication and characterization of the SAW device. I am also responsible for building the real time photon counting device using a field-programmable gate array (FPGA). I also worked closely with Andrew Golter for the optical measurement. Kevin Steward also helped us with the RF sputtering deposition of zinc oxide on the diamond surface. Mayra Amezcua contributed to the theoretical analysis of the experiment. My advisor, Hailin Wang, supervised the project.

6.1. Introduction

A scalable long distance quantum communication[79–81] is one of the greatest challenges in quantum information processing (QIP). In light of recent significant progress in hybrid quantum system[82–84] with nano-mechanical resonators and further development in nano-mechanical device fabrication, optomechanical devices are one of the promising candidates for sloving the issue. Due to intense study and technological improvement, these optomechanical systems can be very scalable on chips; and in terms of quantum communication and processing, phonons have a great advantage as a quantum memory transducer due to their long-lived coherent time compared to photons. Moreover, these mechanical systems have been proven to be able to interact with a wide variety of electric, magnetic and optical quantum systems.

There are several optomechanical system with different types of mechanical oscillators such as photonic crystal[85], cantilevers[86, 87] and acoustic wave resonators[88–93].

Recently, surface acoustic wave (SAW) devices have been proposed as a universal, on-chip quantum transducer[90] and can serve as a universal quantum platform linking a broad array of qubits such as superconducting qubits[94], quantum dots[95], trapped ions and nitrogen vacancy centers[96, 97] in diamond and silicon carbide[98]. A great benefit of using SAW devices is that their technology is well-developed and approximately 3 billions devices annually have been used in many applications, especially in the telecommunication sector. With the help of SAW devices, researchers have recently achieved interactions between the propagating phonons and the superconducting qubit with the help of SAW devices while there is also significant progresses in spin-phonon interaction in nitrogen vacancy center in diamond with high-overtone bulk acoustic resonators (HBARs) and high-quality-factor (high-Q) mechanical cantilevers. SAW resonators with high-quality-factor have been shown to be a reasonable candidate for integration into quantum coherent devices.

6.2. Surface Acoustic Wave

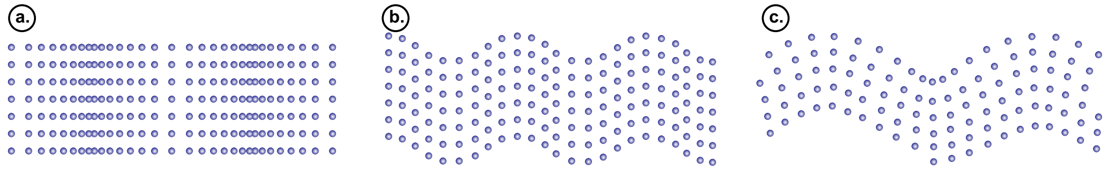

FIGURE 6.1. (a) Compression Wave (b) Shear Wave (c) Surface Acoustic Wave

In acoustic wave motion, there are generally two types of motion: compression and shear. The motion of the medium is aligned with the direction of the wave propagation in the compression wave while the motion is parallel in shear wave. Surface acoustic wave (SAW) is a combination of both the compression wave and shear wave. Most of SAW energy is confined within one wavelength into the medium and the amplitude of SAW falls off exponentially with its depth from the surface.SAW penetration depth is inversely proportionally to its frequency. Surface acoustic wave possesses a wide range of frequency starting from 10 MHz to 4 GHz.

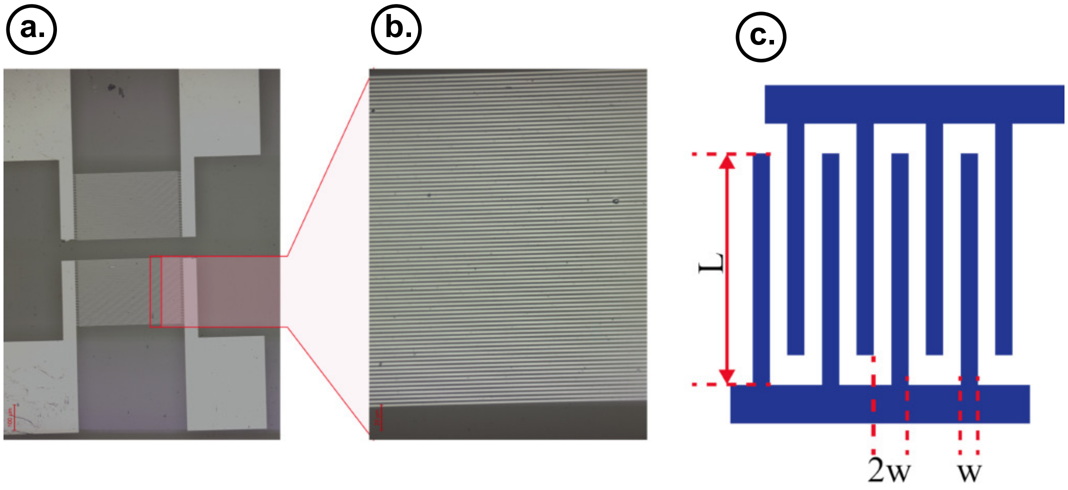

FIGURE 6.2. (a) Thermally deposited 100nm thick aluminum electrodes as interdigital transducer. (b)Zoom-in subset of interdigital transducer. (c) Simplified layout of IDT electrodes.

Interdigital transducers[99] (IDTs) are the most widely used transducers for generating surface acoustic waves. They can convert electrical energy into mechanical energy and vice versa with the help of piezoelectric material. IDTs are made of thin metal electrodes deposited on piezoelectric substrate. When the potential is applied across the IDT electrodes, it causes the periodic surface displacement. For the piezoelectric materials such as aluminum nitride (AlN), Lithium niobate ($LiNbO_3$) and zinc oxide (ZnO), the IDT electrodes can be fabricated without any intermediate step to become a transducer. For our case, diamond is not a piezoelectric material and we do need a intermediate piezoelectric layer to induce the surface acoustic wave and then transfer to the bulk diamond. The resonant frequency of the IDT is defined as

$$f = \frac{v_s}{4\text{w}} \tag{6.1}$$

where v_s is the SAW velocity and depends on the thickness of the piezoelectric material and type of the material we eventually want to generate SAW waves. 'w' is the width of each individual electrode, as shown in Fig. 6.2c.

6.3. Fabrication of Interdigital Transducers on Diamond

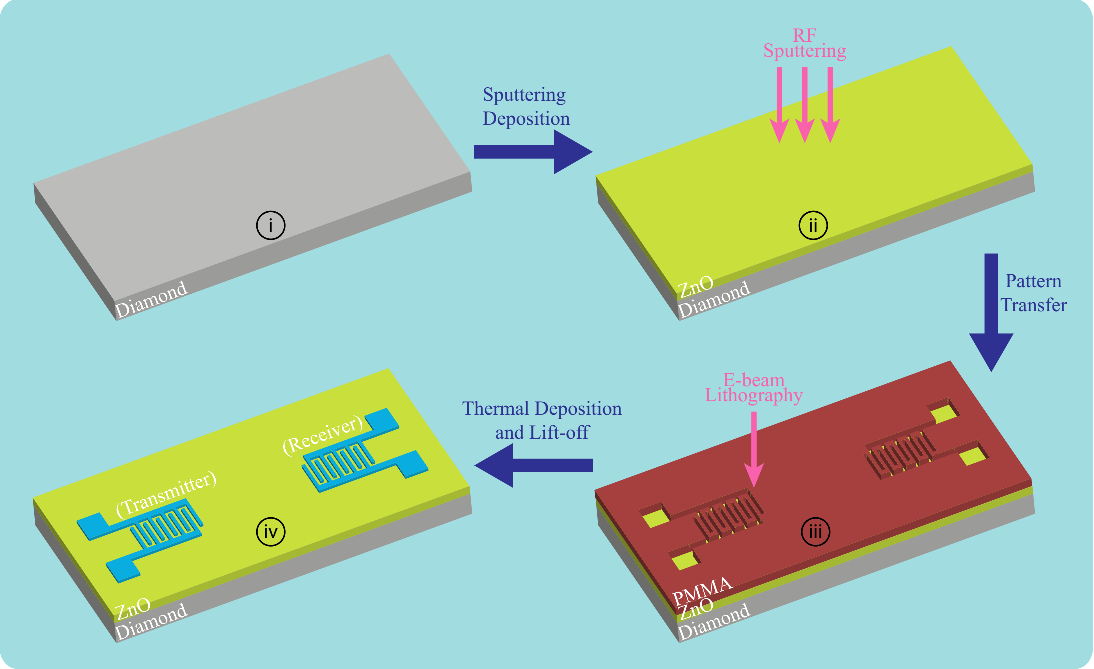

FIGURE 6.3. Fabrication steps for IDT on Diamond: (i) a bulk diamond sample (5mm x 5mm x 500μm) with NV centers from E6, (ii) RF-sputtering deposition of ZnO, (iii) E-beam lithography with PMMA resist (iv) thermal deposition of aluminum followed by lift-off process with acetone.

First the diamond sample (5mm x 5mm x 500μm) with NV centers from Element Six is cleaned with a 1:1:1 mixture of sulfuric, nitric, and perchloric acid at 380 for

2 hours. In order to convert an electrical signal to a mechanical acoustic wave, zinc oxide (ZnO) is used as piezoelectric material. Approximately 400nm ZnO film is deposited on the surface of diamond by using a radio frequency sputtering deposition system with the sputtering gas of 80% Argon and 20% Oxygen at RF power of 50W. Two Interdigital transducer (IDT) patterns are transferred via E-beam lithography and subsequently depositing 100nm of Aluminum thin film followed by the lift-off process with acetone.

We set the width ‘w’ of the individual IDT fingers to 1.5 μm. The resonant frequency is calculated by means of the relationship shown in Eq. (7.1). For our sample, v_s is approximately 5600 m/s giving us a resonant frequency of roughly 900MHz. Forty pairs of IDT fingers with the length L = 400 μm are made for each IDT and two IDTs (one to be served as a transmitter and another as a receiver) are fabricated 80 μm apart. (See Fig. 6.2c)

6.3.1. E-beam Lithography on Diamond

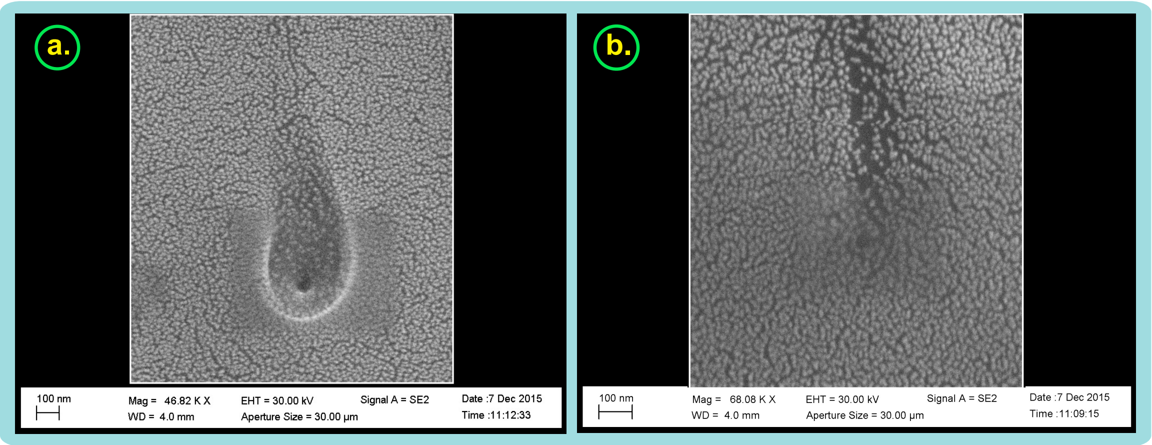

FIGURE 6.4. SEM image of E-beam alignment spot burned on PMMA with the anti-charging gold layer. Due to the different amount of time spent on individual spots and the variation in thickness of the anti-charging gold layer, some spots are obvious and others are obscure.

Since E-beam lithography uses a focused electron beam to shoot to the surface covered with an electron-sensitive film called E-beam resist, these electrons can easily build up a negative charge on the substrate if they cannot quickly neutralize with the ground. When the sample gets a charge, the electron beams will be deflected and the E-beam pattern will be obscure and distorted. One way to solve the issue is to clamp a substrate with a metal clamp so that the excessive charges can flow to the ground. The major drawback with this approach is the pattern has to be written close to the metal clamp. Another approach, which we use in this fabrication process, is to deposit an anti-charging layer with gold or titanium. After ZnO deposition on diamond, we spin-coat 400-500nm of polymethyl methacrylate (PMMA) as an E-beam resist, followed by a thermal deposition of 4-6nm of gold as an anti-charging layer.

Nanometer Pattern Generation System (NPGS) software is used to write the E-beam pattern. It is important to mention that it is necessary to perform X-Y-Focus Mode because the IDT pattern is a relative large pattern and we need to know in quantitative terms how much the sample is tilted. X-Y-Focus Mode determines the height (z-height) between the microscope objective and the substrate and generate the relation between X-Y coordinate (assuming the sample is completely flat and along the X-Y plane.) and the height. Therefore, to acquire the coordinate data, we first create a feature on the E-beam resist by burning a tiny hole so that we can adjust the exact z-height on that point. To calculate a plane, three points is a minimum requirement but we usually get 5-6 points to get a better calculation with the root-mean-square-error within the range of 10^{-6} mm.

For E-beam lithography with a 400-500nm thick PMMA resist, the following parameters are used in the Zeiss E-beam lithography instrument: 30μ aperture, 30kV energy, 377 pA beam current, 21.28 nm center-to-center distance, 42.56 nm line spacing, and 750-800 μC/cm^2 area dose. If the thickness of the anti-charging gold layer is changed, the area dose has to be changed; otherwise the E-beam pattern will be overexposed or underexposed.

6.4. Electron-phonon Interaction

One of the most successful exploitation of mechanical vibration for quantum information processing (QIP) involves the combination of both optical and mechanical interactions through phonon-assisted optical transition or sideband transitions. These interactions occur in the resolved-sideband regime, where the mechanical frequency, ω_m, exceeds the decoherence rate for the relevant optical transitions. The resolved sideband emission of a quantum dot coupling to a SAW has been demonstrated[95].

In our experiment, we reported the experimental realization of optomechanical control of the NV center in diamond through the sideband transitions[100]. Quantum interference between the sideband transition and the direct optical dipole transition has been observed. We also realized Rabi oscillation of the NV center driven simultaneously by both optical and surface acoustic fields. These studies represent a major step toward achieving the quantum control of both the internal atom-like states and the mechanical motion of a hybrid artificial-atom nano-mechanical system.

A NV center has to be located less than a few microns below the surface of the diamond so that both mechanical (acoustic) and optical fields have profound effects on it. The excited state optical transition ($|m_s = 0\rangle$ to $|E_y\rangle$) near $\lambda = 637$ nm is used in the experiment. The optical excitation spectrum of the transition without an acoustic field for a single NV center is shown in Fig. 6.5c with respect to the detuning of the laser frequency.

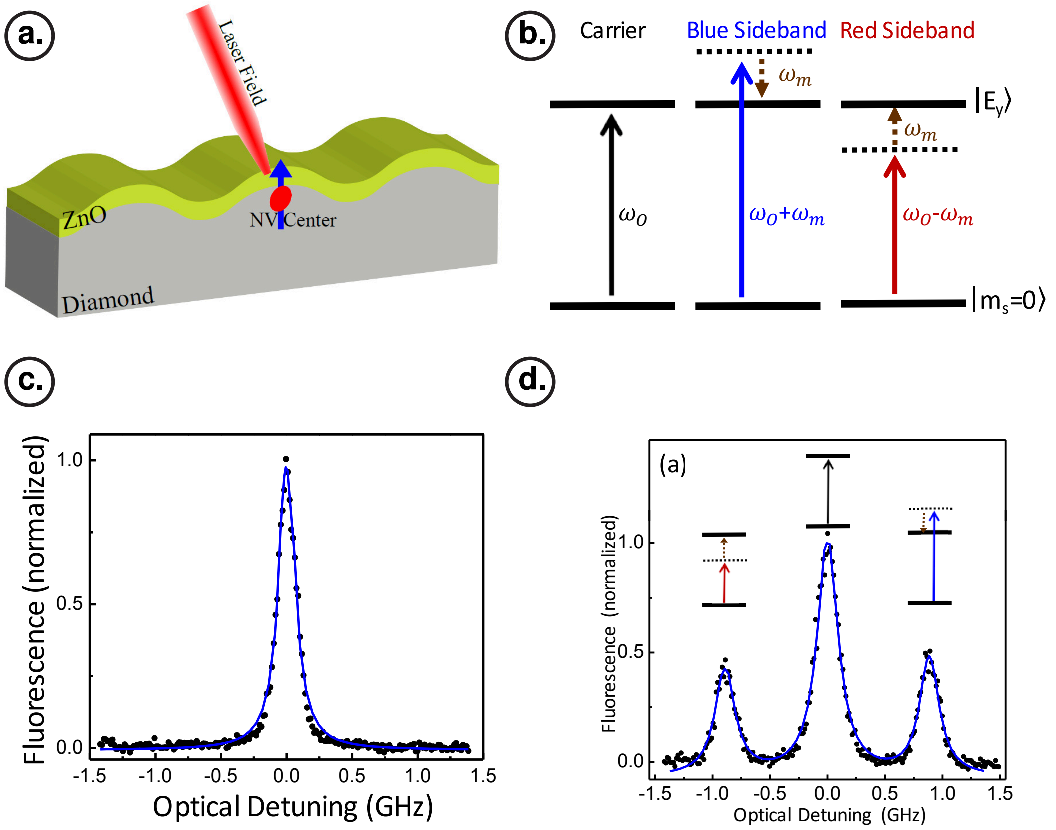

FIGURE 6.5. (a) A NV center located a few microns below the surface of diamond can be coupled to both optical and acoustic fields. A 300nm-500nm thick ZnO layer is deposited as a piezoelectric mediator to induced the surface acoustic waves on diamond. (b) Energy level diagram representing the blue and red sideband transitions for the optomechanical interactions. The carrier optical transition is between the $m_s = 0$ ground state and E_y excited state of the NV center. (c) The excitation spectrum of the carrier transition while the acoustic field is turned off. (d) The excitation spectrum of the NV center simultaneously driven by both the optical and acoustic fields. The acoustic field is driven at $\omega_m = 900MHz$. The power of the incident laser fields is about $P_0 = 0.4\mu W$ and the RF input power of the IDT is $P_{RF} = 0.2W$. In (c), and (d), flourescence is measured with respect to the detuning frequency of the optical dipole transition. The data are fitted with the Lorentzian function as a blue solid line.

The excitation of long-wavelength acoustic phonons in diamond induces a periodic lattice strain. The orbital degrees of freedom of the excited states of a NV couple strongly to this lattice strain[86, 101–103], with a deformation potential, D, of several eV. The electron-phonon coupling can be characterized by a strain-induced energy shift as well as state mixing of the relevant electronic energy levels. For phonon-assisted optical transitions, we consider the strain-induced energy shift of the NV excited state $|E_y\rangle$, with the electron-phonon interaction Hamiltonian given by:

$$H_{e-phonon} = \hbar \; g \; (\hat{b} + \hat{b}^{\dagger}) \; |E_y\rangle \langle E_y| \tag{6.2}$$

where $\hat{b}$ is the annihilation operator for the mechanical mode, $g = Dk_m\sqrt{\hbar/(2m\omega_m)}$ is the effective electron-phonon coupling rate, k_m is the wave number of the mechanical mode, and m is the effective mass of the mechancial oscillator. With the laser field at the red sideband of the optical dipole transition, the effective interaction Hamiltonian for the first red sideband transition is given by,

$$H_R = \frac{\hbar \; g \; \Omega_0}{2\omega_m}(\hat{b}\sigma_+ + \hat{b}^{\dagger}\sigma_-) \tag{6.3}$$

where Ω_0 is the Rabi frequency for the optical field and $\sigma_\pm$ are the raising and lowering operators for the two-level optical transition. The effective Rabi frequency for the sideband transition is thus given by $\Omega = g\sqrt{n}\Omega_0/\omega_m$, where n is the average phonon number. A similar Hamiltonian can also be derived for the first blue sideband transition. Note that electron-phonon interactions in diamond can also take place through the ground-state triplet of the NV center. The ground state spin-phonon coupling, however, is a few orders of magnitude weaker than the excited-state electron-phonon coupling due to the symmetry of the NV ground-state wave functions.

The phonon-assisted sideband transition is observed by detecting the fluorescence coming out of an NV center when it is simultaneously driven by both optical and mechanical fields. For the photo-luminescence excitation (PLE) spectrum shown in

Fig. 6.5c, the NV center is initially prepared to the $|m_s = 0\rangle$ state using the green laser ($\lambda = 532nm$) and the NV emission from the excited state ($|E_y\rangle$) is measured as a function of detuning of the incident laser field while the the mechanical frequency (ω_m) of the acoustic fields is fixed at 900 MHz. The blue and red sideband resonances observed in the PLE spectrum correspond to the Stokes and anti-Stokes phonon-assisted optical transitions, respectively, while the carrier resonance at zero detuning corresponds to the direct optical transition from the $|m_s = 0\rangle$ to $|E_y\rangle$ states. The spectral separation between the sideband and the carrier resonance equals ω_m, as confirmed by the dependence of the sideband spectral position on the RF driving frequency of the IDT shown in Fig. 6.5d.

To further verify these blue and red sideband transitions are due to the acoustic fields, we examined the splitting between the optical dipole transition and acoustic field assisted transition in terms of the driven frequency of the acoustic fields. As we expect, the splitting is determined by the driven frequency. (see Fig. 6.6a). At the relatively weak optical and acoustic power, the peak amplitude of the resonance increases linearly with both power (see Fig. 6.6c). As shown in Fig. 6.6b, the sideband resonances are more robust against power broadening compared to the carrier resonances. The spectral linewidths of both the carrier and sideband resonances are plotted in Fig. 6.6d.

In a relatively low optical power regime ($P_0 < 25\mu W$), the linewidths of the sideband resonances are still approximately 175 MHz while the linewidth of the carrier resonance ends up four time larger than it was before. The power broadening of the carrier resonance can be accounted for by a simple two-level model. The broadening also provides a way to measure the optical Rabi frequency Ω_0. From Fig. 6.6d, we estimate $\Omega_0/(2\pi\sqrt{P_0}) = 65$, where P_0 is the incident laser power. The lack of power broadening in sideband transitions indicates that the effective Rabi frequency Ω of NV center is still small compared to its optical dipole transition linewidth.

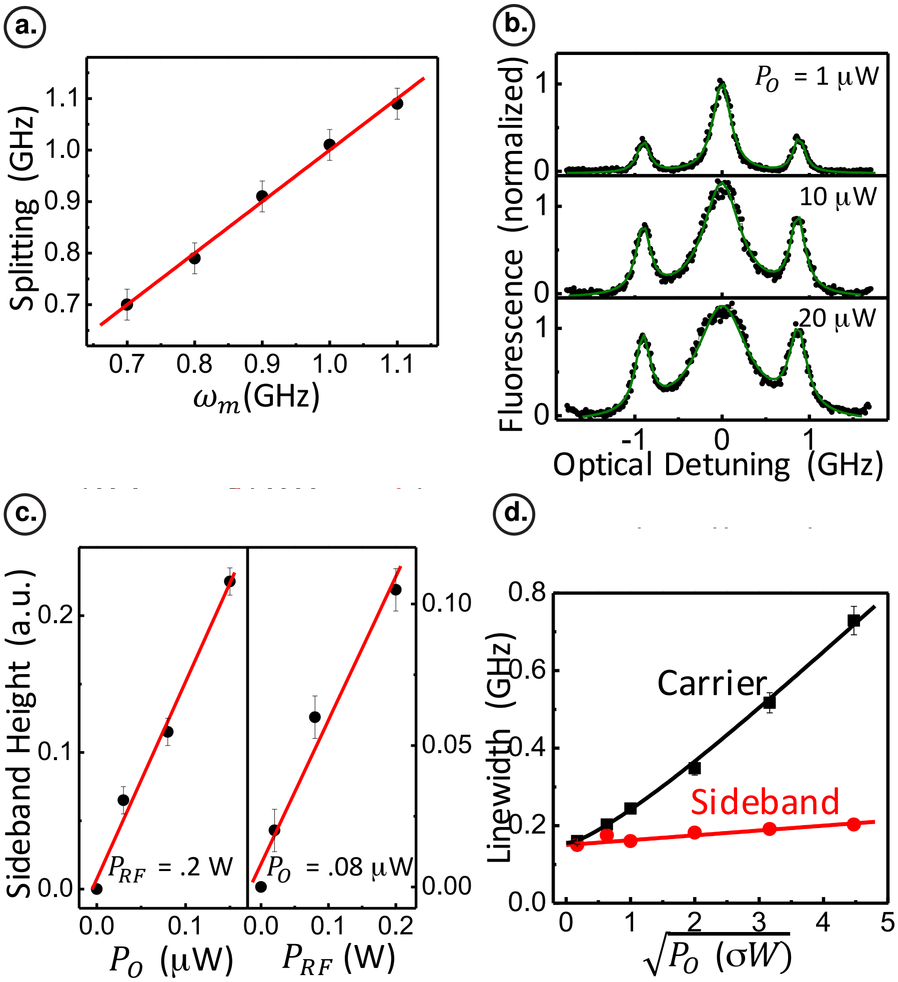

FIGURE 6.6. (a) Frequency measurement of the splitting between the carrier and sideband resonances as a function of the driven frequency ω_m. Red line is to guide the eye where the splitting is equivalent to the driven frequency ω_m. (b) Excitation spectra of the NV obtained for three different laser powers and with PRF = .1 W. Green lines are fits to Lorentzians. (c) Amplitudes of the sideband resonances with increasing optical P_0 and acoustic P_{RF} power. (d) Linewidths of the carrier resonance (black squares) and red sideband resonance (red circles) as a function of optical laser power P_0, with $P_{RF} = .1W$. The carrier resonance exhibits strong power broadening. Black line is the theoretically calculated power broadening. Red line is a liner fit to guide the eye.

Surface acoustic wave assisted transition and the direct optical dipole transition can interfere each other (see Fig. 6.7a). To demonstrate this interference, we drive these two transitions simultaneously with both optical and acoustic fields. We phase-lock both ω_1 and $\omega_2 + \omega_m$ optical fields. Moreover, the phase of the acoustic field ω_m is also locked to the optical fields. While all three fields are phase-locked, we scan the optical field of the sideband transition. A sharp resonance is retained when the resonant frequency of the carrier transition matches the sum of the frequency of the sideband detuned optical field and acoustic field (see Fig. 6.7b). The width of the resonance ($<$ 10 Hz) is limited by the instrument resolution. We can further verify this interference by varying the relative phase of the acoustic field and measuring the peak amplitude of the fluorescence coming out of the NV center. This sinusoidal oscillation demonstrates the interference between the carrier and sideband transition and proves that the optomechanical processes can be fully coherent with the conventional optical processes (see Fig. 6.7c).

In general, the optical dipole transition linewidth of a NV center in our experiment is approximately 200 MHz. And we are driving our acoustic fields at 900 MHz. Therefore, the acoustic field assisted sideband transition is well within the resolved sideband limit. In the resolved sideband limit, the Rabi oscillation of the two-level NV system can be driven by using the acoustic field assisted sideband transition. To demonstrate this, the NV center is initially prepared in the $m_s = 0$ ground state. The optical laser field is tuned into the red sideband. The red detuned laser field is treated as a continuous field. Then the acoustic pulse is sent out to mediate the sideband transition and simultaneously the fluorescence emission from the NV is measured in the time domain. Using three different acoustic field strengths, we measure the optomechanically driven Rabi oscillations in time domain with the

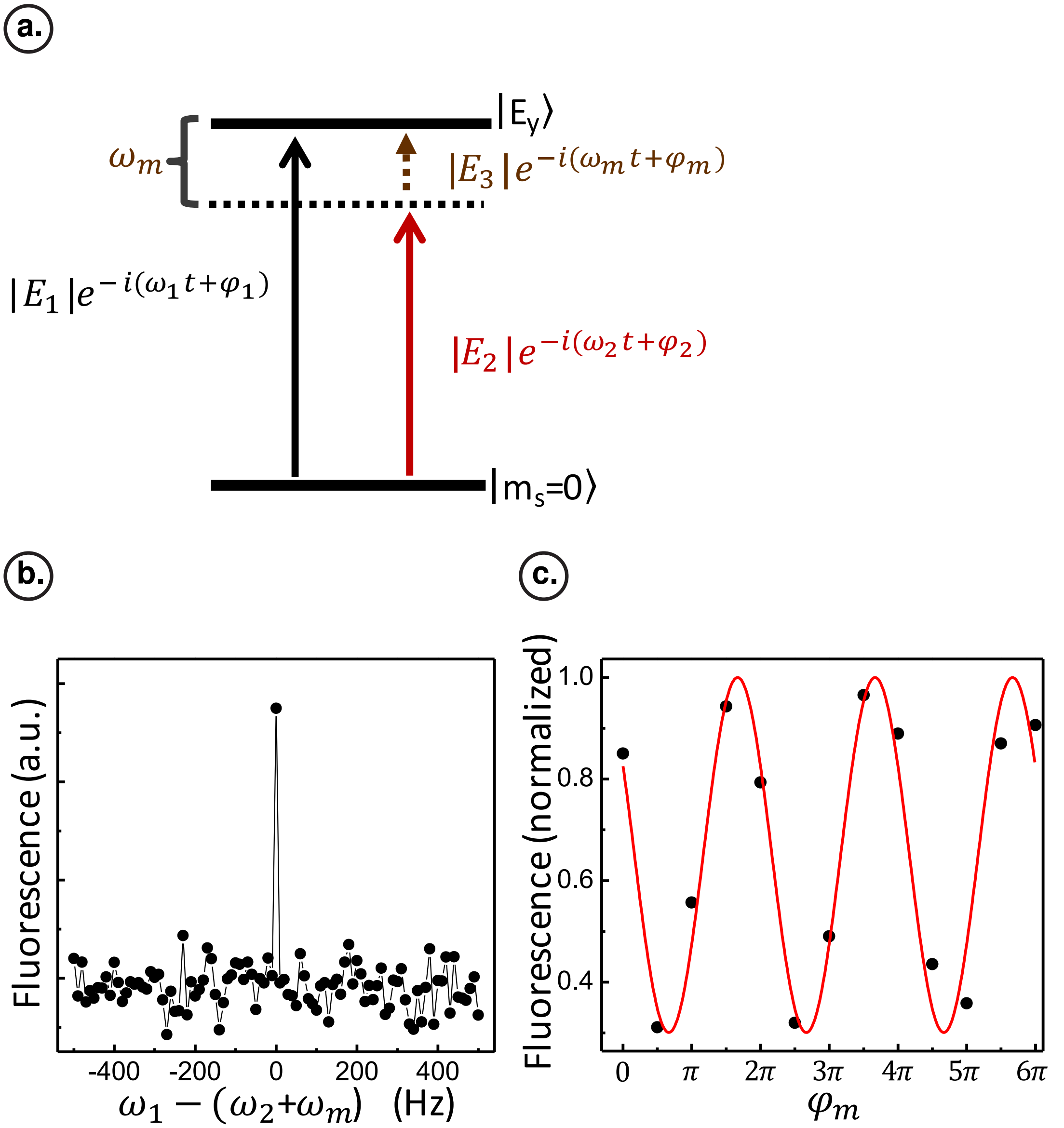

FIGURE 6.7. (a) Black arrow represents the direct optical dipole transition and, the red arrow and dotted arrow represents the acoustic field assisted sideband transition. (b) The fluorescence of a NV center as a function of detuning between the direct transition optical field and sideband transition optical field while the acoustic field is fixed at $\omega_m = 900MHz$. (c) The fluorescence of a NV as a function of the phase of acoustic field ϕ_m with $\omega_1 = \omega_2 + \omega_m$, demonstrating the sinusoidal interference oscillation between two transitions.

time resolution of approximately 3 ns. From this measurement, the estimated Rabi frequency of $\Omega_0/2\pi = 290$ MHz is extracted. The effective Rabi frequency Ω for the sideband transition can be derived from the Rabi oscillations and it complies with the square root of the RF driving power of the acoustic field (see Fig. 6.8)

The amplitude of the surface acoustic wave (SAW) can be estimated based on these experiments.

$$A_{saw} = 2(\omega_m/k_m)(\Omega/\Omega_0)/D \tag{6.4}$$

where A_{saw} is the amplitude of SAW, ω_m is the driving frequency of SAW, Ω is the effective Rabi frequency, $_0$ is the Rabi frequency and D is the deformation potential. With $\Omega_0/2\pi = 290MHz, \Omega/2\pi = 66MHz, \omega_m/k_m = 5600m/s, andD/2\pi = 610THz$, A_{saw} is approximately 0.7 pm. This relatively small amplitude of the SAW required to drive the Rabi oscillation also reflects the strong electron-phonon coupling between acoustic phonons and the NV center.

The resolved sideband optomechanical processes realized in these experiment can be applied to quantum information and processing in high-Q hybrid optomechanical system such as NV centers embedded in diamond nanomechancial oscillators. For a diamond nanomechancial oscillator with a mechanical resonant frequency $\omega_m = 900MHz$ and effective mass $m_{eff} = 1pg$, the excited state electron-phonon coupling can be as strong as 2 MHz.

In summary, we have demonstrated the quantum control of the internal states of an NV center by using optomechanical sideband transitions and by taking advantage of the strong excited state electron-phonon coupling of NV centers. The combination of the long coherent time of the NV center and exceptional material properties of diamond suggest a promising future for this hybrid system in quantum information and processing. In addition, the readily available SAW technologies in the industrial world could give this system a head start in the pursuit of quantum communication. In this chapter, we have demonstrated how to integrate the excited state electron-phonon coupling into a simple two level system. In the next chapter, we will provide how to implement this electron-phonon coupling into a Λ-like three level system.

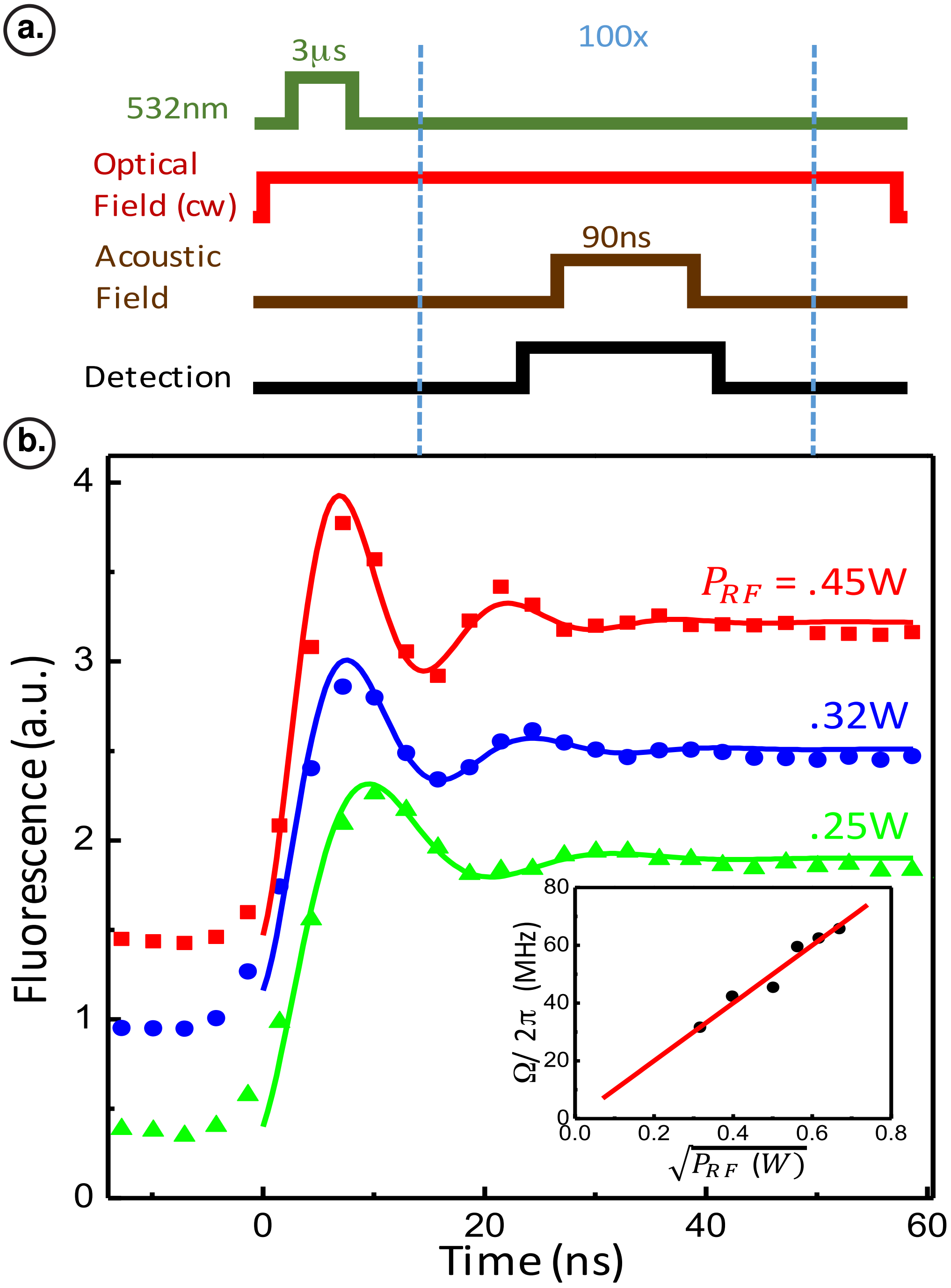

FIGURE 6.8. (a) Pulse sequence used for the Rabi oscillation experiment. Green laser is to initialized the NV center to $m_s = 0$ ground state. Red laser is tuned to the red side of the optical dipole transition and treated as a continuous field right after the initialization of green laser. (b) NV fluorescence as a function of time.Rabi oscillations are driven by three different acoustic field strengths. Inset: Rabi frequencies obtained as a function of RF power.

CHAPTER VII

SURFACE ACOUSTIC WAVE AND DARK STATE

This chapter was published in Physical Review X[104]. My main contribution is the fabrication and characterization of the SAW device, and worked together with both Andrew Golter and Ignas Lekavicius for the optical measurement. Kevin Steward also helped us with the RF sputtering deposition of zinc oxide on the diamond surface. Mayra Amezcua contributed to the theoretical analysis of the experiment. My advisor, Hailin Wang, supervised the project.

7.1. Introduction

In the previous chapter, we demonstrated how a surface acoustic wave (SAW) can be manipulated to couple an electron spin inside a diamond by taking advantage of the two level systems of the ground spin states of NV center in diamond[105]. In this chapter, we are going to pursue how to couple between a surface acoustic wave and an electron spin viaΛ-type three-level system in which two ground spin states couple to a common excited state through a phonon-assisted and a direct dipole optical transition.

In general, the decay of the ground state of the NV center is much longer than the decay of its excited state. We can take advantages this by using an optically prepared dark state, which can be established through quantum interference or through adiabatic evolution of the spin states. In this way, the ground spin states are sensitive to the excited-state strain coupling through optical interactions but are nearly immune to the decay of the excited state. The deformation potential, which defines the strength of the excited state strain coupling, scales with the relevant energy gap and the deformation energy of the excited state is five orders of magnitude stronger than its counterpart of the ground state of the NV center[106, 107].

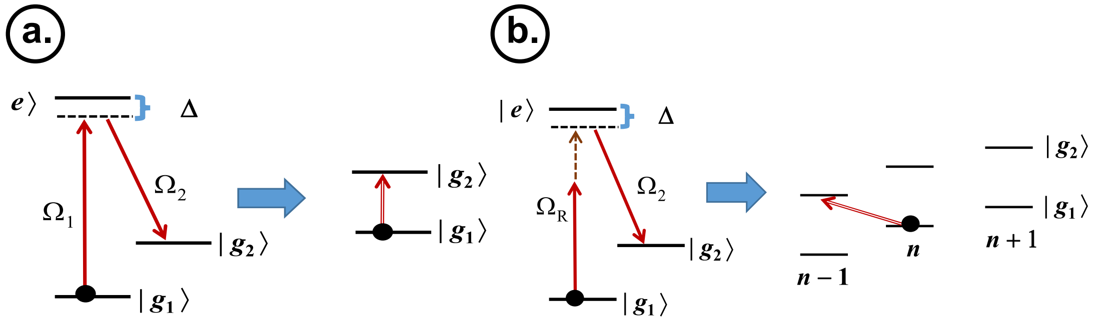

FIGURE 7.1. (a) Schematic of a Λ-type three-level system driven by two optical fields with respective Rabi frequency,Ω_1 and Ω_2. In the limit of large dipole detuning, Δ, the system becomes equivalent to an optically driven transition between the two lower states. (b) Schematic of a Λ-type three-level system driven by an acoustic field (brown dashed line) as well as two optical fields. The $|g_1\rangle$ to $|e\rangle$ transition is a phonon-assisted transition with effective Rabi frequency Ω_R. In the limit of large Δ, the system becomes equivalent to an optically driven transition between the phonon ladders of the two lower states, where n denotes the phonon number.

The Λ-type three-level system can be realized by using two ground states and one excited state of the NV center in diamond[108, 109]. The spin scan be transferred from one ground state to another through a SAW assisted dark state, in which the electron is trapped in a special coherent superposition of the two ground spin states and is thus decoupled from the excited state. Moreover, in the regime in which the external optical fields are sufficiently detuned from the respective dipole optical transitions, the excited state in the Λ-type three-level system can be adiabatically eliminated from the dynamics of the two spin states. In this case, the optically driven transitions take place between the phonon ladders of the two spin states (which we refer to as sideband spin transitions), as illustrated in Fig. 7.1. We have demonstrated the coherent coupling between a SAW and an electron spin in diamond via a dark state by observing phonon-assisted coherent population trapping (CPT).

7.2. Experimental Setup

The sample preparation and the generation of the surface acoustic waves (SAW) are identical to those described in the previous chapter. As mentioned, the ground state of NV centers is a spin triplet state composed of $m_s = \pm 1$ states and $m_s = 0$ state while the excited states are denoted by $A_{1,2}$, $E_{x,y}$ and $E_{1,2}$ with respect to their symmetry properties. For this experiment, the Λ-type three-level system is built by $m_s = +1$, $m_s = 0$, and A_2 state. A_1 and$E_{1,2E}$ state can also be served as the upper state of a Λ-type system instead of A2. However, we avoided using these states due to various mechanisms of state mixing[110, 111]. A practical advantage of using $m_s = 0$ as one of the lower state is that the initial spin preparation and detection can be done without the use of microwave fields. This also excludes the extra fabrication step required to design and implement a microwave antenna close to the NV center.

Different NV centers have their own unique splitting of energy level structure for many reasons such as their orientation, strain and so on[111]. For instance, for the implanted NV centers, during the implantation process, we tried to alleviate the mechanical strain. Therefore, the splitting between E_x and E_y is relatively narrower than its counterpart of non-implanted NV centers. First, we conduct a photoluminescence excitation experiment to identify each excited state optical transition so that we can single out the individual states to construct the desired Λ-type three-level system. For this photo-luminescence excitation experiment, the green laser ($\lambda = 532nm$) is used to initialize the spin state. While the green laser is used as *a*

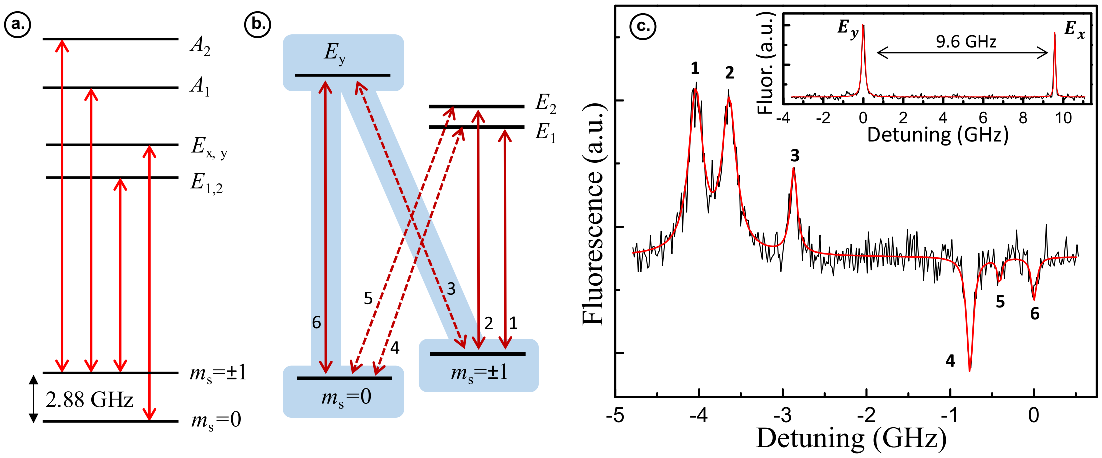

FIGURE 7.2. (a) Energy-level structure and dipole optical transitions of a NV center (strain free). (b) State mixing due to built-in dc strain, leading to additional dipole transitions, as indicated by the dashed lines. Shaded levels and arrows highlight the Λ-type three-level systems used in our experiments. (c) Excitation spectrum with a pump field fixed at the E_x transition. Peak labels indicate the corresponding transitions in (b). Red lines are fits to Lorentzians. Inset: Excitation spectrum obtained with no pump field.

pump laser , the red laser near the zero phonon line ($\lambda = 637nm$) is used as*a probe laser*. The pump and probe lasers are alternated periodically with a period of 10 μs.

When we scanned the probe laser around the wavelength ($\lambda = 637nm$), there are photo-luminescence resonant excitations between the ground state $m_s = 0$ and the excited states (E_x and E_y) as shown in the inset of Fig. 7.2 (c). For the particular NV center, there is a relatively broad energy splitting (9.6 GHz) between E_x and E_y which confirms a comparably large native dc strain. This leads to transitions between the E_y and the $m_s = \pm1$ state as well as transitions between the $E_{1,2}$ and the $m_s = 0$ state. We have to bring in the second *laser pump* to identify these transitions due to strain-induced state mixing. This pump laser is fixed at the resonant frequency of the transition between $m_s = 0$ and E_x state. As show in Fig. 7.2 (c), the excitation spectrum is obtained by scanning the red probe laser while the second pump laser is fixed at E_x transition and the x-axis is the detuning of the probe laser with respect to the second pump laser.

The high fluorescence background level in the excitation spectrum shown in Fig. 7.2 (c) is due the second *pump laser* driven E_x excitation. This resonant excitation also pumps the electron to $m_s = \pm 1$ state because there is a small probability for the electron to decay back to $m_s = \pm 1$ state instead of $m_s = 0$ state.

As shown in Fig. 7.2 (c), there are three positive peaks, which are labeled as '1', '2', and '3', representing the transitions between $m_s = \pm 1$ ground state to $E_{1,2}$ and E_y excited state. In these three cases, the electron is pumped back into the $m_s = 0$ ground state and therefore, the total amount of fluorescence of the transition between E_x and $m_s = 0$ is increased. In contrast, the excitation spectrum of the transition from $m_s = 0$ to $E_{1,2}$ and E_y state emerges as three negative peaks labeled by '4', '5', and '6'. These transitions effectively reduce the fluorescence from the pump-drive E_x transition. This pump-probe excitation spectrum provides detailed information on the optical transitions of the NV center without the need for a microwave field.

7.3. Phonon-assisted Coherent Population Trapping

As mentioned, the electron-phonon interaction Hamiltonian can be written as

$$H_{e-phonon} = \hbar\ g\ (\hat{b} + \hat{b^{\dagger}})\ |E_y\rangle\ \langle E_y| \tag{7.1}$$

where $g = Dk_m\sqrt{\hbar/(2m\omega_m)}$ is the effective electron-phonon coupling rate, $\hat{b}$ is the annihilation operator for the mechanical mode, k_m is the wave number of the mechanical mode, ω_m is the mechanical frequency and m is the effective mass of the mechanical oscillator. For the phonon-assisted optical transition from the $m_s = 0$ to the E_y state and with a laser field at the red sideband of the optical transition, the effective interaction Hamiltonian linear to the mechanical displacement can be derived as

$$H_R = \frac{\hbar\, g\, \Omega_0}{2\omega_m}(\hat{b}\ |E_y\rangle\, \langle m_s = 0|\ +\ \hat{b}^{+}\, |m_s = 0\rangle\, \langle E_y|) \tag{7.2}$$

where Ω_0 is the Rabi frequency for the laser field coupling to the transition between the $m_s = 0$ and the E_y state (i.e., the E_y transition). The effective Rabi frequency for the sideband transition is thus given by $\Omega = g\sqrt{n}\Omega_0/\omega_m$, where n is the average phonon number.

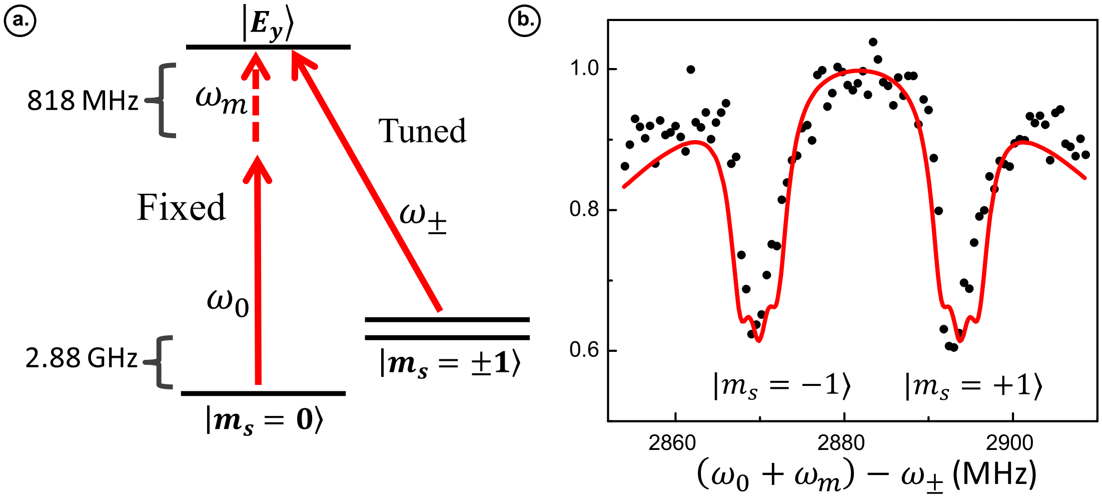

FIGURE 7.3. (a) Energy-level diagram used for phonon-assisted CPT. The solid red arrows are the optical fields. The dashed brown arrow is the acoustic field. (b) Fluorescence from state E_y as a function of $\omega_0 + \omega_m - \omega_\pm$. The optical power at frequency ω_0 and $\omega_\pm$ is 4 μW and 1 μW, respectively. The RF input power for the IDT is about 0.13 W. The two negative peaks correspond to Λ-type systems formed with either the $m_s = +1$ or the $m_s = -1$ state. The solid red curve is the theoretical calculation discussed in the text. The fluorescence is normalized to the peak of the theoretical excitation spectrum with no CPT.

Similar to what we did for the phonon-assisted Rabi oscillation demonstrated in the previous chapter, we can integrate a phonon-assisted optical transition into a Λ-type three-level system as shown in Fig. 7.3 (a). In general, a dark state can be generated in a Λ-type three-level system by simultaneously driving two optical transitions. A dark state is a special coherent superposition of the two lower states that is decoupled from the upper state. In NV center, it is also known as a metastable singlet state. Due to the nature of the destructive quantum interference between the optical fields and phonon-assisted optical field, the originated fluorescence level is quenched as shown in Fig. 7.3 (b). In this case, the direct optical dipole transition takes place between E_y and $m_s = \pm 1$ state while the phonon-assisted transition occurs between E_y and $m_s = 0$ state. The dark state for this Λ-type three-level system can be written as:

$$|\psi_d\rangle = \frac{1}{\sqrt{\Omega_R^2 + \Omega_\pm^2}} \left(\Omega_R \left| m_s = \pm 1 \right\rangle - \Omega_\pm \left| m_s = 0 \right\rangle \right) \tag{7.3}$$

where $\Omega_\pm$ is the Rabi frequency for the direct dipole optical transition between E_y and $m_s = \pm 1$ state. The electrons are trapped in the two lower states in the phonon-assisted CPT.

For this phonon-assisted CPT experiment, a SAW driven at $\omega_m = 818 MHz$ is coupled to the NV center in diamond. The two optical fields are detuned by two acoustic optical modulators (AOMs). The $m_s = \pm 1$ states are split into $\omega_B / 2\pi = 24 MHz$ apart bringing an external magnetic field closer to a NV center. Another optical field is fixed at ω_0 which is detuned exactly ω_m away from the resonant transition to E_y state. Initially, the NV center is prepared to be in the $m_s = 0$ state by using the green laser. Then, the power of two optical fields is set to be approximately equal such that $\Omega_R \approx \Omega_\pm$. When the frequency ω_0 of one optical field is tuned so that the difference between $\omega_0 + \omega_m$ and $\omega_\pm$ becomes exactly as the ground state splitting ($\approx 2.88GHz$) of a NV center. As soon as this Ranman Resonant condition is fulfilled, the destructive interference occurs and we can see the decrease in the fluorescence as shown in Fig. 7.3. In our case, due to the Zeeman splitting, the splitting of $m_s = +1$ and $m_s = -1$ would, consequently, be at $\approx (2.88 + 0.024)GHz$ and $\approx (2.88 - 0.024)GHz$. The experimental result is in total agreement with the corresponding Zeemen splitting. Moreover, these negative peaks are a direct manifestation of the phonon-assisted CPT process, revealing the coherent interaction between the SAW and the relevant electron spin coherence.

We have used the density matrix equations for the Λ-type three-level system to model the phonon-assisted CPT experiment. Note that the $m_s = \pm 1$ states exhibit a hyperfine splitting of 2.2 MHz due to coupling with the nitrogen nuclear spin with $I = 1$. These hyperfine states, which are included in our model, cannot be clearly resolved in the CPT experiment because of power broadening of the CPT peaks and the limited signal-to-noise ratio. With the assumption that $\Omega_R = \Omega_\pm$, the observed depth of the CPT peak yields $\Omega_R/2\pi = 8MHz$, in agreement with the Rabi frequency estimated from individual dipole optical or phonon-assisted optical transitions and with the Rabi frequency derived from the sideband spin transition experiment, which will be discussed in the next section.

7.4. Optically Driven Sideband Spin Transitions

One of the disadvantages of the Λ-type system in the NV center is the shorter spin coherence life time of the excited state. There is a way to avoid this by using stimulated Raman adiabatic passage (STIRAP)[112], which has been successfully demonstrated for NV centers. With the help of STIRAP, the electron can be transferred from $m_s = 0$ to $m_s = \pm 1$ states without passing though the upper excited state (E_y) by detuning from the respective optical dipole transitions. In this adiabatic limit, the three-level system becomes equivalent to an optically driven spin transition between the two lower states, with an effective Rabi frequency for the spin transition given by $\Omega_{ss} = \Omega_1\, \Omega_2/(2|\Delta|)$, where Ω_1 and Ω_2 are the Rabi frequencies for the two dipole transitions and Δ is the dipole detuning, as illustrated in Fig. 7.4 (a). In our case, we have two optical fields and one SAW acoustic field in our Λ-type system and we can modify the effective Rabi frequency for this phonon-assisted spin transition as:

$$\Omega_{ss} = \frac{\Omega_R\, \Omega_\pm}{2\,|\Delta|} = \frac{\Omega_0\, \Omega_\pm}{2\,|\Delta|\,\omega_m}\, g\sqrt{n} = g_{ss}\,\sqrt{n} \tag{7.4}$$

Here, g_{ss} is the single-phonon Rabi frequency for the sideband spin transition.

In Fig. 7.4 , we conducted the spectral domain experiment to demonstrate and characterize STIRAP with the detuning $\Delta/(2\pi) = 100 MHz$. The optical and RF power used in this experiment is relatively identical to the previous CPT experiment. The spin population of $m_s = \pm 1$ is detected by using the resonant excitation between $m_s = \pm 1$ to A_2 state followed by measuring the fluorescence. The pulse sequence used for this experiment is shown in Fig. 7.4 (b). As usual, the green laser is used to initialize the electron into the $m_s = 0$ ground state. SAW acoustic field was continuously applied through out the experiment. Both applied optical fields have

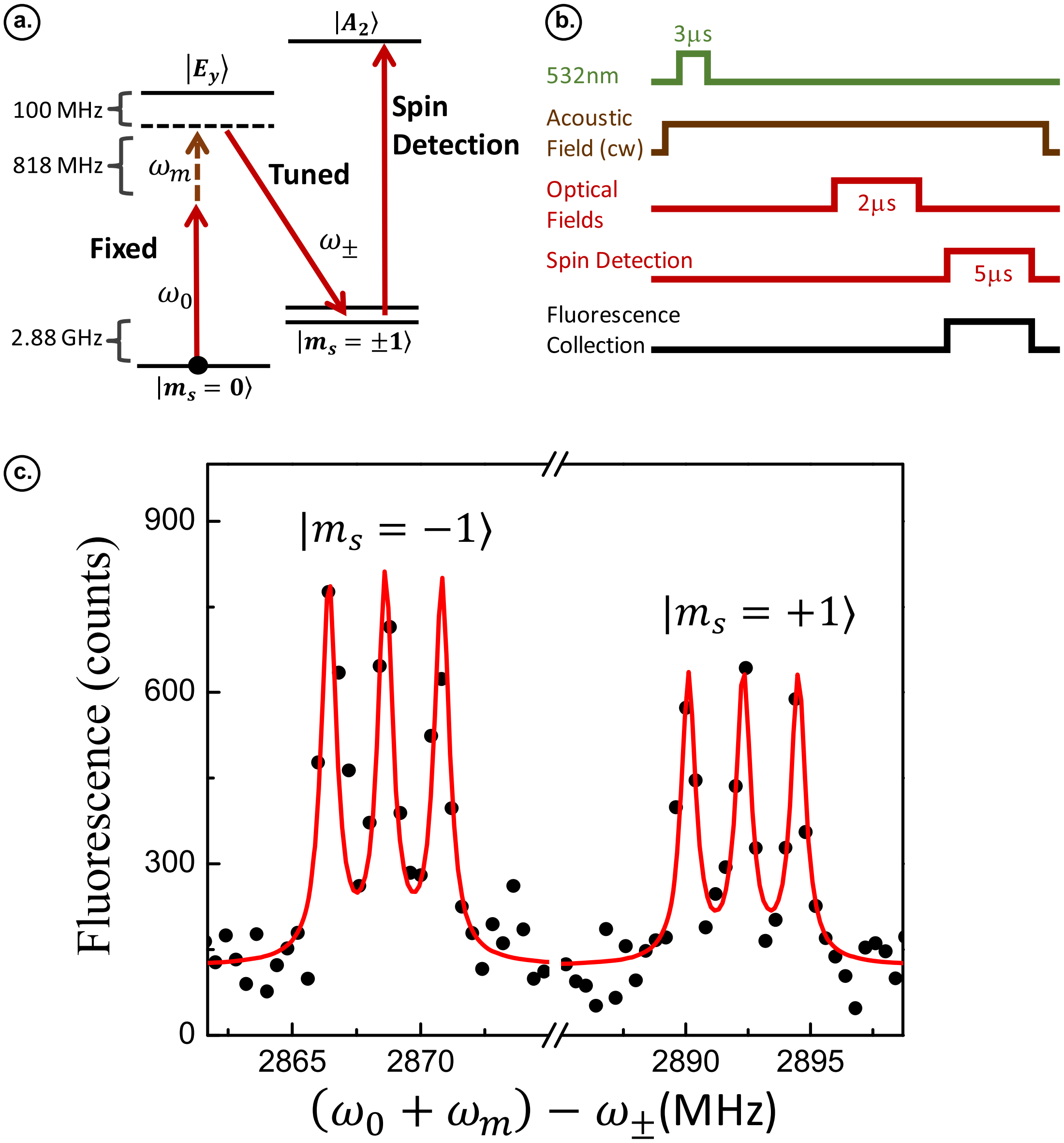

FIGURE 7.4. (a) Energy-level diagram including spin detection used for the sideband spin transition experiments. (b) Pulse sequence used for the spectral domain experiment. (c) Fluorescence from state A_2 as a function of $\omega_0 + \omega_m - \omega_\pm$. The solid red line is a fit to six Lorentzians with equal linewidths. A background due to optical pumping has been subtracted from the data.

the duration of $2\mu s$. At the end of each sequence, the detection of fluorescence is taken place via $m_s = \pm 1$ to A_2 transition. The fluorescence from A_2 is plotted as a function of detuning $\omega_0 + \omega_m - \omega_\pm$, while both ω_0 and ω_m are fixed. The spectral linewidth (full width at half maximum) of the transition resonances is 0.7 MHz, in agreement with the expected spin dephasing rate. The clearly resolved hyperfine structure of the $m_s = \pm 1$ states, with a 2.2 MHz hyperfine splitting, demonstrates that the sideband spin transitions are nuclear-spin selective, thus allowing the use of nuclear spins in quantum acoustics.

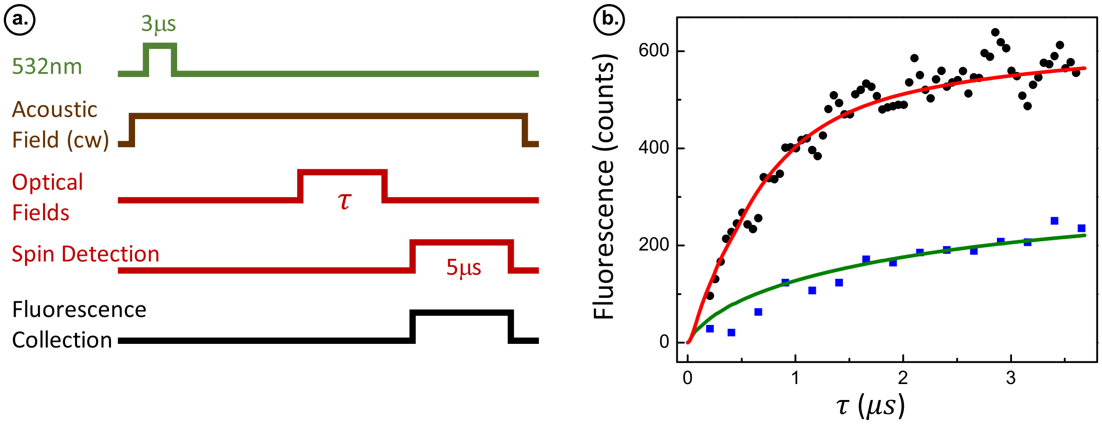

FIGURE 7.5. (a) Pulse sequence used for the transient sideband spin transition experiment. (b) Fluorescence from state A_2 as a function of the optical pulse duration. Solid circles: $\omega_0+\omega_m-\omega_\pm$ satisfies the Raman resonant condition for the sideband spin transition. Solid squares: $\omega_0+\omega_m-\omega_\pm$ is 6.5 MHz detuned from the Raman resonant condition (the data are smoothed). The solid lines are the theoretical calculations.

For the time domain measurement, we use the pulse sequence shown in Fig. 7.5 (a) which is similar to the spectral domain measurement except the fact that the duration of the optical driving fields is a variable parameter. The experimental results are plotted with respect to the duration of the optical driving field in Fig. 7.5 (b). We have shown two data sets. The solid circles represent the fluorescence from state A_2 as a function of the optical pulse duration, while $\omega_0, \omega_\pm$ and ω_m are fixed so that the Raman resonant condition for the sideband spin transition is satisfied for the state with $m_s = +1$ and $m_n = +1$, where m_n denotes nitrogen nuclear-spin projection. The initial rise of the fluorescence is primarily due to the sideband spin transition from the $m_s = 0$ state to the $m_s = +1$ state, with the rise time determined by Ω_{ss}.

Optical pumping resulting from the excitation and subsequent decay of the upper state can also lead to population in the $m_s = +1$ state.

The experimental result is plotted as the solid squares in Fig. 7.5 with the detuning frequency $(\omega_0 + \omega_m - \omega_\pm)/2\pi \approx 6.5$ MHz away from the Raman resonant condition. The solid lines show the theoretical calculations based on the density matrix equations, where we have taken $\Omega_R = \Omega_\pm$ and Γ_1, the decay rate from the E_y state to $m_s = \pm 1$ states,as adjustable parameters. The calculations yield $\Gamma_1/2\pi = 1.8$ MHz and $\Omega_R/2\pi = 8$ MHz,which agrees with the Rabi frequency derived from the phonon-assisted CPT experiment using the same optical powers. From these results, we obtain an effective Rabi frequency for the sideband spin transition, $\Omega_{ss}/2\pi = 0.3$ MHz. The strong agreement between the experiment and theory shows that both the sideband spin transitions and the optical pumping are well characterized by the density matrix equations.

In the limit of large dipole detuning, the upper-state population in the Λ-type system scales with $1/\Delta^2$. Both the optical pumping rate and the optically induced decoherence rate, γ_{opt}, thus also scale with $1/\Delta^2$. In comparison, Ω_{ss} scales with $1/\Delta$. In this regard, strong excited state mediated spin-phonon coupling can be achieved with negligible optical pumping or optically induced decoherence. For example, by setting $\Omega_\pm/|\Delta|$ and $\Omega_0/|\Delta|$ to 1/60, we keep $\gamma_{opt}/2\pi$ to about 1 kHz. With $|\Delta| = 25\omega_m$, Eq (7.4) then yields a single-phonon Rabi frequency g_{ss} that is three orders of magnitude greater than what can be achieved with direct ground-state spin-phonon coupling. More optimal excited-state-mediated spin-phonon coupling with greater g_{ss} and smaller γ_{opt} can be achieved by exploiting techniques such as a shortcut to adiabatic passage.

In summary, by coupling a SAW to an electron spin in diamond through a Λ-type three-level system, we have realized both phonon-assisted CPT and optically driven sideband spin transitions. These experiments demonstrate that we can take advantage of the strong excited-state electron-phonon interaction to mediate and control the coupling between spin and mechanical degrees of freedom while avoiding decoherence associated with the excited state. Note that Λ-type three-level systems with strong excited-state strain coupling provide an excellent experimental platform for exploring spin-based quantum acoustics.

Our approach can also be extended to other emerging spin systems with spin defect centers such as SiC, as well as to quantum-dot and superconducting systems. A diamond nanomechanical resonator featuring optically driven sideband spin transitions resembles a trapped-ion system. For a resonator with a modest mechanical Q factor, phonon lasing from a single spin, as well as cooling of the mechanical resonator via coupling to an electron spin, can be explored. A nanomechanical resonator with a sufficiently high mechanical Q factor can enable us to achieve strong spin-phonon coupling at the level of a single phonon and to pursue the highly successful paradigm of trapped-ion-based quantum computing in a solid-state system.

CHAPTER VIII

CONCLUSION

8.1. Summary

In this dissertation, we have demonstrated the coupling of mechanical vibrations to a single spin qubit embedded in diamond using optical sideband transitions and have developed the technical approach to fabricate spin-mechanical systems that can take advantage of unique properties of diamond and especially spin qubits in diamond

More specifically, we have demonstrated the quantum control of the internal states of a NV center by using sideband transitions and by taking advantage of strong excited-state electron-phonon coupling of NV centers. We have realized Rabi oscillations of a NV center by coupling the NV simultaneously to both optical and SAW fields in the resolved-sideband regime. Quantum interferences between the optomechanical sideband and the direct dipole-optical (or carrier) transitions have also been observed. In addition, we have also realized strong spin-mechanical coupling by exploiting dark states in a Λ-type three-level system. These studies establish firmly the physical mechanisms and processes that will be used for coherent coupling between electron spins and mechanical vibrations in a spin-mechanical system.

We have successfully fabricated diamond nanomechanical resonators using a diamond-on-insulator platform. The elaborate fabrication process overcame many obstacles in nearly all essential steps, including wafer bonding, deposition of SiN mask, mask transfer to SiN, as well as O_2 and Ar/Cl reactive ion etching of diamond. In addition, we have also further developed the experimental technique[50] to the generation of high quality single NV centers within 100 nm of the diamond surface via ion implantation. For this process, a step-wise thermal annealing up to 1200 degrees and a careful surface treatment including oxygen termination at a temperature of 500 degree are crucial for creating optically stable NV centers, i.e. NV centers with absorption linewidth less than a few hundred MHz at low temperature.

8.2. Future Work

The experimental progresses made in this dissertation open the door to using resolved-sideband coupling for quantum control of both the atom-like internal states and the motional states of a diamond nanomechanical oscillator, leading to the realization of a solid-state analog of trapped ions. With the robust electron spin coherence in diamond, the next immediate technical challenge is to realize diamond nanomechanical resonators with long lifetime for mechanical vibrations. Given the exceptionally small intrinsic mechanical loss in diamond, the primary mechanical loss mechanism is clamping loss[113–117]. For the next generation of diamond nanomechanical resonators, a phononic crystal structure[118–122] can be used to isolate the mechanical modes from the mechanical support, thus suppressing the clamping loss.

In addition to NV centers, diamond can also host other spin qubit systems such as silicon vacancy centers and germanium vacancy centers. These centers can feature properties that are in many aspects superior to those of NV centers. The technique of generating near-surface single NV centers in diamond via ion implantation demonstrated in our work can be directly applied to create other defect enters such as silicon vacancy and germanium vacancy centers in diamond.

With much improved diamond-based spin qubits and nanomechanical resonators, it will be promising to realize a new solid-state experimental platform based on the coherent coupling between spin and mechanical degrees of freedom to implement quantum computers

APPENDIX

SUPPLEMENTARY INFORMATION

A.1. Estimated Amplitude of the SAWs

We use our measurement of optomechanically-driven Rabi oscillations to estimate the amplitude of the IDT-generated SAW, A_{SAW} . The position operator for the harmonic oscillator is

$$\hat{x} = \sqrt{\frac{\hbar}{2m\omega_m}}(\hat{b} + \hat{b}^{\dagger}) \tag{A.1}$$

where m is the effective oscillator mass, ω_m is the mechanical SAW frequency, and $\hat{b}$ and $\hat{b}^{\dagger}$ are the creation and annihilation operators for the phonon mode. The amplitude is thus given by

$$A_{SAW} = \sqrt{\frac{\hbar}{2m\omega_m}}\, 2\sqrt{n} \tag{A.2}$$

Here n is the mean phonon number. Moreover,

$$\Omega = \frac{g\sqrt{n}\Omega_0}{\omega_m} \tag{A.3a}$$

$$g = Dk_m\sqrt{\frac{\hbar}{2m\omega_m}} \tag{A.3b}$$

where Ω is the effective Rabi frequency for the sideband transition, is the optical Rabi frequency, g is the effective electron-phonon coupling rate, D is the deformation potential for the NV center excited state, and k_m is the wave number of the phonon mode. Combining Eq. (A.2) and Eq. (A.3) gives

$$A_{SAW} = 2\,\frac{\omega_m}{k_m}\frac{\Omega}{\Omega_0}\frac{1}{D} \tag{A.4}$$

With $\Omega/2\pi = 66MHz$, $\Omega_0/2\pi = 290MHz$, $\omega_m/2\pi = 940MHz$, $k_m/2\pi = 1/(6\mu m)$, and $D/2\pi = 610THz$, we can estimate the amplitude of the surface acoustic wave, $A_{SAW} = 0.7pm$ based on the measured Rabi frequency.

We now compare this to an order-of-magnitude estimate for the amplitude of the SAWs based on the driving power of the IDT and the IDT dimensions. The SAWs propagate away from the IDT at velocity, v . The displacement is largest at the surface and falls off on a length scale of about one wavelength, λ . As an approximation we will first assume the SAW energy is uniformly distributed between the surface and one wavelength deep. The energy density is then given by

$$\frac{E}{V} = \frac{P_{RF}}{A\,v} \tag{A.5}$$

where P_{RF} is the power transmitted by the IDT and is the cross-sectional area through which the SAW travels. Taking $A = L\,\lambda\,\frac{v}{\omega_m}2\pi$, where L is the length of the IDT, leads to

$$\frac{E}{V} = \frac{P_{RF}\omega_m}{2\pi\,L\,v^2} \tag{A.6}$$

The energy density of the mechanical wave is given by

$$\frac{E}{V} = 2\rho\,\omega_m^2\,A_{SAW}^2 \tag{A.7}$$

with ρ as the mass density of diamond. Combining Eq. (A.6) and Eq. (A.7), and rearranging gives

$$A_{SAW} = \sqrt{\frac{P_{RF}}{4\pi\ L\ v^2\ \rho\omega_m}(\mathrm{A.8})}$$

The power applied to the IDT was about . We assume 50% of the power is transmitted to the device. The electromechanical coupling efficiency of the IDT is estimated to be $\approx 0.05\%$[123, 124]. Also, the IDT transmits in both directions so only half the power reaches the NV center. Furthermore, the NV centers used in this work were typically located roughly 0.7λ from the surface so we estimate that they will see half the average power. We set $P_{RF} = 0.45 \times 1/2 \times 0.0005 \times 1/2 \times 1/2$. Using $L = 400\mu m, \rho = 3500 kg/m^3$, and $v = \lambda\omega/(2\pi)$, we get $A_{SAW} \approx 3pm$. This is likely an overestimate since we have used overly optimistic values for the IDT efficiency. In this regard, our predicted amplitude is in general agreement with the amplitude derived from the Rabi frequencies.

A.2. Optical Rabi Frequency and Power Broadening

The dependence of the carrier resonance linewidth on optical power provides an estimate for the power dependence of the optical Rabi frequency. The linewidth of the NV center optical dipole transition is subject to spectral diffusion due to the off-resonant excitation step in the PLE measurement, as well as to power broadening. The power broadened FWHM, F_p , is given by

$$F_p \times 2\pi = 2\gamma\sqrt{1 + \frac{\Omega_0^2}{\gamma\Gamma}} \qquad (\mathrm{A.9})$$

where γ is the coherence decay rate, and Γ is the excited state population decay rate. We treat the spectral diffusion as an inhomogeneous broadening yielding a Gaussian distribution with a linewidth of F_s. The convolution of the power broadening and spectral diffusion is a Voigt profile with a FWHM approximated by

$$F \approx 0.535\, F_p \,+\, \sqrt{0.217\, F_p^2 + F_s^2} \tag{A.10}$$

We take $\Gamma/2\pi = 14MHz$ and $\gamma/2\pi = 20MHz$. To fit the data at low optical power we use $F_s = 135MHz$. To fit the higher power data we take $\Omega/2\pi = \sqrt{P_0} \times 65MHz$, where is the optical power given in units of μW. The values of $\Omega/2\pi$ used in these experiments are therefore estimated to range between about 10 MHz and 300 MHz.

A.3. Interference between Carrier and Sideband Transitions: Theory

For phonon-assisted sideband transition experiment,we simultaneously drive the carrier and sideband transitions and observe a phase dependent interference effect. To model this interference experiment, we consider a two level system with transition frequency ω_0. There are two complex Rabi frequencies $\Omega_a = \bar{\Omega}_a e^{-i\omega_a t + i\phi_a}$ and $\Omega_b = \bar{\Omega}_b e^{-i\omega_b t + i\phi_b}$ with ω_a and ϕ_a as the frequency and phase of the carrier excitation and ω_b and ϕ_b for the sideband excitation (Fig. A.1).(ω_b and ϕ_b are the sum of the frequencies and phases of the optical and acoustic fields which together drive this transition.)

From the optical Bloch equations, we get

$$\dot{\rho}_{22} = -\Gamma \rho_{22} + \frac{1}{2}[-i\Omega\rho_{22} + h.c.] \tag{A.11a}$$

$$\dot{\rho}^a_{12} = (-\gamma + i\omega_0)\rho^a_{12} + \frac{i}{2}\Omega^*_a(\rho_{22} - \rho_{11}) \tag{A.11b}$$

$$\dot{\rho}^b_{12} = (-\gamma + i\omega_0)\rho^b_{12} + \frac{i}{2}\Omega^*_b(\rho_{22} - \rho_{11}) \tag{A.11c}$$

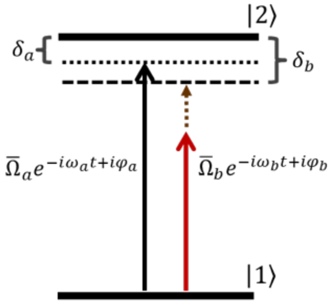

FIGURE A.1. Energy level diagram for the interference measurement

where $\Omega = \Omega_a + \Omega_b$ and $\rho_{12} = \rho^a_{12} + \rho^b_{12}$. We take

$$\dot{\rho}^b_{12} = (-\gamma + i\omega_0)\rho^b_{12} + \frac{i}{2}\Omega^*_b(\rho_{22} - \rho_{11}) \tag{A.12a}$$

$$\rho^a_{12} = \bar{\rho}^a_{12} e^{i\omega_a t} \tag{A.12b}$$

$$\rho^b_{12} = \bar{\rho}^b_{12} e^{i\omega_b t} \tag{A.12c}$$

and substitute into Eq. (A.11b) and Eq. (A.11c) to get

$$\dot{\rho}^a_{12} = (-\gamma + i\delta_a)\rho^a_{12} + \frac{i}{2}\bar{\Omega}_a e^{-i\phi_a}(\rho_{22} - \rho_{11}) \tag{A.13a}$$

$$\dot{\rho}^b_{12} = (-\gamma + i\delta_b)\rho^b_{12} + \frac{i}{2}\bar{\Omega}_b e^{-i\phi_b}(\rho_{22} - \rho_{11}) \tag{A.13b}$$

where $\delta_{a,b} = \omega_0 - \omega_{a,b}$. Solving these in the steady state gives

$$\rho_{12}^{a} = \frac{-i\bar{\Omega}_a e^{i\phi_a}}{2(-\gamma + i\delta_a)} \tag{A.14a}$$

$$\rho_{12}^{b} = \frac{-i\bar{\Omega}_b e^{i\phi_b}}{2(-\gamma + \delta_b)} \tag{A.14b}$$

where we have taken a zeroth order approximation and set $(\rho_{22} - \rho_{11}) = 0$.

Next we combine Eq. (A.14) and Eq. (A.12), and then substitute into Eq. (A.11a). We will get

$$\dot{\rho}_{22} = -\Gamma\rho_{22} + \frac{1}{2}\left[\frac{\bar{\Omega}_a^2}{2(\gamma - i\delta_a)} + \frac{\bar{\Omega}_b^2}{2(\gamma - i\delta_b)} + \frac{\bar{\Omega}_a\bar{\Omega}_b e^{-i\Delta\omega t} e^{i\Delta\phi}}{2(\gamma - i\delta_b)} + \frac{\bar{\Omega}_a\bar{\Omega}_b e^{i\Delta\omega t} e^{-i\Delta\phi}}{2(\gamma - i\delta_a)} + c.c.\right] \tag{A.15}$$

where $\Delta\omega = (\omega_a - \omega_b)$ and $\Delta\phi = (\phi_a - \phi_b)$.

Now we assume

$$\rho_{22} = \bar{\rho}_{22}^{(0)} + \bar{\rho}_{22}^{(+)} e^{i\Delta\omega t} + \bar{\rho}_{22}^{(-)} e^{-i\Delta\omega t} \tag{A.16}$$

which combined with Eq. (A.15) gives

$$\dot{\rho}_{22}^{(0)} = -\Gamma\rho_{22}^{(0)} + \frac{1}{2}\left[\frac{\bar{\Omega}_a^2}{2(\gamma - i\delta_a)} + \frac{\bar{\Omega}_b^2}{2(\gamma - i\delta_b)} + c.c.\right] \tag{A.17a}$$

$$\dot{\rho}_{22}^{(0)} = (-\Gamma - i\Delta\omega)\bar{\rho}_{22}^{(+)} + \frac{1}{2}\left[\frac{\bar{\Omega}_a\bar{\Omega}_b e^{i\Delta\phi}}{2(\gamma - i\delta_b)} + c.c.\right] \tag{A.17b}$$

$$\dot{\rho}_{22}^{(0)} = (-\Gamma + i\Delta\omega)\bar{\rho}_{22}^{(+)} + \frac{1}{2}\left[\frac{\bar{\Omega}_a\bar{\Omega}_b e^{i\Delta\phi}}{2(\gamma - i\delta_a)} + c.c.\right] \tag{A.17c}$$

Solving these in the steady state and substituting back into Eq. (A.16), we arrive at an expression for the excited state population.

$$\rho_{22} = \frac{1}{2\Gamma}\left[\frac{\bar{\Omega}_a^2}{2(\gamma - i\delta_a)} + \frac{\bar{\Omega}_b^2}{2(\gamma - i\delta_b)} + \frac{\bar{\Omega}_a\bar{\Omega}_b e^{-i\Delta\omega t}e^{i\Delta\phi}}{2(\gamma - i\delta_b)(\Gamma + i\Delta\omega)} + \frac{\bar{\Omega}_a\bar{\Omega}_b e^{i\Delta\omega t}e^{-i\Delta\phi}}{2(\gamma - i\delta_a)(\Gamma - i\Delta\omega)} + c.c.\right] \tag{A.18}$$

Our measurement of the excited state population, by means of the spontaneously emitted fluorescence, averages over a long time period. This means that when $\Delta\omega$ is nonzero the phase dependent terms in Eq. (A.18) averages to zero. When $\Delta\omega = 0$ (and therefore $\delta_a = \delta_b = \delta$) , the expression simplifies to

$$\rho_{22} = \frac{1}{2\Gamma}\left[\frac{\bar{\Omega}_a^2\bar{\Omega}_b^2}{2(\gamma - i\delta)} + \frac{\bar{\Omega}_a\bar{\Omega}_b}{(\gamma - i\delta)}cos(\Delta\phi) + c.c.\right] \tag{A.19}$$

which has a nonzero phase dependent term that goes as the cosine of the phase difference. Unity contrast in the interference fringes can be achieved if $\Omega_a = \Omega_b$.

A.4. Optomechanically Driven Rabi Oscillations: Theory

In this section we discuss optomechanically driven Rabi oscillations, in particular contributions from the carrier (i.e. direct optical dipole) transition to the Rabi oscillation experiment. We consider a two-level system, where the upper state $|e\rangle$ couples to a lower state $|g\rangle$ via an acoustic and laser field. The full Hamiltonian for this system is as follows:

$$H = \hbar\omega_m b^\dagger b + \hbar\omega_0\sigma_+\sigma_- + \hbar\frac{\Omega_0}{2}[\sigma_+ e^{-i\omega_L t} + h.c.] + \hbar g(b + b^\dagger)\sigma_+\sigma_- \tag{A.20}$$

where the laser field has Rabi frequency Ω_0 and laser frequencyω_L . The Pauli operators correspond to the two-level system with transition frequency ω_0, whereas the $b^\dagger, b$ denote the phonon operators with frequency ω_m . The effective electron-phonon coupling rate is g . The Hamiltonian for the first red sideband transition is given by

$$H_R = i\hbar\frac{\Omega_0 g}{2\omega_m}(b\sigma_+ - b^\dagger\sigma_-) = i\hbar\frac{\Omega}{2}(b\sigma_+ - b^\dagger\sigma_-) \tag{A.21}$$

Fig. A.2 shows the optomechanically driven Rabi oscillations obtained using H_R and the same parameters as those from the experiment, indicating an overall agreement between the theory and experiment.

The sideband detuned laser field can couple directly to the carrier transition and as a result induces generalized Rabi oscillations of the excited state population. Fig. A.3 shows the calculated generalized Rabi oscillations using parameters the same as those for Fig. A.2, except that the acoustic field is now turned off. For comparison, we also compare directly in Fig. A.3 the generalized Rabi oscillations with the optomechanically-induced Rabi oscillations shown in Fig. A.2. The generalized Rabi oscillations are not observable in our experiments because of the limited time resolution (2.8 ns).

We also note that in addition to the optomechanically-driven Rabi oscillations due to H_R, the combined optical and mechanical coupling can also lead to a weak temporal modulation (with frequency ω_m) in the excited state population. This modulation is not observable in our experiments, again due to the limited time resolution.

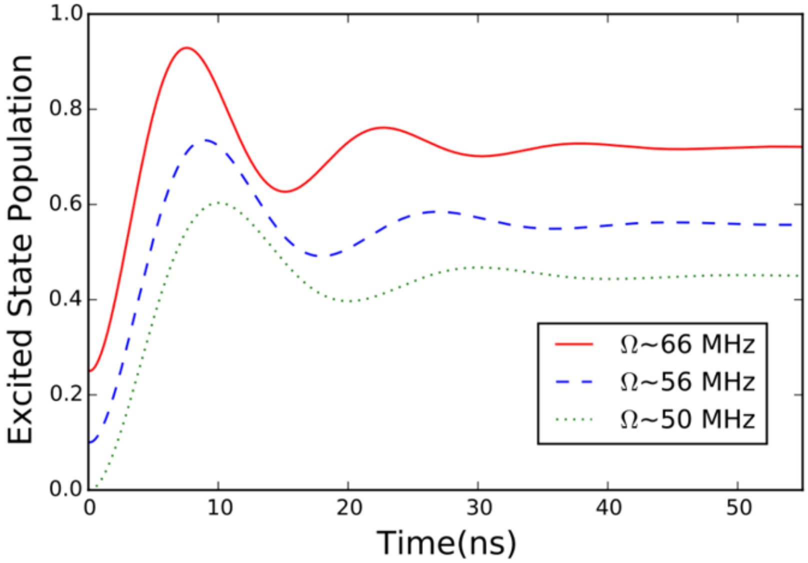

FIGURE A.2. Calculated optomechanically driven Rabi oscillations for three different RF powers. For clarity, the oscillations displayed are vertically offset. The effective Rabi frequency is indicated in the figure.

A.5. Theoretical Model for Λ-type System

We consider a Λ-type three-level system, driven by two optical fields and an acoustic field, as shown in Fig. A.4. The two dipole optical transitions, with frequency v_1 and v_2, couple to the two optical fields, with frequency ω_1 and ω_2 and Rabi frequency $_1$ and Ω_2, respectively. With the rotating wave approximation, the Hamiltonian of the system, is given by

$$\begin{aligned} H =& \hbar\omega_m b^\dagger b - \hbar v_1 \left|g_1\right\rangle \left\langle g_1\right| - \\ & \hbar v_2 \left|g_1\right\rangle \left\langle g_1\right| + \hbar g(b^\dagger + b) \left|e\right\rangle \left\langle e\right| + \\ & \hbar\frac{\Omega_1}{2}(e^{i\omega_1 t} \left|e\right\rangle \left\langle g_1\right| + h.c.) + \hbar\frac{\Omega_2}{2}(e^{i\omega_2 t} \left|e\right\rangle \left\langle g_2\right| + h.c.) \end{aligned} \tag{A.22}$$

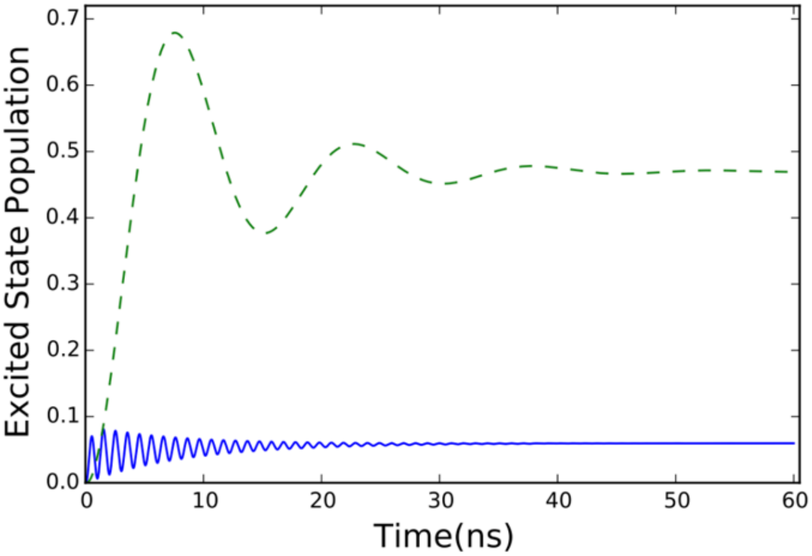

FIGURE A.3. Calculated generalized Rabi oscillations (solid blue curve) using parameters the same as those for Fig. A.2, except that the acoustic field is turned off. For comparison, the dashed curve shows the optomechanically driven Rabi oscillations (with $\Omega \approx 66MHz$) in Fig. A.2

.

where $b^\dagger$ and b are the creation and annihilation operators for the acoustic field with frequency ω_m and g is the electron-phonon coupling rate. Applying the Schrieffer-Wolff transformation

$$U = exp\left[\frac{g}{\omega_m}(b^\dagger - b)\left|e\right\rangle\left\langle e\right|\right] \tag{A.23}$$

to the Hamiltonian gives

$$\begin{aligned}\widetilde{H} =&\hbar\omega_m b^\dagger b - \hbar v_1 \left|g_1\right\rangle\left\langle g_1\right| - \\ &\hbar v_2 \left|g_1\right\rangle\left\langle g_1\right| + \hbar\frac{g^2}{\omega_m}\left|e\right\rangle\left\langle e\right| + \\ &\hbar\frac{\Omega_1}{2}(e^{i\omega_1 t + \frac{g}{\omega_m}(b^\dagger - b)}\left|e\right\rangle\left\langle g_1\right| + h.c.) + \\ &\hbar\frac{\Omega_2}{2}(e^{i\omega_2 t + \frac{g}{\omega_m}(b^\dagger - b)}\left|e\right\rangle\left\langle g_2\right| + h.c.)\end{aligned} \tag{A.24}$$

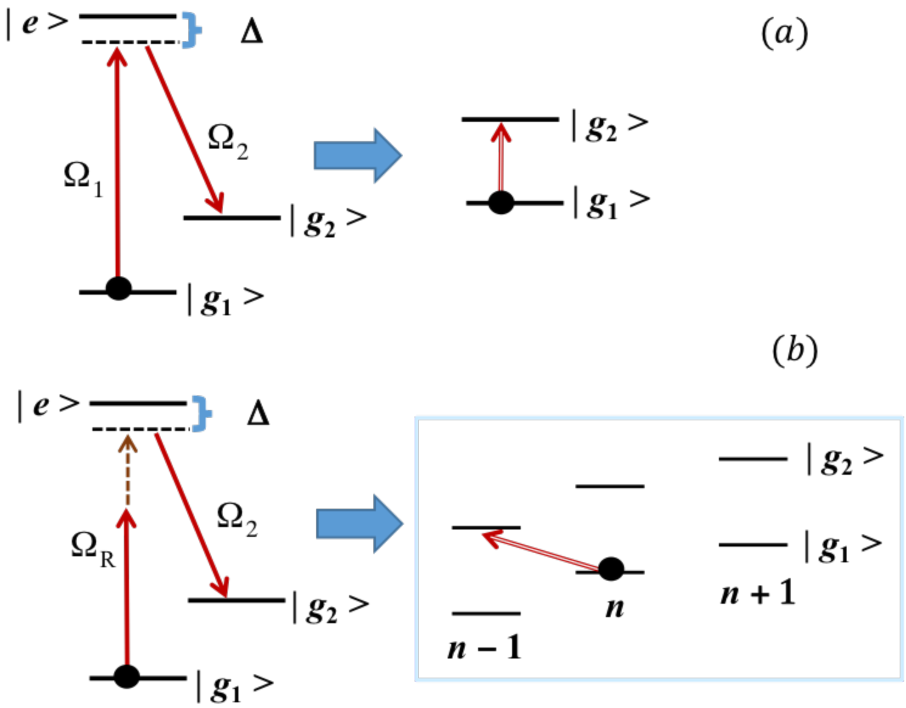

FIGURE A.4. (a) Schematic of a Λ-type three-level system driven by two optical fields with respective Rabi frequency, Ω_1 and Ω_2. In the limit of large dipole detuning, Δ, the system becomes equivalent to an optically-driven transition between the two lower states. (b) Schematic of a Λ-type three-level system driven by an acoustic field (brown dashed line) as well as two optical fields. The $|g_1\rangle$ to $|e\rangle$ transition is a phonon-assisted transition with effective Rabi frequency Ω_R. In the limit of large Δ, the system becomes equivalent to an optically-driven transition between the phonon ladders of the two lower states, where n denotes the phonon number.

which has the same form as the trapped ion Hamiltonian. Transforming to an interaction picture, we then have

$$\begin{aligned}\widetilde{H} =& \hbar\frac{\Omega_1}{2}(e^{i\Delta_1 t}e^{-\frac{g}{\omega_m}(b^\dagger e^{i\omega_m t}-be^{-i\omega_m t})}\left|e\right\rangle\left\langle g_1\right| + h.c.) + \\ & \hbar\frac{\Omega_2}{2}(e^{i\Delta_2 t}e^{-\frac{g}{\omega_m}(b^\dagger e^{i\omega_m t}-be^{-i\omega_m t})}\left|e\right\rangle\left\langle g_2\right| + h.c.)\end{aligned} \tag{A.25}$$

where $\Delta_1 = (v_1 - g^2/\omega_m) - \omega_1$ and $\Delta_2 = (v_2 - g^2/\omega_m) - \omega_2$ are the effective detunings of the two optical fields from their respective dipole transitions.

We assume that the Ω_1 field is tuned near the red phonon-sideband of the $|g_1\rangle$ to $|e\rangle$ transition ($\Delta_1 \approx \omega_m$) and the Ω_2 field is tuned near the $|g_2\rangle$ to $|e\rangle$ transition ($\Delta_2 \approx 0$). Expanding $\widetilde{H}$ in g/ω_m, which can be viewed as an effective Lamb-Dicke parameter for our solid state system, and keeping only the nearly resonant terms, we can approximate the interaction Hamiltonian as

$$H_I = \hbar \frac{\Omega_1}{2} \frac{g}{\omega_m} \left[b e^{i(\Delta_1 - \omega_m)t} |e\rangle \langle g_1| + h.c. \right] + \hbar \frac{\Omega_2}{2} \left[e^{i\Delta_2 t} |e\rangle \langle g_2| + h.c. \right] \tag{A.26}$$

which is similar to a Hamiltonian for a Λ-type three-level system driven by two optical fields, with effective detuning, $\Delta_R = \Delta_1 - \omega_m$ and Δ_2, and effective Rabi frequency, $\Omega_R = g\sqrt{n}\Omega_1/\omega_m$ and $\Omega_2 2$, respectively, where n denotes the average phonon number. Note that the Raman resonant condition is $\Delta_R = \Delta_2$. The above Hamiltonian is also valid for relatively large Δ_R and Δ_2, as long as $\Delta_R \approx \Delta_2$. With $\Delta_R = \Delta_2$, the Hamiltonian given by Eq. (A.26) features a dark state,

$$|\Psi_d\rangle = \frac{1}{\sqrt{\Omega_R^2 + \Omega_2^2}} \left[\Omega_R |g_2\rangle - \Omega_2 |g_1\rangle \right] \tag{A.27}$$

with $H_I |\Psi_d\rangle = 0$. This dark state is decoupled from state $|e\rangle$, leading to phonon-assisted CPT of the electron in the two lower state. The equations of motion for the density matrix elements,ρ_{ij} , in the rotating frame, which we have used to model the experiments, can also be derived from H_I and are given as

$$\dot{\rho}_{e1} = -(i\Delta_R + \gamma)\rho_{e1} + \frac{i\Omega_R}{2}(\rho_{ee} - \rho_{11} - \frac{i\Omega_2}{2}\rho_{21} \tag{A.28a}$$

$$\dot{\rho}_{e2} = -(i\Delta_2 + \gamma)\rho_{e2} + \frac{i\Omega_R}{2}(\rho_{ee} - \rho_{22} - \frac{i\Omega_2}{2}\rho_{12} \tag{A.28b}$$

$$\dot{\rho}_{21} = -[i(\Delta_R - \Delta_2) + \gamma_s]\rho_{21} + \frac{i\Omega_R}{2}\rho_{2e} - \frac{i\Omega_2}{2}\rho_{e1} \tag{A.28c}$$

$$\dot{\rho}_{ee} = -\Gamma\rho_{ee} + (\frac{i\Omega_R}{2}\rho_{e1} + c.c.) + (\frac{i\Omega_2}{2}\rho_{e2} + c.c.) \tag{A.28d}$$

$$\dot{\rho}_{11} = \Gamma_1\rho_{ee} - (\frac{i\Omega_R}{2}\rho_{e1} + c.c.) \tag{A.28e}$$

$$\dot{\rho}_{22} = \Gamma_2\rho_{ee} - (\frac{i\Omega_2}{2}\rho_{e2} + c.c.) \tag{A.28f}$$

where γ_s and γ are the decay rates for the spin coherence and optical dipole coherence, respectively,$\Gamma = \Gamma_1 + \Gamma_2$ is the total decay rate for the upper state population, with Γ_1 and Γ_2 being the decay rate to $|g_1\rangle$ and $|g_2\rangle$, respectively. For the theoretical calculation, we have used $\gamma_s/2\pi = 0.35MHz$, which is primarily due to spin dephasing induced by the nuclear spin bath, and $\Gamma/2\pi = 14MHz$, as determined experimentally. We have assumed $\gamma = \Gamma/2 + \gamma_{orb}$, where γ_{orb} is the dephasing rate due to coupling to the orbital degrees of freedom and have taken $\gamma_{orb}/2\pi = 12MHz$[125]. We have also used $\Gamma_1/2\pi = 1.8MHz$, as derived from the optical pumping experiment. NV spectral diffusion is treated as a Gaussian distribution of the optical transition frequency with a linewidth of 140 MHz, as derived from the excitation spectrum of the E_y resonance.

A.6. Effects of Strain-induced electric fields

For our experiments, the strain field of a SAW can induce a propagating electric field in the piezoelectric ZnO layer. This strain-induced electric field can couple to NV centers, though theoretically this coupling is expected to be small compared with the deformation potential coupling. This is because the strain-induced electric field is relatively small[126], and also because this electric field is mostly confined in the ZnO layer and the NV center is about a few microns (3 μm in our experiment) below the diamond surface. For an experimental confirmation, we rapidly heated up the sample from 8 K to room temperature. When we cooled the sample back down again to 8 K, the phonon sidebands in the excitation spectrum vanished, but the IDT still functions, though with a slightly reduced amplitude. In this case, the rapid temperature change broke or significantly weakened the bonds between the ZnO and diamond. Although the electric field induced by the strain field still propagates in the ZnO layer, the SAW no longer propagates in diamond. We can only recover the phonon sideband by removing and then re-depositing the ZnO layer. Our experiments show that the coupling between the strain-induced electric field and the NV center used in our experiment is negligible compared with the deformation potential coupling.

REFERENCES CITED

1. Jordan, S. P. Fast Quantum Computation at Arbitrarily Low Energy. *Physical Review A* **95,** 032305 (Mar. 2017).

2. Farhi, E., Goldstone, J., Gutmann, S. & Sipser, M. A Limit on the Speed of Quantum Computation in Determining Parity. *Physical Review Letters* **81,** 5442–5444 (Dec. 1998).

3. DiVincenzo, D. P. *et al.* Quantum Computation. *Science* **270,** 255–261 (1995).

4. Wallraff, A. *et al.* Strong Coupling of a Single Photon to a Superconducting Qubit Using Circuit Quantum Electrodynamics. en. *Nature* **431,** 162–167 (Sept. 2004).

5. Blais, A., Huang, R.-S., Wallraff, A., Girvin, S. M. & Schoelkopf, R. J. Cavity Quantum Electrodynamics for Superconducting Electrical Circuits: An Architecture for Quantum Computation. *Physical Review A* **69,** 062320 (June 2004).

6. Häffner, H., Roos, C. F. & Blatt, R. Quantum Computing with Trapped Ions. *Physics Reports* **469,** 155–203 (Dec. 2008).

7. Leibfried, D., Blatt, R., Monroe, C. & Wineland, D. Quantum Dynamics of Single Trapped Ions. *Reviews of Modern Physics* **75,** 281–324 (Mar. 2003).

8. Kielpinski, D., Monroe, C. & Wineland, D. J. Architecture for a Large-Scale Ion-Trap Quantum Computer. en. *Nature* **417,** 709–711 (June 2002).

9. Childress, L. & Hanson, R. Diamond NV Centers for Quantum Computing and Quantum Networks. *MRS Bulletin* **38,** 134–138 (Feb. 2013).

10. Acosta, V. & Hemmer, P. Nitrogen-Vacancy Centers: Physics and Applications. *MRS Bulletin* **38,** 127–130 (Feb. 2013).

11. Gustafsson, M. V. *et al.* Propagating Phonons Coupled to an Artificial Atom. en. *Science* **346,** 207–211 (Oct. 2014).

12. Wixforth, A., Kotthaus, J. P. & Weimann, G. Quantum Oscillations in the Surface-Acoustic-Wave Attenuation Caused by a Two-Dimensional Electron System. *Physical Review Letters* **56,** 2104–2106 (May 1986).

13. Manenti, R. *et al.* Surface Acoustic Wave Resonators in the Quantum Regime. *Physical Review B* **93,** 041411 (Jan. 2016).

14. Weiß, M. *et al.* Surface Acoustic Wave Regulated Single Photon Emission from a Coupled Quantum Dot–nanocavity System. *Applied Physics Letters* **109,** 033105 (July 2016).

15. Rabl, P. *et al.* A Quantum Spin Transducer Based on Nanoelectromechanical Resonator Arrays. en. *Nature Physics* **6,** 602–608 (Aug. 2010).

16. Golter, D. A., Oo, T., Amezcua, M., Stewart, K. A. & Wang, H. Optomechanical Quantum Control of a Nitrogen-Vacancy Center in Diamond. *Physical Review Letters* **116,** 143602 (Apr. 2016).

17. MacQuarrie, E. R., Gosavi, T. A., Bhave, S. A. & Fuchs, G. D. Continuous Dynamical Decoupling of a Single Diamond Nitrogen-Vacancy Center Spin with a Mechanical Resonator. *Physical Review B* **92,** 224419 (Dec. 2015).

18. Ovartchaiyapong, P., Lee, K. W., Myers, B. A. & Jayich, A. C. B. Dynamic Strain-Mediated Coupling of a Single Diamond Spin to a Mechanical Resonator. en. *Nature Communications* **5,** ncomms5429 (July 2014).

19. Teissier, J., Barfuss, A., Appel, P., Neu, E. & Maletinsky, P. Strain Coupling of a Nitrogen-Vacancy Center Spin to a Diamond Mechanical Oscillator. *Physical Review Letters* **113,** 020503 (July 2014).

20. MacQuarrie, E. R., Gosavi, T. A., Jungwirth, N. R., Bhave, S. A. & Fuchs, G. D. Mechanical Spin Control of Nitrogen-Vacancy Centers in Diamond. *Physical Review Letters* **111,** 227602 (Nov. 2013).

21. Golter, D. A. *et al.* Coupling a Surface Acoustic Wave to an Electron Spin in Diamond via a Dark State. *Physical Review X* **6,** 041060 (Dec. 2016).

22. Awschalom, D. D., Epstein, R. & Hanson, R. The Diamond Age Diamond Age of Spintronics. en. *Scientific American* **297,** 84–91 (2007).

23. Hall, L. T., Simpson, D. A. & Hollenberg, L. C. L. Nanoscale Sensing and Imaging in Biology Using the Nitrogen-Vacancy Center in Diamond. *MRS Bulletin* **38,** 162–167 (Feb. 2013).

24. Rondin, L. *et al.* Magnetometry with Nitrogen-Vacancy Defects in Diamond. en. *Reports on Progress in Physics* **77,** 056503 (2014).

25. Kucsko, G. *et al.* Nanometre-Scale Thermometry in a Living Cell. en. *Nature* **500,** 54–58 (Aug. 2013).

26. Schirhagl, R., Chang, K., Loretz, M. & Degen, C. L. Nitrogen-Vacancy Centers in Diamond: Nanoscale Sensors for Physics and Biology. en. *Annual Review of Physical Chemistry* **65,** 83–105 (Apr. 2014).

27. Wrachtrup, J. & Jelezko, F. Processing Quantum Information in Diamond. en. *Journal of Physics: Condensed Matter* **18,** S807 (2006).

28. Lenef, A. & Rand, S. C. Electronic Structure of the NV Center in Diamond: Theory. *Physical Review B* **53,** 13441 (1996).

29. Miyoshi, K. Structures and Mechanical Properties of Natural and Synthetic Diamonds. Chapter 8 (1998).

30. Maze, J. R. *et al.* Properties of Nitrogen-Vacancy Centers in Diamond: The Group Theoretic Approach. en. *New Journal of Physics* **13,** 025025 (2011).

31. Doherty, M. W. The theory of the nitrogen-vacancy colour centre in diamond (2012).

32. Evans, R. E., Sipahigil, A., Sukachev, D. D., Zibrov, A. S. & Lukin, M. D. Coherent optical emitters in diamond nanostructures via ion implantation. arXiv: `1512.03820` (Dec. 11, 2015).

33. Schirhagl, R., Chang, K., Loretz, M. & Degen, C. L. *Nitrogen-Vacancy Centers in Diamond: Nanoscale Sensors for Physics and Biology* en. `http://www.annualreviews.org/doi/10.1146/annurev-physchem-040513-103659`. review-article. Apr. 2014.

34. Aharonovich, I., Greentree, A. D. & Prawer, S. Diamond Photonics. en. *Nature Photonics* **5,** 397–405 (July 2011).

35. Ofori-Okai, B. K. *Optical and Spin Properties of Nitrogen Vacancy Centers in Bulk and Nanocrystalline Diamond* PhD thesis (Massachusetts Institute of Technology, 2013).

36. Golter, D. Optical Control of Electron Spins in Diamond. en_US (Jan. 2015).

37. Jamali, M. *et al.* Microscopic Diamond Solid-Immersion-Lenses Fabricated around Single Defect Ceneters by Focussed Ion Beam Milling. *Review of Scientific Instruments* **85,** 123703 (Dec. 2014).

38. Corporation, M. I. *LOW WORKING DISTANCE OPTIONS* <`http://resources.montanainstruments.com/help/article/link/low-working-distance-options`> (2016).

39. Peters, J. K. & Polyakov, S. *Simple and Inexpensive FPGA-Based Fast Multichannel Acquisition Board* `https://www.nist.gov/services-resources/software/simple-and-inexpensive-fpga-based-fast-multichannel-acquisition-board`. 2009-11-24T10:03-05:00.

40. Jensen, K., Kehayias, P. & Budker, D. en. in *High Sensitivity Magnetometers* (eds Grosz, A., Haji-Sheikh, M. J. & Mukhopadhyay, S. C.) *Smart Sensors, Measurement and Instrumentation* 19, 553–576 (Springer International Publishing, 2017).

41. Rondin, L. *et al.* Magnetometry with Nitrogen-Vacancy Defects in Diamond. en. *Reports on Progress in Physics* **77,** 056503 (2014).

42. Pham, L. M. *et al.* Magnetic Field Imaging with Nitrogen-Vacancy Ensembles. en. *New Journal of Physics* **13,** 045021 (2011).

43. Rugar, D., Budakian, R., Mamin, H. J. & Chui, B. W. Single Spin Detection by Magnetic Resonance Force Microscopy. en. *Nature* **430,** 329–332 (July 2004).

44. Dolde, F. *et al.* Sensing Electric Fields Using Single Diamond Spins. *Nature Physics* **7,** 459–463 (June 2011).

45. Kucsko, G. *et al.* Nanometer Scale Thermometry in a Living Cell. *Nature* **500,** 54–58 (Aug. 2013).

46. Toyli, D. M., de las Casas, C. F., Christle, D. J., Dobrovitski, V. V. & Awschalom, D. D. Fluorescence Thermometry Enhanced by the Quantum

Coherence of Single Spins in Diamond. en. *Proceedings of the National Academy of Sciences* **110,** 8417–8421 (May 2013).

47. Dolde, F. *et al.* High Fidelity Spin Entanglement Using Optimal Control. *Nature Communications* **5.** arXiv: `1309.4430` (Feb. 2014).

48. Togan, E. *et al.* Quantum Entanglement between an Optical Photon and a Solid-State Spin Qubit. en. *Nature* **466,** 730–734 (Aug. 2010).

49. Binnig, G., Quate, C. F. & Gerber, C. Atomic Force Microscope. *Physical Review Letters* **56,** 930–933 (Mar. 1986).

50. Chu, Y. *et al.* Coherent Optical Transitions in Implanted Nitrogen Vacancy Centers. *Nano Letters* **14,** 1982–1986 (Apr. 2014).

51. Yamamoto, T. *et al.* Extending Spin Coherence Times of Diamond Qubits by High-Temperature Annealing. *Physical Review B* **88,** 075206 (Aug. 2013).

52. Orwa, J. O. *et al.* Engineering of Nitrogen-Vacancy Color Centers in High Purity Diamond by Ion Implantation and Annealing. *Journal of Applied Physics* **109,** 083530 (Apr. 2011).

53. Naydenov, B. *et al.* Enhanced Generation of Single Optically Active Spins in Diamond by Ion Implantation. *Applied Physics Letters* **96,** 163108 (Apr. 2010).

54. Fu, K.-M. C., Santori, C., Barclay, P. E. & Beausoleil, R. G. Conversion of Neutral Nitrogen-Vacancy Centers to Negatively-Charged Nitrogen-Vacancy Centers through Selective Oxidation. *arXiv:1001.5449 [cond-mat].* arXiv: `1001.5449 [cond-mat]` (Jan. 2010).

55. Rabeau, J. R. *et al.* Implantation of Labelled Single Nitrogen Vacancy Centers in Diamond Using N15. *Applied Physics Letters* **88,** 023113 (Jan. 2006).

56. Meijer, J. *et al.* Generation of Single Color Centers by Focused Nitrogen Implantation. *Applied Physics Letters* **87,** 261909 (Dec. 2005).

57. Ohno, K. *et al.* Engineering Shallow Spins in Diamond with Nitrogen Delta-Doping. *Applied Physics Letters* **101,** 082413 (Aug. 2012).

58. Ziegler, J. F., Ziegler, M. D. & Biersack, J. P. SRIM – The Stopping and Range of Ions in Matter (2010). *Nuclear Instruments and Methods in Physics Research Section B: Beam Interactions with Materials and Atoms. 19th International Conference on Ion Beam Analysis* **268,** 1818–1823 (June 2010).

59. Gibbons, J. F. Ion Implantation in Semiconductors #8212;Part II: Damage Production and Annealing. *Proceedings of the IEEE* **60,** 1062–1096 (Sept. 1972).

60. Craighead, H. G. Nanoelectromechanical Systems. *Science* **290,** 1532–1536 (Nov. 1, 2000).

61. Ekinci, K. L. & Roukes, M. L. Nanoelectromechanical systems. *Review of Scientific Instruments* **76,** 061101 (6 May 26, 2005).

62. Anetsberger, G. *et al.* Near-field cavity optomechanics with nanomechanical oscillators. *Nature Physics* **5,** 909–914 (12 Oct. 11, 2009).

63. Park, Y.-S. Radiation pressure cooling of a silica optomechanical resonator (2009).

64. Chen, Y. Macroscopic Quantum Mechanics: Theory and Experimental Concepts of Optomechanics. *arXiv:1302.1924* [*gr-qc, physics:quant-ph*] (Feb. 7, 2013).

65. Wang, Y.-D. & Clerk, A. A. Using dark modes for high-fidelity optomechanical quantum state transfer. *New Journal of Physics* **14.** arXiv:1205.5284 [cond-mat, physics:quant-ph], 105010 (10 Oct. 10, 2012).

66. Dong, C., Fiore, V., Kuzyk, M. C. & Wang, H. Optomechanical Dark Mode. en. *Science* **338.** PMID: 23160956, 1609–1613 (6114 Dec. 21, 2012).

67. Krause, A. G., Winger, M., Blasius, T. D., Lin, Q. & Painter, O. A microchip optomechanical accelerometer. *arXiv:1203.5730 [physics]* (Mar. 26, 2012).

68. Dean, R. & Luque, A. Applications of Microelectromechanical Systems in Industrial Processes and Services. *IEEE Transactions on Industrial Electronics* **56,** 913–925 (4 Apr. 2009).

69. Stannigel, K., Rabl, P., Sørensen, A. S., Lukin, M. D. & Zoller, P. Optomechanical transducers for quantum information processing. *Physical Review A* **84.** arXiv:1106.5394 [quant-ph] (4 Oct. 2011).

70. Tao, Y., Boss, J. M., Moores, B. A. & Degen, C. L. Single-Crystal Diamond Nanomechanical Resonators with Quality Factors exceeding one Million. *arXiv:1212.1347 [cond-mat]* (Dec. 6, 2012).

71. Zwickl, B. M. *et al.* High quality mechanical and optical properties of commercial silicon nitride membranes. *Applied Physics Letters* **92,** 103125 (10 Mar. 14, 2008).

72. Coe, S. E. & Sussmann, R. S. Optical, thermal and mechanical properties of CVD diamond. *Diamond and Related Materials* **9,** 1726–1729 (9–10 Sept. 2000).

73. Jr, W. W., Timoshenko, S. P. & Young, D. H. *Vibration Problems in Engineering* en. 632 pp. (John Wiley & Sons, Feb. 14, 1990).

74. Babinec, T. M., Choy, J. T., Smith, K. J., Khan, M. & Loncar, M. Design and focused ion beam fabrication of single crystal diamond nanobeam cavities. *Journal of Vacuum Science & Technology B: Microelectronics and Nanometer Structures* **29,** 010601–010601 (1 2011).

75. Kouh, T., Karabacak, D., Kim, D. H. & Ekinci, K. L. Diffraction effects in optical interferometric displacement detection in nanoelectromechanical systems. *Applied Physics Letters* **86,** 013106 (1 Dec. 27, 2004).

76. Carr, D. W., Sekaric, L. & Craighead, H. G. Measurement of nanomechanical resonant structures in single-crystal silicon. *Journal of Vacuum Science & Technology B* **16,** 3821–3824 (6 Nov. 1, 1998).

77. Clerk, A. A., Devoret, M. H., Girvin, S. M., Marquardt, F. & Schoelkopf, R. J. Introduction to quantum noise, measurement, and amplification. *Reviews of Modern Physics* **82,** 1155–1208 (2 Apr. 15, 2010).

78. Golter, D. A., Oo, T., Amezcua, M., Stewart, K. A. & Wang, H. Optomechanical Quantum Control of a Nitrogen-Vacancy Center in Diamond. *Physical Review Letters* **116,** 143602 (Apr. 2016).

79. Bose, S. Quantum Communication through an Unmodulated Spin Chain. *Physical Review Letters* **91,** 207901 (Nov. 2003).

80. Duan, L.-M., Lukin, M. D., Cirac, J. I. & Zoller, P. Long-Distance Quantum Communication with Atomic Ensembles and Linear Optics. en. *Nature* **414,** 413–418 (Nov. 2001).

81. Briegel, H.-J., Dür, W., Cirac, J. I. & Zoller, P. Quantum Repeaters: The Role of Imperfect Local Operations in Quantum Communication. *Physical Review Letters* **81,** 5932–5935 (Dec. 1998).

82. Aspelmeyer, M., Kippenberg, T. J. & Marquardt, F. Cavity Optomechanics. *Reviews of Modern Physics* **86,** 1391–1452 (Dec. 2014).

83. Bochmann, J., Vainsencher, A., Awschalom, D. D. & Cleland, A. N. Nanomechanical Coupling between Microwave and Optical Photons. en. *Nature Physics* **9,** 712–716 (Nov. 2013).

84. Kippenberg, T. J. & Vahala, K. J. Cavity Optomechanics: Back-Action at the Mesoscale. en. *Science* **321,** 1172–1176 (Aug. 2008).

85. Wang, C. F. *et al.* Fabrication and Characterization of Two-Dimensional Photonic Crystal Microcavities in Nanocrystalline Diamond. *Applied Physics Letters* **91,** 201112 (Nov. 2007).

86. Ovartchaiyapong, P., Lee, K. W., Myers, B. A. & Jayich, A. C. B. Dynamic Strain-Mediated Coupling of a Single Diamond Spin to a Mechanical Resonator. en. *Nature Communications* **5,** 4429 (July 2014).

87. Ovartchaiyapong, P., Pascal, L. M. A., Myers, B. A., Lauria, P. & Bleszynski Jayich, A. C. High Quality Factor Single-Crystal Diamond Mechanical Resonators. *Applied Physics Letters* **101,** 163505 (Oct. 2012).

88. Manenti, R. *et al.* Surface Acoustic Wave Resonators in the Quantum Regime. *Physical Review B* **93.** arXiv: `1510.04965` (Jan. 2016).

89. Aref, T. *et al.* Quantum Acoustics with Surface Acoustic Waves. *arXiv:1506.01631 [cond-mat, physics:quant-ph].* arXiv: `1506.01631 [cond-mat, physics:quant-ph]` (June 2015).

90. Schütz, M. J. A. en. in *Quantum Dots for Quantum Information Processing: Controlling and Exploiting the Quantum Dot Environment* 143–196 (Springer International Publishing, 2017).

91. Magnusson, E. B. *et al.* Surface Acoustic Wave Devices on Bulk ZnO Crystals at Low Temperature. *Applied Physics Letters* **106,** 063509 (Feb. 2015).

92. Aref, T. *et al.* Quantum Acoustics with Surface Acoustic Waves. *arXiv:1506.01631 [cond-mat, physics:quant-ph].* arXiv: `1506.01631 [cond-mat, physics:quant-ph]` (June 2015).

93. Barnes, C. H. W., Shilton, J. M. & Robinson, A. M. Quantum Computation Using Electrons Trapped by Surface Acoustic Waves. *Physical Review B* **62,** 8410–8419 (Sept. 2000).

94. Barnes, C. H. W., Shilton, J. M. & Robinson, A. M. Quantum Computation Using Electrons Trapped by Surface Acoustic Waves. *Physical Review B* **62,** 8410–8419 (Sept. 2000).

95. Shilton, J. M. *et al.* High-Frequency Single-Electron Transport in a Quasi-One-Dimensional GaAs Channel Induced by Surface Acoustic Waves. en. *Journal of Physics: Condensed Matter* **8,** L531 (1996).

96. Manson, N. B., Harrison, J. P. & Sellars, M. J. Nitrogen-Vacancy Center in Diamond: Model of the Electronic Structure and Associated Dynamics. *Physical Review B* **74,** 104303 (Sept. 2006).

97. Tamarat, P. *et al.* Spin-Flip and Spin-Conserving Optical Transitions of the Nitrogen-Vacancy Centre in Diamond. en. *New Journal of Physics* **10,** 045004 (2008).

98. Falk, A. L. *et al.* Electrically and Mechanically Tunable Electron Spins in Silicon Carbide Color Centers. *Physical Review Letters* **112,** 187601 (May 2014).

99. Smith, W. R., Gerard, H. M., Collins, J. H., Reeder, T. M. & Shaw, H. J. Analysis of Interdigital Surface Wave Transducers by Use of an Equivalent Circuit Model. *IEEE Transactions on Microwave Theory and Techniques* **17,** 856–864 (Nov. 1969).

100. Golter, D. A., Oo, T., Amezcua, M., Stewart, K. A. & Wang, H. Optomechanical Quantum Control of a Nitrogen-Vacancy Center in Diamond. *Physical Review Letters* **116,** 143602 (Apr. 2016).

101. Teissier, J., Barfuss, A., Appel, P., Neu, E. & Maletinsky, P. Strain Coupling of a Nitrogen-Vacancy Center Spin to a Diamond Mechanical Oscillator. *Physical Review Letters* **113,** 020503 (July 2014).

102. Kepesidis, K. V., Bennett, S. D., Portolan, S., Lukin, M. D. & Rabl, P. Phonon Cooling and Lasing with Nitrogen-Vacancy Centers in Diamond. *Physical Review B* **88,** 064105 (Aug. 2013).

103. Doherty, M. W. *et al.* Theory of the Ground-State Spin of the NV- Center in Diamond. *Physical Review B* **85,** 205203 (May 2012).

104. Golter, D. A. *et al.* Coupling a Surface Acoustic Wave to an Electron Spin in Diamond via a Dark State. *Physical Review X* **6,** 041060 (Dec. 2016).

105. Golter, D. A., Oo, T., Amezcua, M., Stewart, K. A. & Wang, H. Optomechanical Quantum Control of a Nitrogen-Vacancy Center in Diamond. *Physical Review Letters* **116,** 143602 (Apr. 2016).

106. Lee, K. W. *et al.* Strain Coupling of a Mechanical Resonator to a Single Quantum Emitter in Diamond. *Physical Review Applied* **6,** 034005 (Sept. 2016).

107. Kepesidis, K. V., Bennett, S. D., Portolan, S., Lukin, M. D. & Rabl, P. Phonon Cooling and Lasing with Nitrogen-Vacancy Centers in Diamond. *Physical Review B* **88,** 064105 (Aug. 2013).

108. Vitanov, N. V., Halfmann, T., Shore, B. W. & Bergmann, K. Laser-Induced Population Transfer by Adiabatic Passage Techniques. *Annual Review of Physical Chemistry* **52,** 763–809 (2001).

109. Kurtsiefer, C., Mayer, S., Zarda, P. & Weinfurter, H. Stable Solid-State Source of Single Photons. *Physical Review Letters* **85,** 290–293 (July 2000).

110. Batalov, A. *et al.* Low Temperature Studies of the Excited-State Structure of Negatively Charged Nitrogen-Vacancy Color Centers in Diamond. *Physical Review Letters* **102,** 195506 (May 2009).

111. Maze, J. R. *et al.* Properties of Nitrogen-Vacancy Centers in Diamond: The Group Theoretic Approach. en. *New Journal of Physics* **13,** 025025 (2011).

112. Bergmann, K., Vitanov, N. V. & Shore, B. W. Perspective: Stimulated Raman Adiabatic Passage: The Status after 25 Years. *The Journal of Chemical Physics* **142,** 170901 (May 2015).

113. Tsaturyan, Y. *et al.* Demonstration of Suppressed Phonon Tunneling Losses in Phononic Bandgap Shielded Membrane Resonators for High-Q Optomechanics. EN. *Optics Express* **22,** 6810–6821 (Mar. 2014).

114. Cole, G. D., Wilson-Rae, I., Werbach, K., Vanner, M. R. & Aspelmeyer, M. Phonon-Tunnelling Dissipation in Mechanical Resonators. en. *Nature Communications* **2,** ncomms1212 (Mar. 2011).

115. Safavi-Naeini, A. H. *et al.* Two-Dimensional Phononic-Photonic Band Gap Optomechanical Crystal Cavity. *Physical Review Letters* **112,** 153603 (Apr. 2014).

116. Tsaturyan, Y., Barg, A., Polzik, E. S. & Schliesser, A. Ultracoherent Nanomechanical Resonators via Soft Clamping and Dissipation Dilution. en. *Nature Nanotechnology* **advance online publication** (June 2017).

117. Yu, P.-L. *et al.* A Phononic Bandgap Shield for High-Q Membrane Microresonators. *Applied Physics Letters* **104,** 023510 (Jan. 2014).

118. Narayanamurti, V., Störmer, H. L., Chin, M. A., Gossard, A. C. & Wiegmann, W. Selective Transmission of High-Frequency Phonons by a Superlattice: The "Dielectric" Phonon Filter. *Physical Review Letters* **43,** 2012–2016 (Dec. 1979).

119. Zhu, H. & Lee, J. E. .-.-Y. Design of Phononic Crystal Tethers for Frequency-Selective Quality Factor Enhancement in AlN Piezoelectric-on-Silicon Resonators. *Procedia Engineering. Eurosensors 2015* **120,** 516–519 (Jan. 2015).

120. Sigalas, M. M. & Economou, E. N. Elastic and Acoustic Wave Band Structure. *Journal of Sound and Vibration* **158,** 377–382 (Oct. 1992).

121. Kushwaha, M. S., Halevi, P., Dobrzynski, L. & Djafari-Rouhani, B. Acoustic Band Structure of Periodic Elastic Composites. *Physical Review Letters* **71,** 2022–2025 (Sept. 1993).

122. Maldovan, M. Sound and Heat Revolutions in Phononics. en. *Nature* **503,** 209–217 (Nov. 2013).

123. Nakahata, H. *et al.* Diamond-Based Surface Acoustic Wave Devices. en. *Semiconductor Science and Technology* **18,** S96 (2003).

124. Nakahata, H. *et al.* Theoretical Study on SAW Characteristics of Layered Structures Including a Diamond Layer. *IEEE Transactions on Ultrasonics, Ferroelectrics, and Frequency Control* **42,** 362–375 (May 1995).

125. Zhou, B. B. *et al.* Accelerated Quantum Control Using Superadiabatic Dynamics in a Solid-State Lambda System. *Nat Phys* **13,** 330–334 (Apr. 2017).

126. Yu, P. Y. & Cardona, M. Fundamentals of Semiconductors: Physics and Materials Properties (2010).